INVERSE DESIGN METHODS FOR COMPLIANT MECHANISMS

by

Alejandro Eduardo Albanesi

Dissertation submitted to the Postgraduate Department of the

FACULTAD DE INGENIERÍA Y CIENCIAS HÍDRICAS

of the

UNIVERSIDAD NACIONAL DEL LITORAL

in partial fulfillment of the requirements for the degree of

Doctor en Ingeniería - Mención Mecánica Computacional

2011

Contents

List of Figures

Abstract

The objective of this thesis is the study and development of inverse finite element methods (IFEM) for the design of compliant mechanisms. The problem consists in determining the initial shape of a mechanism such that it attains the desired design shape under the effect of service loads. This is formally known as an inverse design problem in the literature. Compliant mechanisms are a special class of mechanisms that gain some of its motion by elastic deformation in one or more members, rather than from rigid-body translations and/or rotations of classical rigid-body mechanisms. Mechanisms synthesis deals with the design of a suitable mechanism for a specified task or performance, and it begins with a prescribed task that must be achieved by using a yet unknown sized or shaped mechanism.

The first approach to determine the mechanism design for a given task was based on optimization methods. Structural optimization methods were tested in several applications. Optimization allows the user to create designs starting from scratch, in which a multitude of possible designs are obtained without the need of any initial commitment or proposal. This is perhaps the major advantage of this technique. However, the computational cost and the lack of physical insight to how and why the topology of a mechanism is created are still the main drawbacks.

It became evident that IFEM could make important contributions in the field of complaint mechanism design, in particular as a re-design tool, since IFEM solutions have shown better convergence than the direct methods from which they derive. It also avoids the trial and error approach used many times in the design process.

Early work focused in the development of a general 3D inverse FEM for

solids with large displacements in the elastic range, since a central aspect
when designing a body to have an imposed shape after severe deformation is
to compute its undeformed shape. However, the vast majority of flexible links
in compliant mechanisms are prismatic shaped and can be modeled as large-
deflection beam-type elements. Subsequently, it became evident that modeling
a beam using the 3D or plane stress inverse finite element method was con-
siderable waste of computational resources. This motivated the formulation of
an inverse finite element method for large-displacement beams in the elastic
range, as an extension of the previous work in inverse finite element methods.
It is specially suited for problems where an object has to be manipulated by
the mechanism with a prescribed contact force, allowing to maximize contact
points between the mechanism and the object geometry, and has a good com-
putational efficiency, requiring only a few iterations to converge to a feasible
solution. Several mechanisms were successfully tested and the results were
validated against the results of the literature.

This is novel methodology in the field of compliant mechanisms. There
is no background of inverse methods among the procedures used to design
compliant system since it departs from classical design methods used up-to-
date, being so far the only design method that does not rely on the use of
optimization techniques.

Resumen extendido

El objetivo de esta tesis es el estudio y desarrollo de métodos de elementos finitos inversos (IFEM) para el diseño de mecanismos flexibles. Se pretende determinar la forma inicial de un mecanismo tal que este adquiera la forma de diseño especificada cuando esta sujeto a las cargas de servicio. La denominación formal de estos problemas en la literatura es *problemas de diseño inverso*. Los mecanismos flexibles son una clase especial de mecanismos que adquieren parte de su movimiento por la deformación elástica de alguno de sus miembros, a diferencia de los mecanismos rígidos cuyos miembros no se deforman durante el movimiento (y cuyo movimiento viene dado por mera traslación y rotación de cuerpos rígidos). La síntesis de mecanismos consiste en diseñar un mecanismo adecuado para una tarea especificada por diseño, y comienza con un requerimiento que debe ser satisfecho mediante un mecanismo cuya forma y tamaño son incógnitas del problema.

En el análisis y diseño de mecanismos flexibles, la tarea de determinar la forma original que ha de tener un mecanismo se encaró en principio usando técnicas de optimización. Diversos ejemplos se llevaron a cabo, incluyendo optimización topológica, de tamaño y de forma de mecanismos. La solución obtenida a través de la optimización topológica es independiente de cualquier opción de diseño previo, y esto permite crear diseños desde cero, siendo ésta quizás la principal ventaja de esta técnica. Sin embargo, los algoritmos utilizados en la optimización de la topología asumen un comportamiento mecánico geométrico lineal, y es posible obtener soluciones inexactas al diseñar un mecanismo que estará sujeto a grandes deformaciones no lineales. El costo computacional sigue siendo la principal desventaja de este método.

Se hizo evidente entonces que IFEM podría aportar contribuciones impor-

tantes al diseño de mecanismos flexibles, en particular como herramienta de re-
diseño. Los modelos inversos siempre demostraron mejor convergencia que los
modelos directos de los cuales fueron derivados. Es además, una metodología
original y novedosa en la disciplina de los mecanismos flexibles ya que no hay
antecedentes en la bibliografía sobre el uso de IFEM para diseñarlos. Se aparta
de los métodos clásicos utilizados hasta la fecha, siendo además el único que
no depende de las técnicas de optimización estructural para obtener un diseño
final. Además, permite evitar el uso de la prueba y error empleado muchas
veces en todo proceso de diseño.

Las primeras aplicaciones de IFEM para el diseño de piezas sujetas a
grandes deformaciones elásticas aparecen hacia fines de 1990. Se trataba de
determinar la forma con que se debía fabricar una pieza (sólido bi- o tridimen-
sional, o axisimétrico) a fin de que adoptara la forma dictada por el diseñador
tras grandes deformaciones provocadas por solicitaciones conocidas (presión,
cambio de temperatura, fuerza centrífuga, etc.). Estos primeros trabajos se
concentraron en materiales hiperelásticos e isótropos.

Los trabajos iniciales desarrollados aquí se centraron en el desarrollo de
un método IFEM general para sólidos 3D sometidos a grandes deformaciones
en el rango elástico, donde la incognita en el diseño de una pieza sujeta a
grandes deformaciones es conocer su geometría no-deformada. Sin embargo,
los miembros que componen la gran mayoría de los mecanismos flexibles tienen
sección transversal prismática, y esto permite modelarlos como elementos de
viga de grandes deformaciones. Resultévidente entonces que modelar vigas con
un elemento finito 3D, o su particularización a tensión plana, era un desperdicio
de recursos computacionales. Esto motivó la formulación de un método de
elementos finitos inversos para vigas de grandes deformaciones en el rango
elástico, como una extensión del trabajo previo en elementos finitos inversos.

En vigas, a diferencia de sólidos como los que se estudiaron anteriormente,
no es posible definir con precisión los ejes principales Lagrangianos transver-
sales (que interesan como dato para la ley constitutiva) a la sección cuando
existe torsión. Dicho problema se resolvió planteando la ley constitutiva en
formulación Euleriana, dado que es justamente la configuración deformada la
que se supone conocida y en consecuencia se pueden definir ajustadamente los

ejes principales que el modelo requiere como dato. Así se logró resolver con gran precisión tanto problemas bi- como tridimensionales.

La formulación IFEM para vigas de grandes deformaciones en el rango elástico tiene buena eficiencia computacional, y requiere una pocas iteraciones para converger a una solución. Varios mecanismos flexibles 2D y 3D, en macro y micro escala, han sido analizados y validados con gran precisión. Podemos mencionar por ejemplo los mecanismos para transmisiones flexibles, (embragues y juntas), herramientas para cirugía no-invasiva (pinzas y micropinzas), y elementos pasivos para sistemas microfluídicos (microválvulas).

Las fallas detectadas en el método son la intersección y la interpenetración de elementos de viga, y la violación del espacio de diseño. En el primer caso, las intersecciones de elementos de viga da como resultado diseños no-viables, en el cual el diseño obtenido será incapaz de ejecutar el movimiento deseado. En cuanto a la violación del espacio de diseño, a medida que el cuerpo se deforma, algunos elementos pueden estar ubicadas fuera del dominio de diseño especificado.

Chapter 1

Introduction

A *mechanism* may be defined as a device formed by rigid or elastic elements joined together in order to allow the conversion and/or transmission of force, motion or energy. These elements are frequently referred to as *links* in the classical literature. Traditional *rigid-body* mechanisms consists of rigid links connected at movable joints, and their motion is composed of rigid-body translations and/or rotations. Presently, many mechanisms are designed to derive some mobility by elastic deformation in one or more links, so they gain at least some of their mobility from the deflection of flexible members rather than from movable joints only. This latter group is widely known as *compliant mechanisms*, and they rely on elastic strain in order to reach the desired degree of deformability. Every elastic structure is subjected to deformations under load and is therefore provided with some compliance; but only a special category of systems is designed to this purpose. Hence, a compliant mechanism can be defined as *a continuum made of elastic material which explicitly fulfills a deformability restriction* [WBWF07].

While not being properly a structure, a compliant system is neither a mechanisms buy something in between, or both at the same time, since it joins properties and challenges of both sorts of mechanical systems. However, each of them has its own nomenclature, principles, and definition of degrees of freedom, with the subsequent properties of the stiffness matrix. Another intrinsic characteristic frequently used in the literature to establish the difference be-

tween a compliant mechanism and a compliant structure is whether or not
the mechanical system performs its function transferring or transforming mo-
tion or energy: if it does, it's classified as a mechanism and if it doesn't, it's
classified as a structure [How01]. Many of the available analysis and design
methods apply to both structures and mechanisms, with diverging principles
and criteria. To avoid a common source of confusion, it is important to point
out that *stiffness and strength are not the same thing.* The former, as the
reciprocal of flexibility, defines how much a body deflects under a given load.
The latter defines the limit of deformation which the mechanical system un-
dergoes without being permanently damaged. The fact that deformabilty and
stiffness do not exclude each other plays an important role in the design of
compliant systems as it grants the construction of objects that are flexible and
strong at the same time [Ana94, KHLS99].

In the framework of the synthesis of compliant mechanisms and structures,
the mechanical design needs to fulfill [How01, KHLS99, WBWF07]:

- *deformability* requirements, specifying the geometric changes that the
  system under consideration must perform.

- *stiffness* requirements, which define the allowed deviations from the de-
  sired geometry under given loads.

- *strength* requirements, which specify the loads to be carried without dam-
  age.

- *activability* requirements, which state that the desired deformation is
  achieved by loading trough the actuator system.

- *a set of further* requirements related to the weight and energy consump-
  tion of the system.

In comparison with conventional rigid-body mechanisms, compliant mecha-
nisms are simpler and replace multiple rigid parts, pin joints and added springs.
In addition, they have several advantages over their rigid counterparts: there
is no wear, no backslash, less noise, they do not release particles, no lubrication

is required and are suited for monolithic manufacturing methods with no need for assembly. The benefits of the use of compliant systems can be summarized as follows [How01, KHLS99, WBWF07]:

- *assembly*: they are conceived to be monolithic and there is a reduced need for mechanism assembly. Some assembly may be needed, but the number of parts is far less in comparison to traditional rigid-body mechanisms.

- *no wear*: compliant mechanisms attain mobility trough deformation and therefore they experience no wear. As such, they do not release particles and there is no need for maintenance and lubrication.

- *no backslash*: due to the absence of discrete joints, compliant mechanisms do not suffer from backslash, stack up errors and clearances. As a result high precision may be obtained.

- *energy storage*: compliant mechanisms store energy as they deform. This energy may be used to assist in applications requiring a return stage. There is a reduced need for springs and possible actuation.

Most disadvantages of compliant systems are related to their fully coupled mechanical properties, in which load-carrying capabilities and deformability are shared by all degrees of freedom. While a typical rigid-body mechanism moves on a prescribed path independently of the acting forces, this does not hold for compliant mechanisms. Another disadvantage is the limited range of motion; an elastic element may be deformed up to a defined level, beyond which the allowable strain of the material is exceeded. Unlike movable joints used in rigid-body mechanisms, monolithic hinges can not be designed for an unlimited rotation angle due to the necessity of maintaining stress levels in all elements of the mechanism within the linear elastic regime [Lob03].

The deformation of a compliant system requires a definite amount of mechanical work, which is stored in the compliant component in the form of strain energy. This is generally seen as a disadvantage in the classical literature of rigid-body mechanisms, as the main purpose of a mechanism consists in converting motion and transferring force as efficiently as possible. However, this

can be seen from another perspective as an advantage since compliant mechanisms can be used to store and/or transform energy that can be released at a later time or in a different manner.

1.0.1   The basic nomenclature behind compliant mechanisms

In compliant systems, a distinction is usually made between systems with *concentrated compliance* (also called lumped compliance), consisting of stiff links and compliant pivots, and systems with *distributed compliance* in which only flexible segments are employed. Mixed and intermediate designs are also conceivable [WBWF07].

A *kinematic pair* is a mechanical constraint (joint) that prescribes the motion of two or more bodies, removing degrees of freedom. Kinematic pairs can be classified in two groups: *higher and lower pairs*. When two bodies have surface contact between them, they are joined by a lower pair (i.e. revolute joints, prismatic joints and planar joints, among others). A higher pair is formed when two bodies have line or point contact between them (e.g. cams and gears). A *link* is defined as the continuum connecting the mating surfaces of one or more kinematic pairs [Nor91, MNH94, How01]. Links connected together by joints constitute a *kinematic chain*. The chain is considered a *mechanism* if one of the links is fixed (usually connected to ground). The fixed link is in general taken as the *reference* link. A *kinematic inversion* is obtained when a different link is fixed.

If a mechanism has no joints, then it has zero links and it is called a *fully compliant mechanism*. Compliant mechanisms that contain one or more traditional kinematic pairs along with compliant members are called *partially compliant mechanisms*. Links are described by their *structural* and/or *functional* type, depending to whether the link is rigid or compliant. In rigid links the distance between joints is fixed and the shape of the link in unchanged regardless of the forces applied, so the structural type suffices to describe it. However, the motion of a compliant link depends on link geometry and location and magnitude of applied forces and therefore its description merely

based in its structural type turns out to be insufficient [How01]. The functional which considers the location and magnitude of applied loads and the number of *pseudo-joints*[1]is needed in conjunction with the structural type to fully describe a compliant link. Some authors characterize compliant links dividing them into *segments*, according to cross-sectional properties, material properties, and magnitude and placement of applied loads and displacements [Nor91]. A compliant segment may be further classified as *simple* (one that is initially straight and has constant material and cross-sectional properties) or *compound* (all other segments that are not simple).

The DOF of the system and Grueber's equation

Traditional mechanism analysis assumes that the deflection of its parts is negligible compared to the overall motion, which means that motion is not a function of the shape of the links or the loads applied. This grants the kinematic analysis to be performed independently from kinetic analysis, thus simplifying the design task.

The degrees of freedom (DOF) of a rigid body are defined as the number of independent movements it has. In a two dimensional plane (a planar unconstrained rigid link) there are three DOF. The link has traslation in the x and y axis, and rotated about its centroid. If a kinematic chain is made up of n links, then the total DOF is $3n$ [RR01]. A kinematic chain is considered a mechanism if one of the links is fixed, reducing the total DOF to $3(n-1)$. Kinematic constraints such as lower or higher pairs result in the decrease of the degrees of freedom. A lower kinematic pair in planar mechanisms (such as a revolute or prismatic pair) removes two degrees of freedom from the system. Lower pairs in spatial mechanisms (i.e spherical, plane, cylindrical, revolute, prismatic, and screw pairs) remove anywhere from one to three degrees of freedom, and higher pairs remove only one degree of freedom [Nor91, How01]. *Grueber's* equation is an analytical expression to compute the degrees of freedom in a planar mechanism

---

[1]Pseudo-joints are present when a load is applied to a compliant link other than at the joints, inducing a significant change in its behavior.

$$DOF = 3(n-1) - 2K_l - K_h \tag{1.1}$$

in which n is the total number of linkages, K_l is the total number of low kinematic pairs, and K_h is the total number of high kinematic pairs. When $DOF = 1$ the linkage is called a mechanism, where any of the movable links can be driven by an external force. The remaining movable links will then have constrained motion. When $DOF = 0$ the linkage forms a structure, in which case external forces do not produce relative motion between links. If $DOF > 1$ the linkage will require more than one driving external force to obtain the constrained motion. In case $DOF < 1$, there is a redundant member and the chain is a statically undetermined structure.

Grashof's criterion and the mobility of the system

The mobility problem has been of interest for a long time in the area of mechanism design. A mechanism may encounter a singular configuration under certain geometric conditions, at which the instantaneous degree of freedom (the transitory mobility of the mechanism) will be different from the result derived by the Grubler's equation. When a singular configuration occurs during the motion, the relative motion between links is in a critical state and the mobility of some link (s) will become zero. Therefore, the study of the geometric relations for linkages under singular conditions may help in understanding the mobility of the linkages. Rigid four-bar mechanisms are the simplest movable linkage, and consists in links attached to two others by single joint or pivot, conforming a close-loop kinematic chain. If s the length of the shortest link, l the length of the longest link, and p and q the length of the remaining links, *Grashof's* law states that for at least one of the four links to have full rotation, the following inequality must hold:

$$s + l \leq p + q \tag{1.2}$$

and that none of the four links can make a full revolution if

$$s + l > p + q \tag{1.3}$$

Inequality 2.11 is called the Grashof's criterion or Grashof's inequality. It is both necessary and sufficient for the existence of at least one fully-rotatable link in a four-bar linkage. Extension of Grashof's criteria to five-bar mechanisms was first investigated by Ting [15], and extended to N-bar kinematic chains later by Ting [16] and Ting and Liu [17]. In the derivations of rotation laws for N-bar linkages, Grashof's theorem becomes a particular case.

Mechanical Advantage: Amplification/Deamplification of Motion/Force

A compliant mechanism needs to provide a specified output displacement or specified output force, according to its main functional objective. Either task has to be solved in terms of an output performance criterion (a prescribed displacement, force, path or load history). In general and under work conservation principles, a mechanism that amplifies the output displacement will necessarily reduce the force that can be delivered at its output port. Conversely, a mechanisms that is designed to amplify the output force will produce less output displacement. The *mechanical advantage* (MA) of the mechanism is defined as a ratio of the force/torque between the output and the input [How01]:

$$MA = \frac{\|\boldsymbol{F}_{out}\|}{\|\boldsymbol{F}_{in}\|} \tag{1.4}$$

Another definition is the ratio between the output and input displacements [Lob03], also known as the *geometric advantage*:

$$GA = \frac{\|\boldsymbol{u}_{out}\|}{\|\boldsymbol{u}_{in}\|} \tag{1.5}$$

It's important to remark that the computation of MA or GA assumes that power is conserved between the input and the output, and that the system is in static equilibrium.

1.0.2   Design of mechanisms: analysis and synthesis

Traditionally, the design of mechanisms was an art, based primarily on the experience of the designer. Even today, despite scientific and technological

advances, the task of conceptualizing these devices is still a mixture of art and science. In this process, *kinematic analysis* is used to determine the characteristic motion of a mechanism. Nevertheless, an initial seed mechanism is required to perform this task and therefore its use does not grant the design of a mechanism from *scratch*, since the experience and insight of a designer is required to create the seed mechanism.

Kinematics synthesis deals with the systematic design of mechanisms for a specified task or performance [ES97, How01]. It begins with a prescribed task that must be achieved by using a yet unknown sized or shaped mechanism (it attempts to design a new device matched to a user-specified task). In general, design problems have many different solutions, and therefore they involve the iteration between synthesis and analysis. Kinematic synthesis is performed to determine the dimensions of the mechanism and possesses three customary tasks: *path generation*, *motion generation* and *function generation* [ES97]. In path generation, a point of the mechanism is required to travel along a specified path or preset points. Motion generation is restricted to a finite number of positions at which the designer desires to control the orientation of output members. Function generation is the correlation of the input and output links of the mechanism, and involves satisfying the input-output relationships. The major categories of synthesis include *type*, *number* and *dimensional* synthesis [How01]. In type synthesis, the selection of the mechanism best suited to solve the problem is addressed (e.g. linkages, gears, cams, etc). Number synthesis, which may be considered a subset of the latter, involves the determination of the number of links and degrees of freedom the mechanisms should have to perform the task. At last, dimensional synthesis involves the determination of the mechanism significant geometry to accomplish the specified task and performance (e.g. link length, area, angles, ratios, etc), but it assumes the existence of a presupposed mechanism topology.

As a final remark, mechanism synthesis should preferably be carried out within the framework of large displacement, non-linear analysis. Designs obtained using linear analysis typically behave differently when modeled using large displacement analysis. In the best of situations one merely has inaccurate results but in the worst cases the results become useless for large displacement

behavior [BS04]. Bruns and Tortorelli [BT01] compared the deformed shape of an optimal cantilever beam (loaded by at the tip) computed by linear analysis, with the shape computed by non-linear analysis. The comparison is depicted in Figure 1.1, from where it can be seen that at low load levels the optimal shape computed by linear analysis is similar to the shape computed by non-linear analysis. However, as the load level increases, the linear assumption becomes invalid and the resulting computed shape is dramatically altered. Therefore, the use of geometric non-linear finite element modeling is absolutely essential for mechanism synthesis.
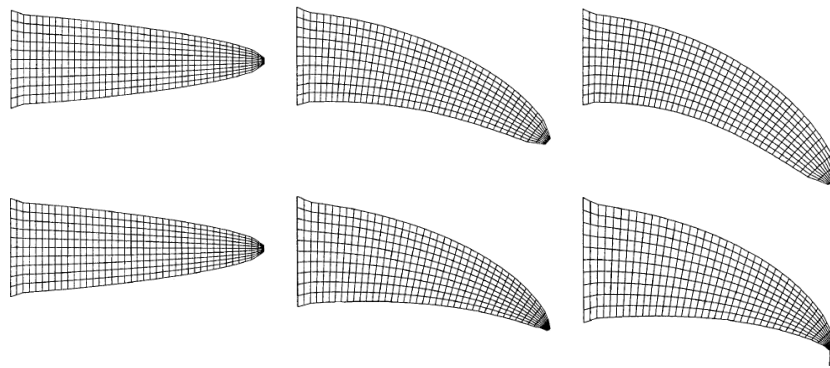
Figure 1.1: Deformed configurations the optimal boundary shape of a cantilever beam based on linear elastic analysis (top), and on non-linear elastic analysis (bottom). Tip loads are: 10 N (left), 1000 N (middle) and 1500 N (right), Bruns and Tortorelli [BT01].

1.1   A brief historical background on classic design methods

Up to the 1950s, the field of kinematics was limited to the study of rigid-body motion as this assumption greatly simplified the analysis of kinematics, which was captured using only the geometry of the mechanism. The benefits of compliant mechanisms, however, motivated the research of motion transmission by means of material deformation. Typically, there are two approaches known in the classic literature for the synthesis of compliant mechanisms, the *kinematic-*

based approach and the *structural optimization* approach, in accordance with flexibility distribution in the system.

Systems with concentrated compliance

In systems with *concentrated compliance* kinematic joints are replaced with flexible hinges, and therefore they behave like classic *rigid mechanisms* (Figure 1.2). Existing methods conceived to design rigid-body mechanisms can be modified and successfully applied in this kinematics-based approach.
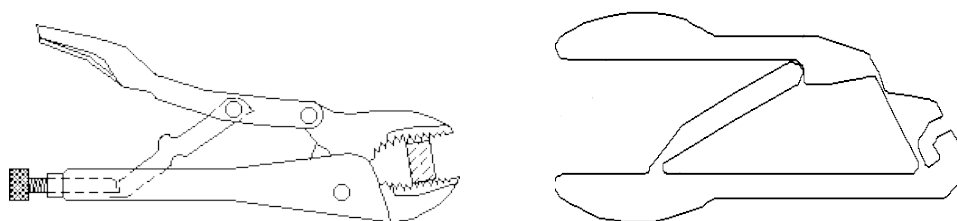
Figure 1.2: Mechanisms with concentrated compliance: a rigid crimping mechanism (left) and its compliant counterpart (right) [How01]. Areas with lower stiffness (i.e. smaller cross-section) are clearly visible in the compliant model (right) and serve as compliant hinges that allow the motion of the mechanism.

Synthesis methods for mechanisms with concentrated compliance had its genesis in the works of Ashok Midha in the middle 1980s. Her and Midha [HM87] introduced the *link compliance content* (*lc*) in order to define the *degree of compliance* of the mechanism as the summation of the degrees of freedom attributed to the rigid-body degrees of freedom and the elastic degrees of freedom. This provided the foundation to develop a systematic but also straightforward and intuition-based tool to classify and design mechanisms with concentrated compliance [MNH94]. Howell [How93] formulated the loop closure equations for compliant mechanisms with flexural pivots, in which compliant links are modeled as cantilever beams with a small-length flexural pivot located at the fixation to grant the rotation of the beam (the beam rotates about a fixed point called characteristic pivot). Elliptic integrals were used to compute the deflection of the mechanism. This approximation was the foundation for one of the most popular techniques to analize the de-

flection of mechanisms with concentrated compliance: the *pseudo-rigid-body model* (PRBM) [HM94, HM96].
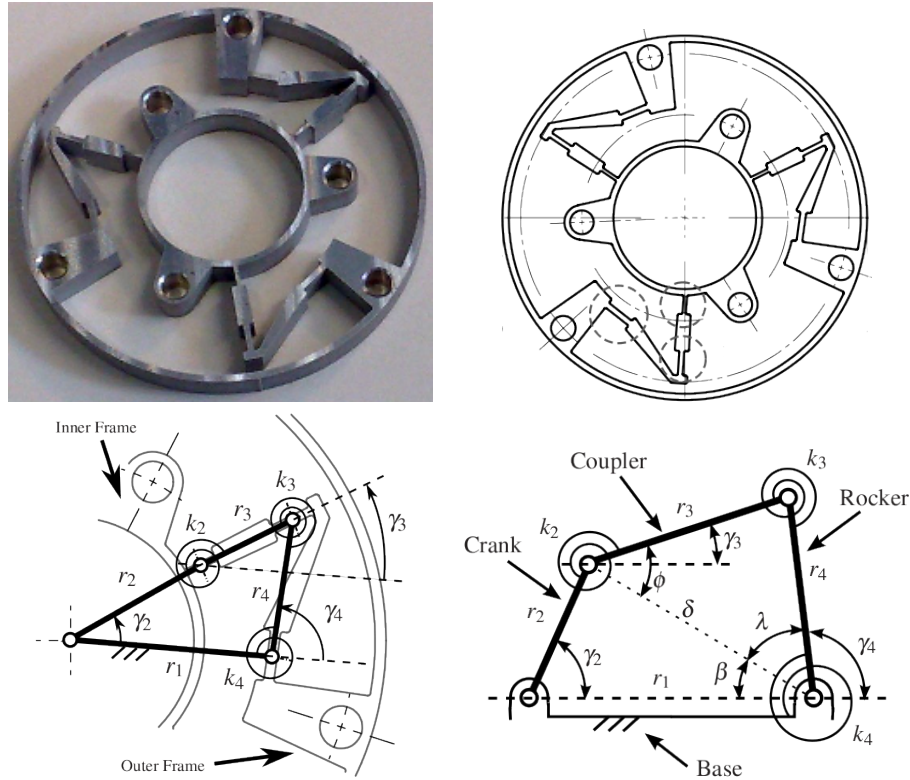
Figure 1.3: Design of a compliant transmission: the inner circle of the joint is fixed to the ground and torque is applied to the outer circle to allow its motion (top left) and a detail view of the multiple cross-sections that form the joint (top right). An schematic view of the four bar mechanism used to model the joint (bottom left) and its pseudo-rigid body model (bottom right) [PMBV10].

In PRBM, flexible links are modeled as rigid links connected by kinematic joints and torsional springs as a substitute for the bending stiffness of the solid hinge. This permitted to use all the information available for the synthesis of rigid-body mechanisms in compliant mechanisms design. Figure 1.3 depicts the pseudo-rigid body model of a compliant joint proposed by Palli *et al.* [PMBV10]. Different types of compliant segments require different pseudo-rigid models that predict its deflection path and force-deflection relationship. It may be used to design mechanisms to perform the traditional tasks of kinematic synthesis (path, motion or function generation) without concern for the

energy storage in flexible members. In early design stages it may serve as a fast and efficient method to evaluate different trial designs to meet the specified design objectives. Nevertheless, PRBM serves for analysis only (an initial mechanism configuration is needed), and it should be combined with another method if the creation of mechanisms from scratch is pursued.

Murphy [MMH96] developed a synthesis method based in graph theory to design compliant mechanisms. Graph theory has been used from the 1960s for the abstract representation of kinematic structures in the aim to develop a systematic and automated method to design rigid-body mechanisms. Freudenstein and Dobrjanskyj [FD65] developed a mathematical representation of basic rigid-kinematic chains, in which links are represented by vertices and joints are represented by edges. This procedure is based on the separation of the mechanism structure from its function, since all kinematic chains enumerated using graph theory result on purely topological considerations. An advantage of graph representation is that kinematic chains can be represented in matrix form, but perhaps the mayor advantage is that most steps needed to synthesize a mechanism can be automated, and this led to the creation of the firsts truly systematic approach for mechanisms synthesis.

With the purpose to extend this methodology for compliant mechanisms, Murphy added information concerning the nature of link deformation to the traditional data of link connectivity. Possible deformation in a compliant link can be specified by determining the link compliance content (lc) of Her and Midha mentioned above. The combination of the link compliance content concept with the matrix representation of link connectivity resulted in the creation of a new method to represent the structure of compliant mechanisms, where several different topologies can be generated starting from an initial seed mechanism, using systematic enumeration and atlases of mechanisms[2]. In his PhD thesis, Pucheta [Puc08] combined graph theory and the pseudo-rigid-body model to develop a synthesis tool to conceive planar rigid and/or partially compliant mechanisms, in which graph theory is used to generate different topologies and the pseudo-rigid-body to analyze each one of them. Figure 1.4 depicts the design of a bistable actuator for a landing gear mechanism carried out by Pucheta and Cardona [PC10], using graph theory and the pseudo-rigid-
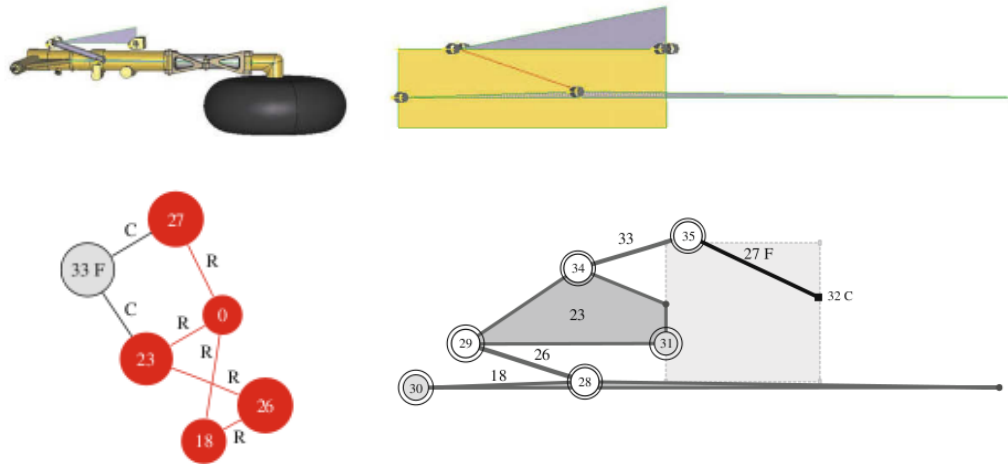
Figure 1.4: Design of a bistable actuator for a landing gear mechanism: the landing gear (top left) and its kinematic chain (top right), the graph representation of the proposed solution (bottom left) and the kinematic chain of this solution (bottom right). References for joint types in graphs are: R = revolute, C = clamped. In sketches, flexible links have a letter F, other links are assumed to be rigid. Pucheta and Cardona [PC10].

body model.

Systems with distributed compliance

Methodologies to design mechanisms with *distributed compliance* (Figure 1.5) appeared in the middle of the 1990s, departing from the work done in the kinematic-based approach. In this case strains are evenly distributed so as to reduce stress concentrations, and the mechanism is treated as a continuum flexible structure. Therefore, Continuum Mechanics design methods are used instead of rigid-body kinematics. By leaving material distribution virtually free, topology optimization techniques posses the ability of being independent of prior design choices. Nevertheless, results obtained through optimization often need further interpretation and modification involving the designer's judgement, so they are still far from being fully systematic.

The typical problem of structural optimization is to find the "best" struc-

---

[2]An atlas is a topological design space constituted only by connected topologies in non-isomorphic ways [PC07, PC10].

ture which is, at the same time, of minimal weight and of maximum strength.
The definition of "best" depends on many considerations: the mechanical
model used (linear, non-linear, plasticity, etc), the constraints on the admissi-
ble shapes and the stiffness criterion, among others [ABFJ97]. Most of classical
optimization algorithms solve the same mathematical problem: minimize an
objective function $f(x)$ (if minimizing $f(x)$ improves the design), under a set
of restrictions $c(x)$, by varying the value of one or more design variables x_j
between specified bounds [Van84].
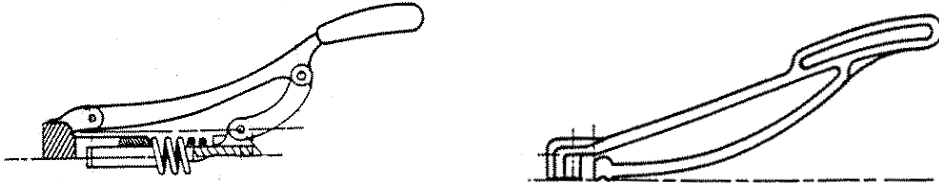
Figure 1.5: Mechanisms with distributed compliance: a rigid crimping mech-
anism (left) and its compliant counterpart (right) [How01].

Structural optimization in mechanism design is utilized in three main lev-
els: *topology*, *shape* and *size* optimization. In topology optimization, design
variables describe the connection among various portions of the mechanisms
(input and output ports, fixed region, holes). Shape optimization deals with
the shape that individual segments of the mechanisms must acquire, once a
topology has been established [HM03, All02]. At the lowest level, once the
topology and shape of the mechanism are defined, the last step is size opti-
mization where the design variables are the cross-section dimensions, length of
of beams or truss-like segments, thickness of shells and so on.

In classic topology optimization material is iteratively removed[3]reducing
the density of an element or by eliminating the element completely. The work
of Kikuchi and Bendsøe [KBe88] pioneered the generation of optimal mecha-
nisms topologies by means of the *homogenization method*[4], treating the design
domain as if it was made of composite material consisting of a solid and void
periodic microstructure. Bendsøe [Be89] and Rozvany *et al.* [RZS94], [Roz97]
were the first to apply a penalized variable density approach to approximate
the material-void problem, where a density variable is associated with each

finite element. Further development of material-void problem led to the creation of the *continuous material density parametrization* method, in which an artificial *material density* function limited by two bounds is defined and the algorithm varies the material density at each point of the domain. When this function reaches the lower bound it implies that the element is made of very soft material, and its eliminated from the structure. If the function reaches the upper bound then the element becomes the solid portion of the optimal mechanism. The main inconvenient of this method arises when the optimum value of the density function is between the bounds. This is an undesirable feature, not only because the manufacturing process involving variable density materials is expensive, but also because the mechanism presents *natural hinges* by the use of soft and stiff materials, which are a source of numerical instability. To overcome this inconvenient, algorithms have been developed to push the design variables to either one of the limits.

Alternative approaches in structural optimization departed from the use of the homogenization method. Frecker *et al.* [FAN+97] developed a method that transformed rigid-link mechanism topologies in equivalent compliant mechanisms using data derived from kinematic synthesis to guide the homogenization method and an initial domain of truss elements. The initial topology consists in a network of *truss elements* (called *ground structure*), which is reduced to the final topology through the minimization of the mutual strain energy. Hetrick [HV99] developed a unified energy formulation using a network of *frame elements*, in which topology and dimensional synthesis is performed through the optimization of energy efficiency. The use of frame elements does not differ much from the use of truss elements since axial stiffness dominates all other available modes of deformation in both types of elements. Ground structure parametrization is a discrete synthesis approach in which the topological synthesis is first solved using discrete algorithms. Some elements are removed for

---

[4]There are alternative methods in which the design domain is empty at the beginning of optimization and material is added until a constraint is fulfilled ([AVMC10]). These will be described later.

[4]The homogenization method was originally developed by Bendsoe [KBe88, Be95, BS04] to design optimal structures with maximum stiffness. Ananthasuresh [Ana94] also worked in the generation of mechanism topology by means of structural optimization using the homogenization method.
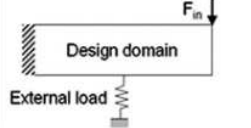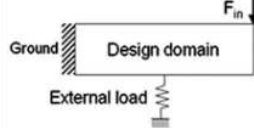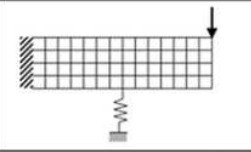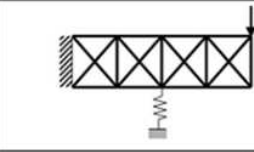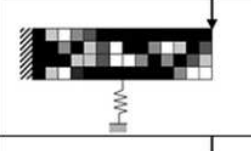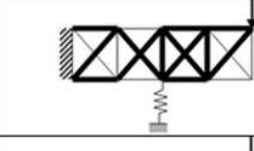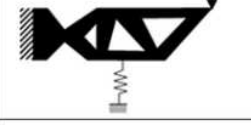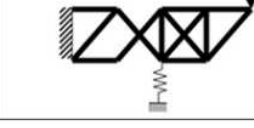
Typical Synthesis Procedure	(a) Homogenization	(b) Ground Structure
Step 1: Problem Specification - Define design domain - Apply boundary conditions		
Step 2: Design Domain Parameterization - Discretize design domain - Define design variables		
Step 3: Topology Optimization - Define objective function - Choose and implement optimization method		
Step 4: Final Design Interpretation - Filter out elements with values under certain threshold - Interpret final topology		

Figure 1.6: Comparison between continuous material density parametrization and ground structure parametrization [LK06].

the ground structure, and the remaining elements will define the topology and shape of the mechanism. Figure 1.6 depicts a comparison between continuous material density parametrization and ground structure parametrization made by Lu and Kota [LK06].

Wang *et al.* [WCWM05, WW06, WL07] introduces a level set (LSM) based methodology to compute the topology of multi-material compliant mechanisms. Following the classic level-set definition, where a closed curve is represented by an auxiliary function that takes positive values inside the curve, negative values if its outside the curve, and a null value at the boundary, Wang's method extends the level set definition to the design of monolithic compliant mechanisms made of multiple materials, as a topology optimization process capable of performing changes of the geometry by merging or splitting parts. The objective function of the optimization scheme is the mechanical advantage (the ratio of forces) or the geometric advantage (the ratio of displacements) of the mechanism [Wan09]. Figure 1.7 depicts some iterations of the topology optimization of a bi-material pull-clamp (represented in the

figure in different colors), computed through LSM.
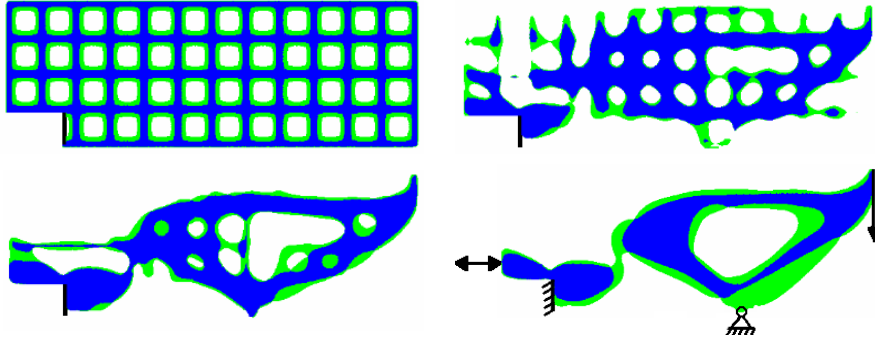
Figure 1.7: Design of a compliant pull-clamp using LSM (taking advantage of symmetry): the initial design domain (top left), intermediate iterations (top right) and (bottom left), and the optimal final design (bottom right) [WCWM05].

Ansola *et al.* [AVMC10] proposes an *element addition method* to synthesize 3D compliant mechanisms, based in bidirectional evolutionary structural optimization (BEVO) which allows for efficient material to be added to the structure at the same time as the inefficient one is removed. At the beginning of the optimization the design domain is empty, and material will be added gradually until the volume amount constraint is fulfilled. The objective function (to be maximized) is the mechanical advantage, and elements of large sensibility number will be added to the finite element model since those elements will introduce the largest increase of the objective function. This method also eliminates the natural hinges that appear by the use of soft and stiff materials. The optimized topology of a 3D inverting mechanisms computed with BEVO (taking advantage of the symmetry of the model) and the resulting complete model built upon the results of the finite element analysis are depicted in Figure 1.8, [AVMC10].

Other optimization techniques were introduced by Lu and Kota [LK03, LK05], in which a load-path formulation and genetic algorithms are used to design compliant mechanisms with shape morphing characteristics. Although structural optimization offers a method to obtain an initial design from problem specifications (there is no need of initial seed mechanisms), its success
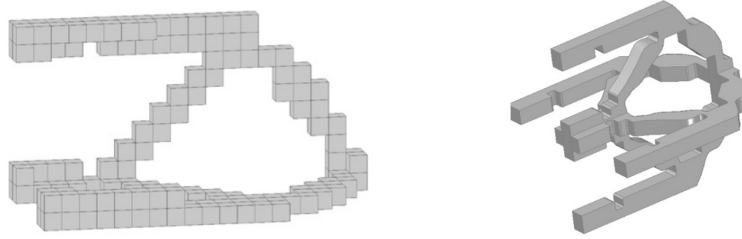
Figure 1.8: The optimized topology of a 3D inverting mechanisms computed with BEVO (left), and the resulting complete model (right), [AVMC10].

depends on the proper objective formulations and optimization algorithms, and most importantly it does not involve any physical insight to how and why elements of a mechanism combine.

1.2   A novel synthesis method with inverse models

The application of inverse methods to solve theoretical problems in mathematics and physics can be traced back to several decades, in particular in applications such as dispersion problems (inverse scattering), spectral problems in differential equations (inverse spectra), quantum mechanics, acoustics, geophysics, seismology and astronomy to name a few [Tar05]. Perhaps the most widespread inverse problems are inverse measurement problems, where the goal is to compute material parameters (e.g. elastic properties, electrical and thermal conductivity, dielectric constant, etc). However, the application of inverse methods in problems of solids under large deformations is relatively recent. When designing structural elements subject to large deformations, it is useful to know its initial non-deformed configuration. Such method grants the computation of the initial (unloaded) shape of a body such that it attains the given design shape when subjected to service loads once the steady state has been attained, neglecting any transient effect. This type of problems are defined as *inverse design problems* [BW98], in contrast to classical *inverse measurement problems*.

Previous numerical models for the inverse design analysis of hyperelastic bodies subjected to large deformations have been proposed by Govindjee and Mihalic [GM96, GM98] and Yamada [Yam97]. Govindjee and Mihalic [GM96] presented an inverse finite element formulation for 2D elastostatic problems, and determined the *manufacturing geometry* of a material grid, such that once the grid is extracted from molding matrices, remaining internal stresses force the grid to attain a perfectly rectangular shape. Subsequently, Govindjee and Mihalic [GM98] incorporated quasi-incompressibility to the former model, and solved the problem of a rubber punch for stamping applications, such that when the punch is under service loads, its shape exactly fits the mold shape (Figure 1.9).
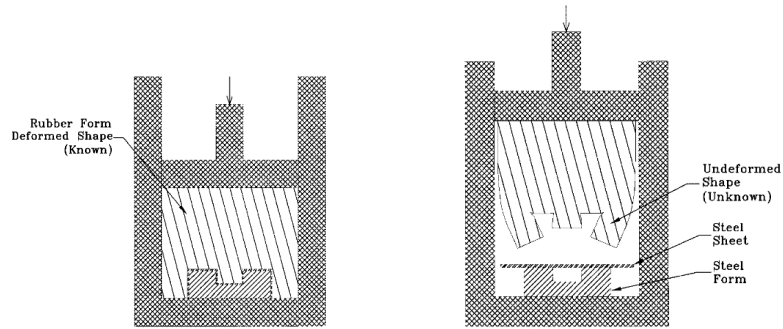
Figure 1.9: Determination of the manufacturing shape of a rubber punch for stamping applications: initial deformed configuration (left), and the manufacturing shape computed through inverse analysis (right) [GM98].

Troxler [Tro02] presents a 2D inverse method coupled to a re-meshing procedure for designing nozzles and diffusers in gas turbines, provided they meet certain distribution of static pressure. More recently, Lu *et al.* [LZR07a] and Fachinotti *et al.* [FCJ08] developed three-dimensional models for the inverse design of anisotropic hyperelastic solids. This work adresses the computation of the unloaded shape of the compressor blade of an aircraft engine, such that it attains the optimal geometry determined by fluid mechanics calculations under the effects of centrifugal loads (Figure 1.10).

The formulation of inverse finite elements models for other structural members is an area of prominent development. Recently, an inverse finite element model of shells was presented by Zhou *et al.* [ZL08], and for large deflection

beams by Albanesi *et al.* [AFC10]. This latter work was the keystone to develop a new design method for compliant mechanisms based in inverse analysis. Since most flexible links in compliant mechanisms are prismatic shaped (where one of its dimensions, the length, is predominant over the other two) they can be modeled as large-deflection beam-type elements. This grants the use of the inverse finite element of large displacement beams as a design tool, starting from the mechanism task (*deformed configuration*) and addressing the computation of the free unloaded configuration (*manufacturing shape*) of the mechanism. Several design problems taken from the literature demonstrate the accuracy of results obtained with this inverse model, and in general a lower computational cost compared to classical design methods. All kind of bar-mechanism (including flexural hinges), with concentrated and distributed compliance, can be modeled with this inverse beam element. Alternative types of inverse finite elements can be used in addition to the inverse beam element when the geometry of the body under analysis departs from the extents of a beam model. The three-dimensional model formulated by Fachinotti [FCJ08] is for bodies in which the length is of the same order than the height and width).
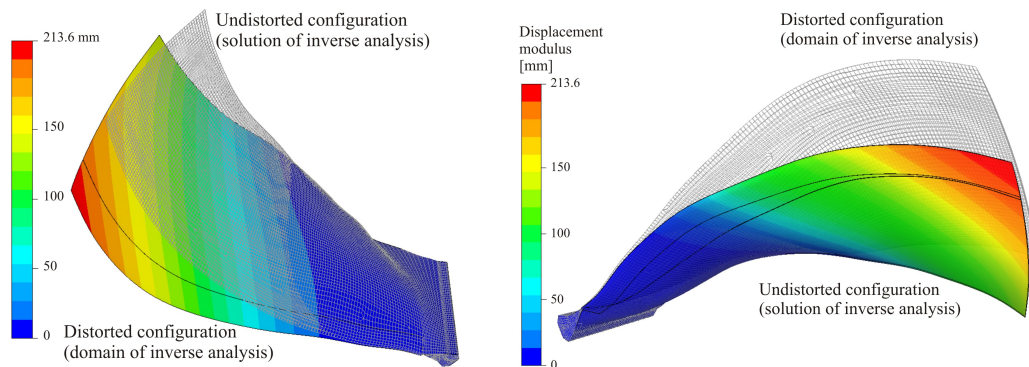
Figure 1.10: Computation of the unloaded shape of a turbine compressor blade: deformed configuration represented as a mesh surface, and manufacturing shape computed through inverse analysis with hyperelasticity represented as a solid surface [FCJ08].

Future work will consists in the development of an inverse shell element, in order to extend the inverse tool to the design of shell and membrane type

of bodies. Problems of sheet metal stamping and inflatable structures can be addressed with this element, along with simulation of veins and arteries in biomedical problems.

1.3 Content of this thesis

This thesis pursues the development of inverse finite element methods to design compliant mechanisms. In this chapter, the historical background of compliant mechanisms was revised. The standard nomenclature was introduced, and design methods were briefly discussed.

In Chapter 2, the design of mechanisms by optimization is presented. Structural optimization methods (e.g. topology, size and shape) are described and tested in the context of mechanisms design and synthesis. Several applications were carried out, including topology and size optimization of compliant mechanisms. Afterward, the synthesis of a four-bar compliant mechanisms for compliant-segment motion generation tasks solved by structural optimization is presented. Links were modeled with non-linear, small and large-displacement FEM elements.

In Chapter 3, a finite element model for the inverse design of solids with large displacements in the elastic range is presented. It consists in determining the initial shape of a body, such that it attains the designed shape under the effect of service loads. Compliant mechanisms and flexible structures of any shape can be modeled with this element. the treatment of body forces is discussed, along with the particularization to plane-stress and plane-strain applications.

In Chapter 4, an inverse finite element model for large-displacement beams in the elastic range is introduced, as an extension of the previous work in inverse finite element methods presented in Chapter 3. Flexible links in compliant mechanisms can be modeled with this element, which consists in the determination of the initial shape of a beam such that it attains a specified design shape under the effect of service loads.

In Chapter 5, several applications of the inverse FEM for large-displacement beams are presented. The design of macro and microscale mechanisms with

concentrated and distributed compliance is studied, in particular in compliant mechanisms that exactly fulfill a desired shape. The computational cost and stability of the solution is discussed, along with the advantages and disadvantages of inverse FEM as a design tool for compliant mechanism.

Chapter 2

Design of compliant mechanisms by optimization

Structural optimization is a frequently used method to design compliant mechanisms, in particular when a large portion of the mechanism deforms when its loaded. The work in this chapter addresses the design of fully compliant mechanisms trough size and shape optimization. The complete design of a compliant four-bar mechanism for motion generation tasks will latter be addressed by optimization. In traditional rigid-body mechanisms, motion-generation tasks require a rigid-body to move through a specified number of position points. However, when the body to be guided is flexible and has an initial smooth shape, the task of moving it from its initial configuration to a final (specified) configuration is referred to as segment-motion generation, as the flexible body is moved through a sequence of prescribed shapes in addition to the prescribed points of rigid-body motion.

2.1   Structural optimization

Shape optimization deals with the shape of the individual segments of a mechanism, when topology remains unchanged [All02, HM03]. The general optimization problem in structural design can be formulated as to minimize an objective function, usually subjected to nonlinear equality and inequality con-

straints:

$$
\begin{aligned}
\min\ & f\left(\boldsymbol{x}\right) \\
& g_j\left(\boldsymbol{x}\right) \leq 0 \quad j = 1, 2, ..., m \\
& h_k\left(\boldsymbol{x}\right) = 0 \quad k = 1, 2, ..., m \\
& \underline{c_l}\ \leq\ c_l \leq \overline{c_l} \quad l = 1, 2, ..., m \\
& \underline{x_i} \leq x_i \leq \overline{x_i} \quad i = 1, 2, ..., n
\end{aligned}
\tag{2.1}
$$

where $\boldsymbol{x} \in \mathbf{R}^n$ is the vector of design variables, $\underline{x_i}$ and $\overline{x_i}$ are given real numbers that represent the bounds of the variables, and f, the objective function, is a differentiable, real-valued function [Van84, Kir93]. Equation 2.1 corresponds to classical structural optimization problems of major interest, termed *min-max* problems. Typical objective in structural optimization are

- maximization of stiffness.

- minimization of weight.

- minimization of volume.

- etc

Typical constraints are stresses, buckling loads, natural frequency and normal modes, suitable flexibility, etc. These constraints relate through laws of structural mechanics to the design variables of the problem. Algorithms to search the optimum design can be classified into simultaneous and sequential. In simultaneous algorithms, trial designs are selected before analysis is started. Designs computed by sequential search algorithms are generated using results from previous iterations.

In optimization, the *design space* is the geometrical space where all feasible and unfeasible designs lay. Feasible designs are those that do not violate the imposed constraints [Van84, Kir93, RR05].

The representation of the design space is depicted in Figure 2.1, where $x_i\ \ i = 1, 2, ..,$ are design variables and every point in the figure represent a
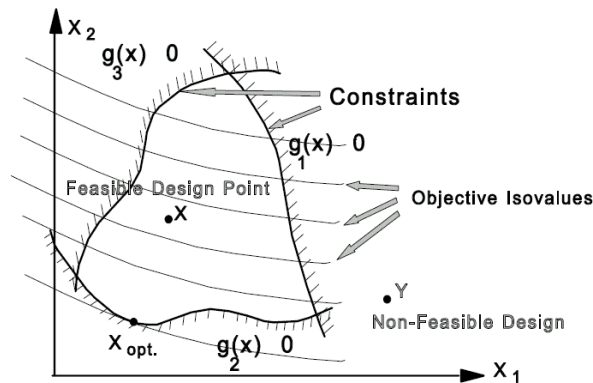
Figure 2.1: The design space, feasible and unfeasible designs [RR05].

design, and isovalue curves for the objective functions can then be drawn. Inequality constraints $g_i(x)$, $i = 1, 2, 3, ...$, are represented by boundaries, and all points inside the space limited by the boundaries represent the feasible designs.
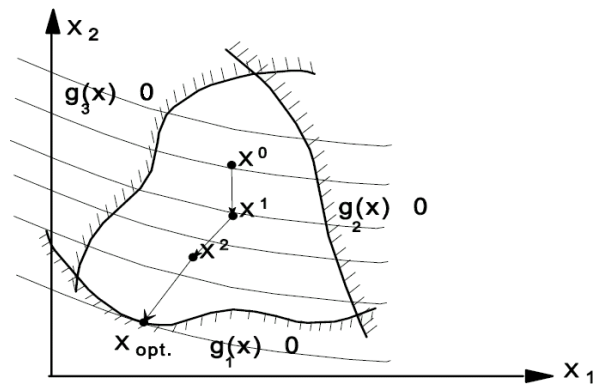
Figure 2.2: The active constraints of the optimization problem, [RR05].

A constraint $g_i(x)$ $i = 1, 2, 3, ...$ is said to be active if a design point lays in the feasible domain frontier representing the constraint. Figure 2.2 depicts the evolution of the design variable x_i, $i = 0, 1, 2$, where the constraint $g_1(x)$ is active at the optimum.

2.2   Topology optimization

Topology optimization is the procedure in which the connection among various portions of the mechanisms are computed, typically from scratch. In what follows, material density reduction scheme will be used to optimize the topology of solids, where material is iteratively removed by reducing the density of an element. Classical objective functions are the maximization of the stiffness or the minimization of the total mass of the mechanism. The result of the optimization process is presented as mass density per element.

Two topology optimization schemes were tested, the first is a module of the Samcef Field ® software package [Sam10]. It's a linear structural analysis driver that uses CONLIN, a gradient-based algorithm to carry out the structural optimization. Results are displayed in a color-scale that indicates where the mass of material should be placed. The second one is the scheme presented by Sigmund [Sig01, ACS+01], which is an heuristic approach to topology optimization programmed in Matlab ®.

2.2.1   Samcef Field® CONLIN algorithm

Convex linear programming (CONLIN), was proposed by Fleury [Fle79, Fle89a] to solve basic sizing problems. The algorithm builds an approximation of the design space and solves the approximate problem, and the estimation/solving loop is repeated until convergence. The design space is only limited by the constraints and bounds on variables as the approximation of the objective function is monotonic [RR02]. Considering any differentiable function $f(x)$, the following linearization scheme yields a convex approximation:

$$f(x) \approx f(x_i{}^0) + \sum_{>0} \frac{df(x)}{dx_i{}^0} \left(x_i - x_i{}^0 \right) - \sum_{<0} \frac{df(x)}{dx_i{}^0} \left(x_i{}^0 \right)^2 \left(\frac{1}{x_i{}^0} - \frac{1}{x_i} \right) \quad (2.2)$$

This algorithm exhibits good convergence properties for sizing and shape optimization problems, however, in some cases the convex approximation might not be appropriate, leading to slow convergence or oscillations [Sam10].

Topology optimization of a hyperstatic beam with a center load

The topology optimization of a simple, clamped-clamped (hyperstatic) beam is analyzed. The objective is to maximize the stiffness and to minimize the material mass of the beam, such as to use the optimum amount of material to support the imposed load. The beam is made of polypropylene, with Young modulus $E = 1.4 \times 10^3 \, \text{N/mm}^2$ and Poisson ratio $\nu = 0.25$, and it's assumed to have a constant rectangular cross section (12 mm wide, 12 mm high), and it's 80 mm long.
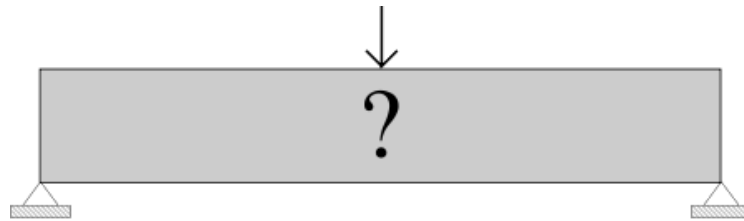
Figure 2.3: The clamped-clamped beam model.

The model is actuated by a vertical resultant force $F = 1000 \, \text{N}$ on its middle length (Figure 2.3), and was discretized using 1140 linear-hexahedral elements. The maximum number of iterations was set to 20, the minimum density value as a 0.01 fraction, and the target volume relative to the mass as a 0.3 ratio. Results are depicted in Figure 2.4.

2.2.2 Sigmund's algorithm

Sigmund's 2D topology optimization algorithm [Sig01, ACS$^+$01] is a linear method written in Matlab® based on evolutionary design [XS97]. In order to control the density distribution a *power law* called SIMP (Solid Isotropic Material with Penalization) [Be89, ZHS98] is used, in which material properties are assume constant within each element of the design domain, and the variable are the elements relative density. This topology optimization problem can be written as
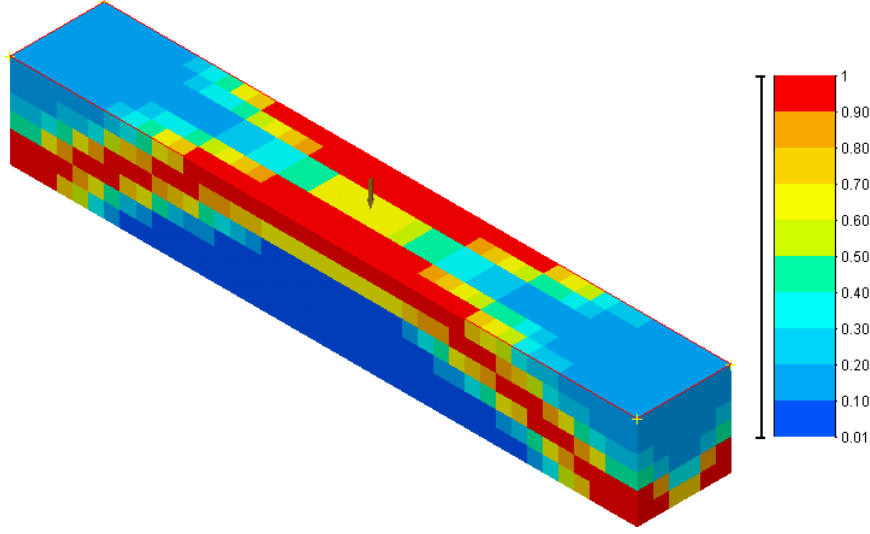
Figure 2.4: Results of the clamped-clamped beam topology optimization performed in Samcef Field®The objective was to maximize the stiffness while minimizing the material mass. The color-scale indicates the location of the material mass (red means maximum density, and blue means minimum density).

$$
\begin{cases}
\text{minimize}: \ c\left(\boldsymbol{x}\right) = \boldsymbol{U}^{T}\boldsymbol{K}\boldsymbol{U} \\
\text{subjected to}: \ \frac{V(\boldsymbol{x})}{V_0} = f \\
: \ \boldsymbol{K}\boldsymbol{U} = \boldsymbol{F} \\
: \ \boldsymbol{0} < \boldsymbol{x}_{min} \leq \boldsymbol{x} \leq \boldsymbol{1}
\end{cases}
$$

where $\boldsymbol{U}$ and $\boldsymbol{F}$ are the global displacement and force vectors, respectively, $\boldsymbol{K}$ is the global stiffness matrix, $\boldsymbol{x}$ is the vector of design variables, $\boldsymbol{x}_{min}$ is a vector of minimum relative densities (non-zero to avoid singularity), $V\left(\boldsymbol{x}\right)$ and V_0 are the material volume and design domain volume, respectively, and f is the volume fraction. It uses the heuristic updating approach proposed by Bendsøe [Be95].

Topology optimization of a hyperstatic beam with a center load

The clamped-clamped (hyperstatic) beam is solved with Sigmund's 2D topology optimization algorithm. It is discretized with 80 elements in the horizontal direction, and 12 elements in the vertical direction. The model is actuated by

a vertical resultant force on its middle length. The minimum density value as a 0.01 fraction, and the target volume relative to the mass as a 0.3 ratio. It took 80 iterations to converge to the optimal result, depicted in Figure 2.5, where the color-scale indicates the location of the material mass. The results are almost identical to the ones obtained previously with Samcef Field® topology optimization, Figure 2.4.
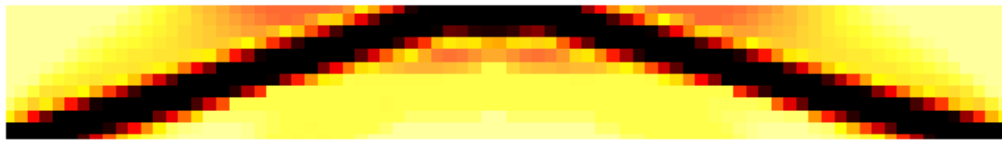
Figure 2.5: Topology optimization solved by Sigmund's algorithm for the clamped-clamped beam shown in Figure 2.3. The color-scale indicates the location of the material mass (dark color means maximum density, and light color means minimum density). Note the similarities with the optimization scheme of Figure 2.4.

2.2.3 Topology optimization conclusions

Two separate topology optimization schemes were applied to solve structural optimization problems, where the objective function was to maximize the stiffness of the structure subjected to the minimization of the material volume. The main advantages and disadvantages of this procedure are:

Advantages

- The structure is automatically generated by the algorithm incresing the density of the elements according to the objective function.

- The results are independent of prior design choices.

Disadvantages

- Topology optimization algorithms assume geometrically linear mechanical behavior, hence, inaccurate results may be obtained in systems undergoing large-displacements.

- The computational cost increases as more elements are used to discretize the domain.

2.3   Shape optimization

In this section, structural optimization algorithms will be applied in a shape optimization problem which deals with computing the optimum shape of the ventilation holes of a turbine disc, such that it maximizes the cross section area of an air channel used to cool the blades and minimizes the equivalent stress in the surroundings of the hole [ARFC06]. In shape optimization, gradient-based algorithms are widely used: *sequential quadratic programming* (SQP), *generalized method of moving asymptotes* (GMMA), and *globally convergent method for moving asymptotes* (GCM) among others [Van84].

2.3.1   GMMA Algorithm

Svanberg [Sva87, Sva07] proposed the *generalized method of moving asymptotes*, in which the approximation of a differentiable function $f(x)$ in GMMA has the form [ZFD96]

$$f_j(x) \approx c_j + \sum_{>0} \frac{p_{ij}}{(u_{ij} - x_i)} + \sum_{<0} \frac{q_{ij}}{(x_i - l_{ij})} \qquad (2.3)$$

in which l_{ij} and u_{ij} are the asymptotic parameters, p_{ij} and q_{ij} depend on the sign of the derivatives, and c_j is

$$c_j \approx f_j\left(x^k\right) - \sum_{>0} \frac{\partial f_j\left(x^k\right)}{\partial x_i} \left(u_{ij} - x_i^k\right) + \sum_{<0} \frac{\partial f_j\left(x^k\right)}{\partial x_i} \left(x_i^k - l_{ij}\right). \qquad (2.4)$$

The main property of GMMA is that each function $f(x)$ has its proper moving asymptote l_{ij} or u_{ij} for each design variable x_i, and this allows to treat each constraint and the objective function independently [Sva07]. The algorithm has monotonous behavior, as the sign of the first order derivative remains unchanged despite change of values of the design variables, making this method

suitable for structural sizing problems where stress and displacement are constraints, in which objective function and constraints vary quasi-monotonously with respect to design variables.

2.3.2 GCM Algorithm

Originally proposed by Svanberg [Sva87], the *globally convergent method for moving asymptotes* (GCM) derives from GMMA. It is a second-order method suitable for optimization problems where the objective function has a nonlinear response to the design variables x_i, and at each iteration i it requires numerical data computed at a previous iteration $i - 1$ (the first iteration is always of first order). The approximation of a function $f(x)$ (differentiable) is [BDF02, RR05]

$$f_j(x) \approx c_j + \sum_{>0} \frac{p_{ij}}{(u_{ij} - x_i)} + \sum_{<0} \frac{q_{ij}}{(x_i - l_{ij})} \tag{2.5}$$

where

$$c_j \approx f_j\left(x^k\right) - \sum_{>0} \frac{\partial f_j\left(x^k\right)}{\partial x_i} \left(u_{ij} - x_i^k\right) + \sum_{<0} \frac{\partial f_j\left(x^k\right)}{\partial x_i} \left(x_i^k - l_{ij}\right). \tag{2.6}$$

Both asymptotes are used simultaneously in GCM and in consequence, p_{ij} and q_{ij} take strictly positive values, making the solution a non-monotonous approximation. The values of p_{ij} and q_{ij} are defined introducing an extra parameter ρ_j that depends on derivatives $\partial f_i\left(x^0\right)$ and on the increment of the design variables $(x_i^{max} - x_i^{min})$.

2.3.3 SQP Algorithm

Sequential quadratic programming (SQP) [PCGH96, SZ05, Sch05] is a *feasible search direction* algorithm. At the beginning of the optimization a search direction $\boldsymbol{S}$ is created, and then a one-dimensional search is performed to improve the design as much as possible in this direction. The direction-finding problem becomes [Van84]

$$\begin{cases} \text{minimize} & Q(\boldsymbol{S}) = \boldsymbol{F}(\boldsymbol{x}) + \bigtriangledown\boldsymbol{F}(\boldsymbol{x}) \cdot \boldsymbol{S} + \frac{1}{2}\boldsymbol{S}^T\boldsymbol{B}\boldsymbol{S} \\ \text{subject to} & \bigtriangledown g_j(\boldsymbol{x}) \cdot \boldsymbol{S} + \delta_j g_j(\boldsymbol{x}) \leq 0 \qquad j = 1, ...m \\ & \bigtriangledown h_k(\boldsymbol{x}) \cdot \boldsymbol{S} + \overline{\delta}h_k(\boldsymbol{x}) \leq 0 \qquad k = 1, ...l \end{cases}$$

Here, design variables are the components of $\boldsymbol{S}$. Matrix $\boldsymbol{B}$ is a positive definite matrix which is initially the identity matrix, and will be updated on subsequent iterations. The scalars δ and $\overline{\delta}$ are problem-dependent and are used to prevent inconsistencies between the linearized constraints [Fle89b]. The parameter $\overline{\delta}$ should be chosen as near to 1 as possible, and values of $\overline{\delta} = 0.90$ a 0.95 works well [Van84]. Once determined the search direction $\boldsymbol{S}$, the design is updated solving a one-dimensional search problem.

2.3.4   Shape optimization example

The ventilation of the blades (cooling) is used in jet engines to increase the gas temperature inside the turbine thus increasing power and thermal efficiency of the engine without increasing the temperature of the blades beyond safe temperature limits, preserving their expected lifetime. Its achieved by taking cold air from the compressor and passing it through ventilation holes machined on a rotating disc located in front of the blades. The shape of the holes play a major role in the air flow and in the stress distribution of the disc.

The diameter of the disc is 520 mm, and posses 37 ventilation holes machined in a periodic pattern. The axial-symmetry of the disc was taken in advantage for modeling, resulting in an 4.86 angle minimum pattern. This three-dimensional paramemtric model is depicted in Figure 2.6.

Given that the objective function is to minimize the equivalent stress subjected to a ventilation area constraint V_A, specified as 127 mm$^2 \leq V_A \leq$ 141 mm^2. The design variables were chosen as the major and minor radius of the hole, RA and RB respectively[1]. The bounds for the design variables are: 6 mm $\leq RA \leq$ 12 mm, and 4 mm $\leq RB \leq$ 8 mm. The parametric model defined upon both of this radius depicted in Figure 2.7.

---

[1]This represents the most general case, in which the resulting shape of the hole may be elliptic. The circular shape is a particular case, in wich $RA = RB$.
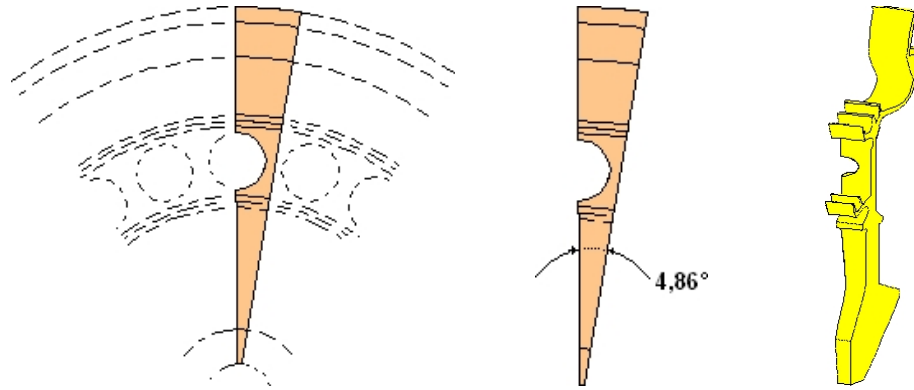
Figure 2.6: The axial-symmetrical model of the disc: the periodic pattern (left), the 4.86 angle minimum pattern (middle), and the resulting three-dimensional model (right).
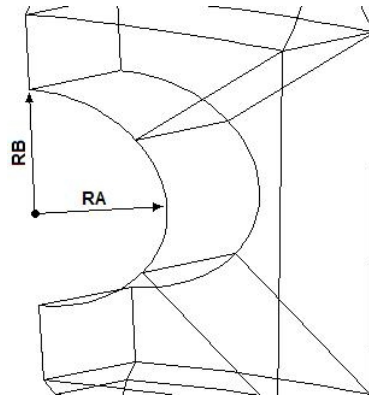
Figure 2.7: The design variables of the parametric model are the major and minor radius of the hole, RA and RB respectively.

At each iteration of the optimization problem the model is re-meshed. The structured mesh of 6600 hexaedral elements depicted in Figure 2.8 is used to maintain the topology of the model in each re-meshing process.

The disc is made of an aluminum alloy with Young modulus $E = 2.1 \times 10^{11}$ N/m^2 and density $\rho = 8.2 \times 10^3$ Kg/m^3, and rotates at an angular speed $\omega = 1772$ rad/s. Boundary conditions are shown in Figure 2.9.

The shape optimization problem can be stated as follows:
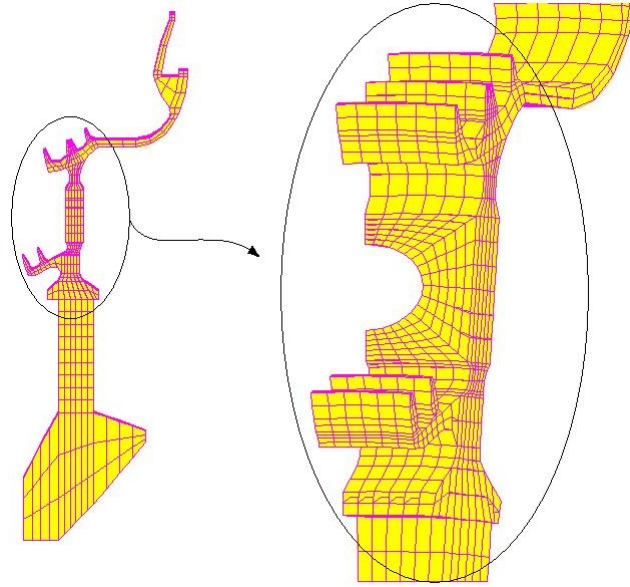
Figure 2.8: Structured mesh of 6600 hexaedral elements.

Minimize: the equivalent stress

$$f_{obj} = \min \ (\boldsymbol{\sigma}_{equiv}) \ \forall \ \text{elements} \tag{2.7}$$

Subject to: an specified range for the ventilation area

$$127 \ \text{mm}^2 \leq V_A \leq 141 \ \text{mm}^2 \tag{2.8}$$

Modifying: the set of design variables

$$6 \ \text{mm} \leq RA \leq 12 \ \text{mm} \qquad 4 \ \text{mm} \leq RB \leq 8 \ \text{mm} \tag{2.9}$$

Results of the shape optimization problem

Two separate optimization problems were computed for each algorithm. The BOSS/Quattro [RR05] optimization software was used, along with Mecano and Asef modules (nonlinear and linear analysis modules, respectively) to carry out the coupled thermo-mechanical analysis of the problem. A maximum number of 100 iterations was adopted. The results are summarized in what follows.
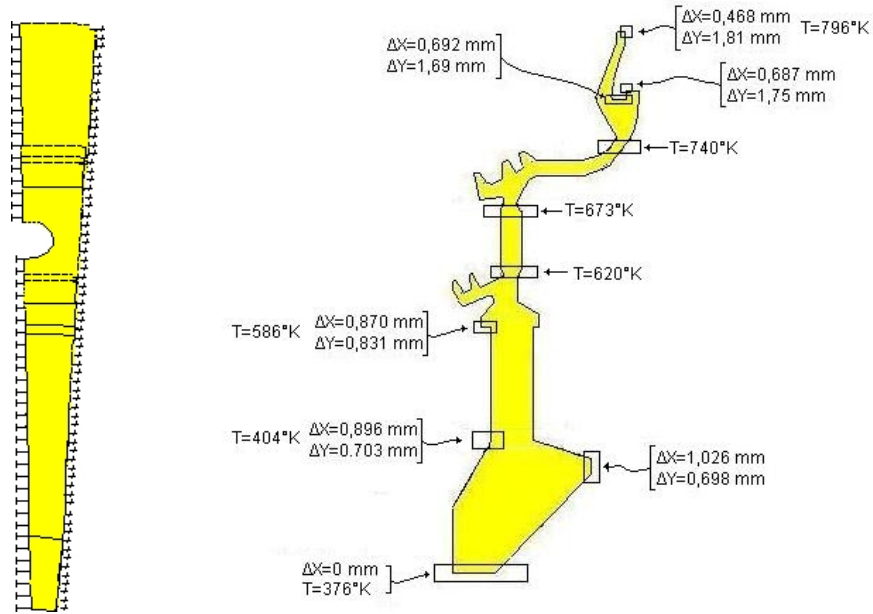
Figure 2.9: The boundary conditions of the model: symmetry conditions (left), and imposed displacements and temperatures (right).

The first algorithm used for the shape optimization problem was GMMA, which computed 82 iterations in the first run and 93 iterations in the second one, showing the worst behavior of the three algorithms due to its oscilating behaviour, and because it does not tend to reach a convergence value. The best result obtained with GMMA was $\boldsymbol{\sigma}_{equiv} = 176$ mN/mm^2 and $V_a = 136.4$ mm^2. The highlights of GMMA were:

- none of the constraints were violated.

- very oscilating behaviour.

- there is no tendency to reach convergence at all.

The next algorithm tested was GCM, which computed 100 iterations in both runs. GCM showed the best behavior of the three algorithms, with very narrow oscillation values and fast convergence. The drawback of this algorithm is that the minimum area constraint was violated. The best result of GCM was $\boldsymbol{\sigma}_{equiv} = 163.5$ mN/mm^2 and $V_a = 108$ mm^2, and the highlights were:

- showed the best behaviour of the three algorithms.

- proved fast convergence.

- narrow oscillation of the results.

- the lowest bound of the constrain was violated.

The last algorithm investigated was SQP, which showed oscillating behavior until half of the study, from which oscillations diminishes and convergence is reached. It computed 54 iterations in the first run and 57 iterations in the second one. None of the constraints were violated and the results obtained are feasible. The only drawback of SQP is *local convergence*, present in both runs performed here, which makes this algorithm unstable. The best result obtained was $\boldsymbol{\sigma}_{equiv} = 165$ mN/mm^2 and $V_a = 131$ mm^2, and:

- none of the constraints were violated.

- proved acceptable convergence.

- it had local convergence, making it unstable.
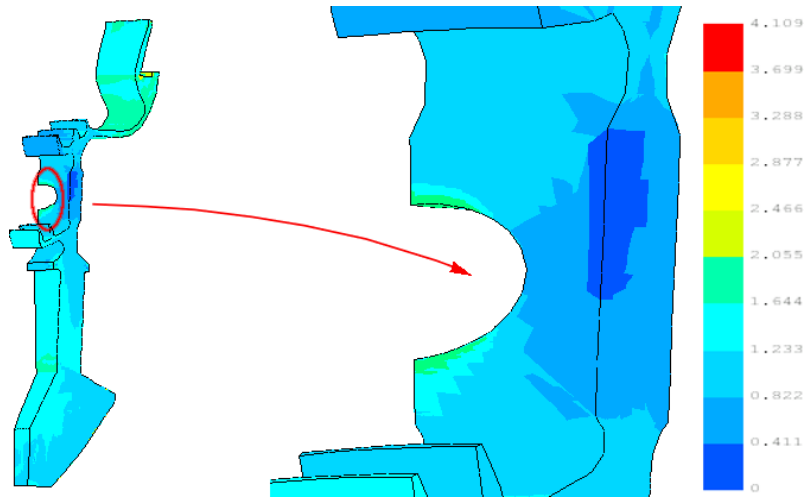
Figure 2.10: Ventilation hole optimization results: maximum equivalent stress.

From this, we conclude that the problem was successfully solved. A smooth stress distribution was achieved in the surroundings of the ventilation hole

(Figure 2.10, and the area of the ventilation hole is between the specified bounds. The geometry of the ventilation hole resulted elliptic in all cases. The 3D model permitted to analyze other phenomena, such as flexural stress. The best result was obtained at iteration 55 of the second run of SQP (Table 2.1), [ARFC06].

Maximum equivalent stress	Ventilation Surface	RA	RB
165 mN/mm^2	131 mm^2	9.17 mm	4.52 mm

Table 2.1: Best results of the ventilation hole optimization problem.

2.4 Size optimization

The design of mechanisms by size optimization will be treated in this section, in order to accomplish compliant-segment motion generation tasks [AFPC07]. The behavior of a *partially compliant mechanism* (*partially* referring to the presence of some rigid body or kinematic pair in the mechanism) is similar to a rigid-body mechanism where a large portion of the mechanism is stiff and flexibility is reduced to a minimum number of regions. The design of these type of mechanisms is in general performed using rigid-body replacement, starting from rigid-synthesis results. *Fully compliant mechanism* behave quite differently since flexibility is evenly distributed, and its motion is obtained from the deflection of an elastic structure.
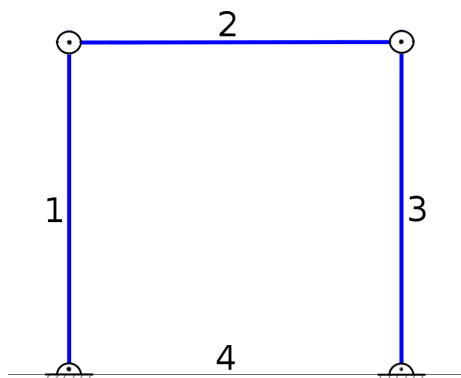
Figure 2.11: A rigid four-bar mechanism. Link N=4 is grounded link.

The rigid four-bar mechanism is the simplest movable linkage, and consists in links attached to two others by single joint or pivot, forming a close-loop kinematic chain (Figure 2.11). In general they obbey *Grashof's* law that states that for at least one of four links to have full rotation, the following inequality must hold:

$$s + l \leq p + q \tag{2.10}$$

being s the length of the shortest link, l the length of the longest link, and p and q the length of the remaining links. Its degrees of freedom (DOF) can be obtained using *Grueber's* equation

$$DOF = 3(n - 1) - 2K_l - K_h \tag{2.11}$$

in which n is the total number of links, K_l is the total number of lower kinematic pairs, K_h is the total number of higher kinematic pairs. A planar rigid four-bar mechanisms has 4 linkages ($n = 4$), 4 low kinematic pairs ($K_l = 4$), and lacks of high kinematic pairs ($K_h = 0$), so application of *Grueber's* equation yields

$$DOF_{r_4bar} = 3(4 - 1) - 8 = 1 \tag{2.12}$$

The compliant four-bar mechanism has 2 low kinematic pairs ($K_l = 2$) and 2 links (one rigid and one compliant, $n = 2$). Application of *Grueber's* equation yields

$$DOF_{c_4bar} = 3(2 - 1) - 4 = -1 \tag{2.13}$$

and results a hyperstatic structure. However, the lack of degrees of freedom can be overcomed by the flexibilities of compliant joints. Addressing motion-generation in a compliant mechanism implies moving flexible links through a sequence of discrete prescribed *precision shapes* in addition to the precision points of rigid-body motion, involving the guidance of a flexible link instead of a rigid body.

Saggere and Kota [SK01] introduced this problem and called this task

compliant-segment motion generation. In his work, flexible members were modeled as a series of small, straight, rigid elements connected end to end through linear torsional springs. This requires disassembling the mechanism and designing each part separately, along with the imposition of appropriate boundary conditions to accomplish identical displacements and rotations at the fusing ends (internal forces and moments should be equal in magnitude but opposite in sign), and therefore all parts are independently in equilibrium. Al last, the synthesis task is performed through optimization by a numerical approach.

One of the drawbacks of this discretization is that it does not account for the shear stress that may appear in the links as they deflect from their initial to their final configuration. Another drawback is the need to split the mechanism into individual links to carry out the synthesis task separately in each one of them. The approach used in this chapter conceives a more realistic proposal to the systematic synthesis of compliant, single-loop mechanism. An optimization scheme coupled with finite element models grants the synthesis of all links simultaneously, [AFPC07]. In an initial approach, compliant links are modeled using a two-dimensional beam finite element with shear deformation, and afterward, using a three-dimensional large-deflection beam element. The extension of this method to synthesize multi-loop mechanisms can be easily arranged.

Many potential applications of compliant-segment motion generation can be envisioned. For instance, certain segments of a large flexible space structure that functions as a reflective surface may be oriented in different directions and also shaped into different curvatures for the purposes of modulating the characteristics of reflecting sound or light waves [LK03]. Similar applications are also practicable at micro level, i.e. micro-mirrors for controlled reflection of light. Other potential application is the design of stamps, where the geometry of a flexible stamp may require contoured rigid surfaces that have differently shaped curvatures. The common feature in these applications is that the required task can be efficiently accomplished by a suitable fully compliant four-bar mechanism.

2.4.1   Problem description

In four-bar mechanisms, one of the links is called the *coupler link*, and is the only one that can trace paths of arbitrary shape because it is not rotating about a fixed pivot. One of the grounded links serves as the *input or driver link*, which may derive its motion by some sort of driving transmission (e.g. by hand, by an electric motor or a hydraulic or pneumatic cylinder). The remaining grounded link is called the *follower or driven link*, because its rotation merely follows the motion determined by the input and coupler link motion. Figure 2.12 depicts a typical four-bar mechanism.
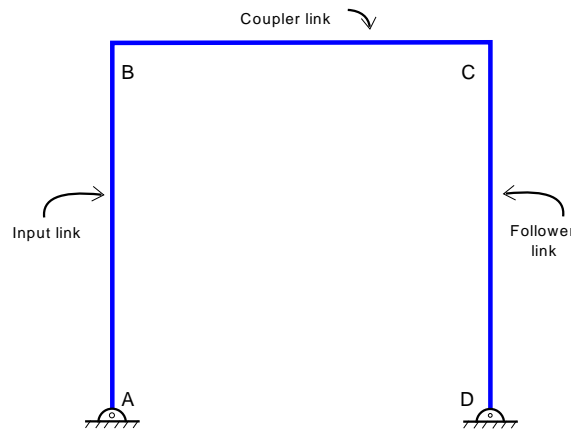
Figure 2.12: A compliant four-bar mechanism, and the classification of its links.

Previous research on this type of mechanisms comprised at least one moving rigid link, and the coupler-link was always considered a rigid member since the motion generation objective was based on the definition for conventional rigid-link mechanisms. In this chapter, the synthesis task is to guide the compliant coupler link with initial smooth configuration to another specified (also smooth) configuration, as depicted in Figure 2.13. The motion from the initial to the final configuration of the compliant coupler link is called *mechanism task*.

The two ends of the coupler-link are connected to the ends of the input and follower links (the ones to be synthesized), and the three segments form one continuous (compliant) planar link. The motion of an unconstrained planar
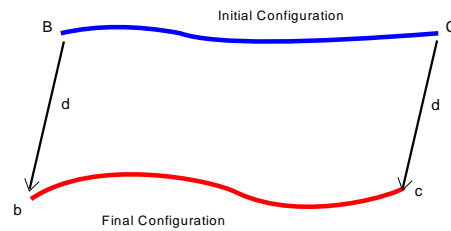
Figure 2.13: Mechanism task: the guiding of the flexible coupler-link.

link is described by three degrees of freedom: two displacements (one in the x coordinate and the other in the y coordinate) and one rotation around an axis perpendicular to the xy plane. The use of a lower kinematic pair removes two degrees of freedom, allowing only rotations about the hinged end. If a planar link is clamped, then all its degrees of freedom are removed. The free end of the follower link may either be pinned or clamped to the ground. However, if the mechanism is to be actuated from the free end of the input link by torque or rotation, the only admissible support is a lower kinematic pair. This situation is represented in Figure 2.14, where B-C is the coupler link to be guided to an specified final configuration b-c, and A-B and C-D are the two remaining links to be synthesized. A-B-C-D represents the initial configuration and A-b-c-D the final configuration of the mechanism.
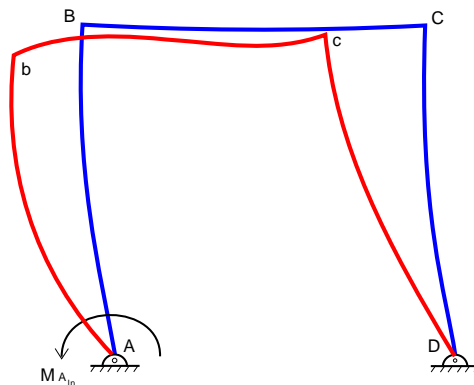
Figure 2.14: Specified initial and final configuration of the mechanism, ABCD and AbcD respectively.

According to this, a more formal definition of the problem can be stated: *given a compliant segment and its initial and final desired configuration, syn-*

thesize the input and follower links of a compliant four-bar mechanism and the corresponding input rotations that generate the prescribed compliant-segment motion generation. The synthesis tasks are to determine:

- optimal shapes and sizes of segments A-B and C-D.

- locations of the pivots A and D.

- input torque and/or rotation in pivot A.

2.4.2   Discretization of the mechanism: beam formulations

It was stated before that the discretization of the mechanism in straight rigid-links connected end to end through linear torsional springs neglects the shear deformation that could be induced in the compliant links as they deflect, and this motivated the use of non-linear beam finite elements to model the mechanism. Two formulations were tested: the first one is a two-dimensional beam finite element based in Timoshenko's beam theory (shear deformation of the neutral axis is allowed in this theory) derived by Crisfield [Cri00], and the second one is a three-dimensional large-deflection beam element derived by Cardona and Geradin [CG88, GC00].

2D Beam finite element formulation

The formulation was derived by Crisfield [Cri00] and it assumes the hypothesis that *plane sections, normal to the axis of the beam, remain plain but not necessarily normal to the axis after deflection.* A very similar formulation can be found in the work of Omar and Shabana [OS00]. The highlights are presented in the following paragraphs.

The finite element has initially a general curved geometry, depicted in Figure 2.15. The displacement in the x-axis direction is labeled u, and in the z-axis direction is labeled w. Under the assumption that plane sections remain plane, the value of u at a distance z_l from the centroid can be computed as follows (Figure 2.16)
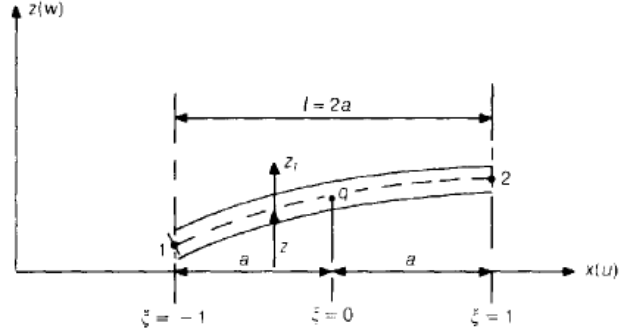
Figure 2.15: Initially curved beam element, [Cri00].

$$u = \bar{u} + z_l \frac{d\theta}{dx} \tag{2.14}$$

being θ the rotation of the normal of the beam, defined by
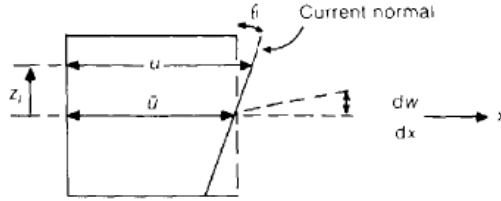
Figure 2.16: Detail of the beam element with shear deformation, [Cri00].

$$\theta = \frac{dw}{dx} + \phi \tag{2.15}$$

where ϕ is the additional rotation induced by the shear strains [On92]. The curvature χ is computed as follows

$$\chi = \frac{d\theta}{dx} \tag{2.16}$$

Assuming elastic properties, the normal force $\boldsymbol{N}$, the moment $\boldsymbol{M}$, and the transverse shear force $\boldsymbol{Q}$ are computed as

$$\boldsymbol{N} = EA\bar{\varepsilon} \qquad \boldsymbol{M} = EI\chi \qquad \boldsymbol{Q} = GA\gamma \tag{2.17}$$

The components of u (displacement in the x direction), w (displacement in

the z direction), and θ (rotation of the normal) are

$$\boldsymbol{u} = (u_1, u_2, \Delta u_q) \qquad \boldsymbol{w} = (w_1, w_2, \Delta w_q) \qquad \boldsymbol{\theta} = (\theta_1, \theta_2, \Delta\theta_q) \qquad (2.18)$$

where suffix 1 refers to the first node, suffix 2 refers to the second node of the element, and suffix q is a central node. The shape functions for u, w and θ are quadratic hierarchical functions, such that the interpolation is carried out in the form

$$\begin{aligned}
\overline{u} &= \boldsymbol{h_u^T u} & (2.19) \\
w &= \boldsymbol{h_w^T w} & (2.20) \\
\theta &= \boldsymbol{h_\theta^T \theta} & (2.21)
\end{aligned}$$

where functions $\boldsymbol{h_u} = \boldsymbol{h_w} = \boldsymbol{h_\theta} = \boldsymbol{h}$ are given by

$$\boldsymbol{h^T} = \frac{1}{2}\left(1 - \xi, 1 + \xi, 2\left(1 - \xi^2\right)\right) \qquad (2.22)$$

The differentiation of Equations (2.19), (2.20) and (2.21) permits the computation of the strains measures

$$\begin{aligned}
\frac{d\overline{u}}{dx} &= \boldsymbol{u} = \boldsymbol{b_u^T u} & (2.23) \\
\frac{dw}{dx} &= \boldsymbol{b_w^T w} & (2.24) \\
\frac{d\theta}{dx} &= \boldsymbol{b_\theta^T \theta} & (2.25)
\end{aligned}$$

where functions $\boldsymbol{b_u} = \boldsymbol{b_w} = \boldsymbol{b_\theta} = \boldsymbol{b}$ are obtained by differentiation of Equation (2.22)

$$\boldsymbol{b^T} = \frac{1}{l}\left(-1, 1, -4\xi\right) \qquad (2.26)$$

and the axial strain ε_x, the shear strain γ and the curvature χ are computed

as follows

$$\bar{\varepsilon} \;=\; \boldsymbol{b_u^T u} + \frac{1}{2}\left(\boldsymbol{b_w^T w'}\right)^2 - \frac{1}{2}\left(\boldsymbol{b_w^T z}\right)^2 \tag{2.27}$$

$$\gamma \;=\; \theta + \frac{dw}{dx} = \boldsymbol{b_w^T w} + \boldsymbol{h_\theta^T \theta} \tag{2.28}$$

$$\chi \;=\; \frac{d\theta}{dx} = \boldsymbol{b_\theta \theta} \tag{2.29}$$

The vector of internal forces is

$$\boldsymbol{q_i^T} = \left(\boldsymbol{U_i^T}, \boldsymbol{W_i^T}, \boldsymbol{T_i^T}\right) \tag{2.30}$$

where the T_i terms are work-conjugate to the nodal rotations θ. The components of q_i are given by

$$\boldsymbol{U_i} = \int N \boldsymbol{b_u} dx \tag{2.31}$$

$$\boldsymbol{W_i} = \int \left(N\left(\boldsymbol{b_w^T w'}\right) b_w + Q \boldsymbol{b_w}\right) dx \tag{2.32}$$

$$\boldsymbol{T_i} = \int \left(M \boldsymbol{b_\theta} + Q \boldsymbol{h_\theta}\right) dx \tag{2.33}$$

At last, the stiffness matrix is obtained in the usual manner by differentiation of the internal force vector.

Large-displacement beam finite element formulation

A large-displacement, non-linear beam finite element will also be used to discretize the mechanism. The model presented here was derived by Cardona and Géradin [CG88, GC00] to model highly flexible multibody systems. It relies on the following kinematic hypotheses:

- the beam is initially straight,

- beam cross sections remain plane during deformation, and

- shear deformation of the neutral axis is allowed.
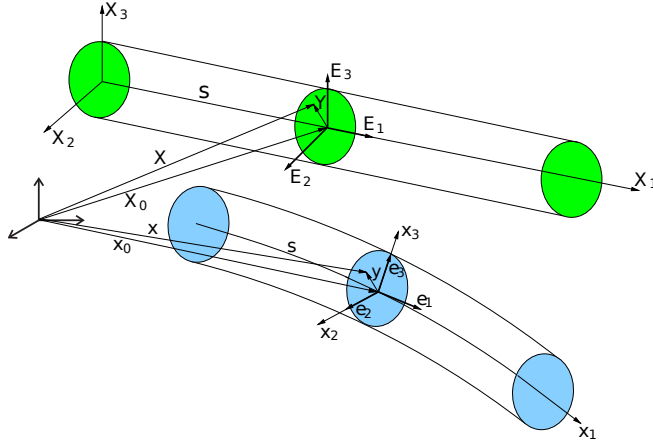
Figure 2.17: Beam kinematics, [CG88, GC00]

With reference to Figure 2.17, the position of any point $\boldsymbol{X}$ in the reference configuration is

$$\boldsymbol{X} = \boldsymbol{X}_0 + \boldsymbol{Y} \tag{2.34}$$

where $\boldsymbol{X}_0$ is the reference position of a cross section at a distance s from the origin, $\boldsymbol{Y}$ is the position of $\boldsymbol{X}$ in the cross section, relative to $\boldsymbol{X}_0$. After elastic deformation, the basis $\{\boldsymbol{E}_1, \boldsymbol{E}_2, \boldsymbol{E}_3\}$ transforms to the basis $\{\boldsymbol{e}_1, \boldsymbol{e}_2, \boldsymbol{e}_3\}$ according to the orthogonal transformation

$$\boldsymbol{e}_i = \boldsymbol{R}\boldsymbol{E}_i \qquad i = 1, 2, 3 \tag{2.35}$$

where $\boldsymbol{R}$ is a linear operator on the abstract three dimensional space and represents the physical rotation between the two basis. The position of the same point can be written as

$$\boldsymbol{x} = \boldsymbol{x}_0 + \boldsymbol{R}\boldsymbol{Y} \tag{2.36}$$

where $\boldsymbol{x}_0$ is the new absolute position of the cross-section. The Cartesian rotational vector $\boldsymbol{\psi}$ is used to parameterize rotations, defined as the vector

whose direction is that of the rotation axis $\boldsymbol{n}$ and whose length is equal to the amplitude of the rotation ψ:

$$\boldsymbol{\psi} = \boldsymbol{n}\psi \tag{2.37}$$

The rotation operator $\boldsymbol{R}$ (a function of $\boldsymbol{\psi}$) in three dimensional space is completely determined by means of the Rodrigues' formulae:

$$\boldsymbol{R}(\boldsymbol{\psi}) = \boldsymbol{I} + \frac{\sin\psi}{\psi}\widetilde{\boldsymbol{\psi}} + \frac{1 - \cos\psi}{\psi^2}\widetilde{\boldsymbol{\psi}}\widetilde{\boldsymbol{\psi}} \tag{2.38}$$

where $\boldsymbol{I}$ is the identity matrix and, from now on, $\widetilde{*}$ is the spin operator applied to the vector $*$. Since $\boldsymbol{\psi}$ suffices to completely describe the rotation $\boldsymbol{R}$, the set of variables $\{\boldsymbol{x}_0, \boldsymbol{\psi}\}$ are used instead of $\{\boldsymbol{x}_0, \boldsymbol{R}\}$ as the unknown of the current problem.

The deformation of the neutral axis $\boldsymbol{\Gamma}$ and the curvature $\boldsymbol{K}$ are material measures, defined by

$$\boldsymbol{\Gamma} = \boldsymbol{R}^T \left(\frac{d\boldsymbol{x}_0}{dx_1} - \boldsymbol{e}_1 \right) \tag{2.39}$$

$$\boldsymbol{K} = \boldsymbol{T}\frac{d\boldsymbol{\psi}}{dx_1} \tag{2.40}$$

being $\boldsymbol{T}$ the tangent operator

$$\boldsymbol{T}(\boldsymbol{\psi}) = \boldsymbol{I} + \frac{\cos\psi - 1}{\psi^2}\widetilde{\boldsymbol{\psi}} + \left(1 - \frac{\sin\psi}{\psi}\right)\widetilde{\boldsymbol{\psi}}\widetilde{\boldsymbol{\psi}} \tag{2.41}$$

The equilibrium equations are formulated in the deformed configuration: $\boldsymbol{n}$ and $\boldsymbol{m}$ are the resultant force and moment with respect to $\boldsymbol{X}_0$ of the tractions acting over the surface S, and $\bar{\boldsymbol{n}}$ and $\bar{\boldsymbol{m}}$ the external force and moment per unit length at $\boldsymbol{X}$. Assuming static conditions, equilibrium equations are

$$\frac{d\boldsymbol{n}}{ds} + \bar{\boldsymbol{n}} = \boldsymbol{0} \tag{2.42}$$

$$\frac{d\boldsymbol{m}}{ds} + \frac{d\boldsymbol{x}_0}{ds} \times \boldsymbol{n} + \bar{\boldsymbol{m}} = \boldsymbol{0} \tag{2.43}$$

The material counterparts of stress and loads resultants are

$$N = R^T n \tag{2.44}$$

$$M = R^T m \tag{2.45}$$

and can be computed following the constitutive relations used in [CG88], in which the material remains in the linear elastic range. Under these hypotheses, the following constitutive equations apply

$$N = C^N \Gamma \tag{2.46}$$

$$M = C^M K \tag{2.47}$$

The unknowns of the problem $\{x_0, \psi\}$ are approximated as follows

$$x_0(s) = \varphi_1(s) x_0^1 + \varphi_2(s) x_0^2 \tag{2.48}$$

$$\psi(s) = \varphi_1(s) \psi^1 + \varphi_2(s) \psi^2 \tag{2.49}$$

where x_0^i and ψ^i are respectively the unknown values of x_0 and ψ at node i, and φ_i is the linear shape function associated to node i, and $i = 1, 2$. The vector Q of nodal unknowns and the matrix φ of shape functions are defined as

$$Q = \begin{bmatrix} x_0^1 \\ x_0^2 \\ \psi^1 \\ \psi^2 \end{bmatrix}, \qquad \varphi = \begin{bmatrix} \varphi_1 I & \varphi_2 I & O & O \\ O & O & \varphi_1 I & \varphi_2 I \end{bmatrix} \tag{2.50}$$

in which O is the 3×3 null matrix and I is the 3×3 identity matrix. Then, equations (2.48) and (2.49) take the matrix form:

$$\begin{bmatrix} x_0 \\ \psi \end{bmatrix} = \varphi Q \tag{2.51}$$

The non-linear system of algebraic equations for the unknowns $\boldsymbol{Q}$ yields

$$\boldsymbol{F}_{int}(\boldsymbol{Q}) - \boldsymbol{F}_{ext} = \boldsymbol{0} \tag{2.52}$$

and this equation is solved with a Newton-Raphson method, where $\boldsymbol{F}_{int}$ and $\boldsymbol{F}_{ext}$ are respectively the vectors of internal and external forces, respectively, given by

$$\boldsymbol{F}_{int} = \int_{\mathcal{B}} \boldsymbol{B}^{T} \boldsymbol{\sigma} ds \tag{2.53}$$

$$\boldsymbol{F}_{ext} = \int_{\mathcal{B}} \boldsymbol{\varphi}^{T} \bar{\boldsymbol{t}} ds \tag{2.54}$$

with

$$\boldsymbol{B} = \begin{bmatrix} \varphi_1' \boldsymbol{I} & \varphi_1 \widetilde{\boldsymbol{i}} & \varphi_2' \boldsymbol{I} & \varphi_2 \widetilde{\boldsymbol{i}} \\ \boldsymbol{O} & \varphi_1' \boldsymbol{I} & \boldsymbol{O} & \varphi_2' \boldsymbol{I} \end{bmatrix}, \qquad \boldsymbol{\sigma} = \begin{bmatrix} \boldsymbol{n} \\ \boldsymbol{m} \end{bmatrix}, \qquad \bar{\boldsymbol{t}} = \begin{bmatrix} \bar{\boldsymbol{n}} \\ \bar{\boldsymbol{m}} \end{bmatrix} \tag{2.55}$$

where $\varphi_1' = d\varphi_1/ds = -1/L$ and $\varphi_2' = d\varphi_2/ds = 1/L$.

2.4.3 Synthesis of the Input and Follower Segments

In the undertaken synthesis problem (figure 2.12) *the initial and loaded shapes of the input and follower links are not known, nor are the tip locations and length of the segment known.* The only data available are the tip loads, displacements and rotations. These inverse problems have, in general, no closed-form solutions, and they require optimization methods in order to be solved. Boundary conditions on the three segments are derived from the specified mechanism task, and optimization is used to *determine the cross-section height and width of segment B-C, shapes and sizes of segments A-B and C-D, the locations of the pivots A and D, and the unknown input torque and/or rotation in pivot A*, so that when it is applied to the synthesized mechanism, its motion agrees with its specified task.

The motion of the coupler link is determined by its known initial configu-

ration (length) and also known final configuration (specified mechanism task). Its change in curvature is translated into displacements and rotations at pivots B and C. The forces and moments induced by this motion are computed by the finite element method. Five finite elements per link are used ($i = 1...n$, where $n = 5$). The objective function is set as the volume of the compliant input and follower links, which has to be minimized (the synthesis aims to satisfy the specified mechanism task, using the minimum amount of material).

The design variables (figure 2.18) are given by:
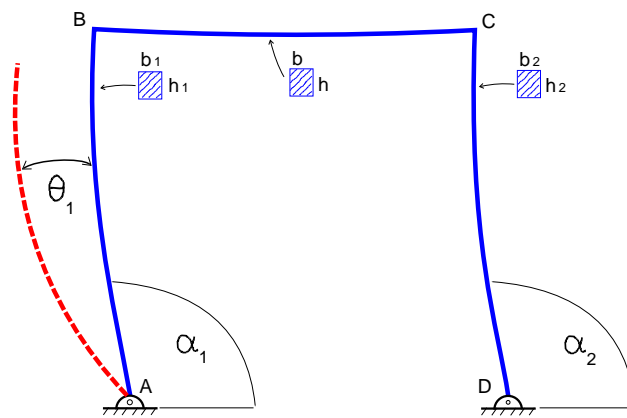
Figure 2.18: The design variables of the problem.

- the length of the links H.

- the cross-section width b.

- the cross-section height h.

- the position angle α.

- the rotation angle θ.

and on the other hand, constraints are:

- the displacements u and w of the coupler link.

- the rotation angle θ of the coupler link.

which are derived from the mechanism task $\bar{t} = t(x, w, \theta)$. From here on, suffix 1 refers to the input and the suffix 2 to the follower link. A weight penalization is added in order to assure that these displacements and rotations are matched. Thus, the optimization problem can be stated as follows:

Minimize: the volume of material

$$f = \sum_{i=1}^{n} (H_i b_i h_i) \tag{2.56}$$

Subject to: the mechanism task

$$t(x, w, \theta) = \bar{t} \tag{2.57}$$

Modifying: the set of design variables

$$X = [H_1, H_2, b, b_1, b_2, h, h_1, h_2, \alpha_1, \alpha_2, \theta_1] \tag{2.58}$$

2.4.4 Optimization algorithms in MATLAB ®

The optimization problem of Equation (2.56) to (2.58) was setup and solved with *fmincon*, the constrained optimization module in MATLAB ® software package [The10]. Constrained minimization is the problem of finding a vector x that is a local minimum to a scalar function $f(x)$ subject to constraints on the allowable x. The aim in constrained optimization is to transform the problem into an easier sub-problem that can then be solved and used as the basis of an iterative process, in which the constrained problem is solved using a sequence of parametrized unconstrained optimizations, which in the limit converge to the constrained problem. Package fmincon uses different optimization algorithms, for this particular problem we used *active-set* and *SQP*. The main advantages of SQP over active-set are [The10]:

- In SQP, bounds are not strict and a step can be exactly on a boundary. This can be beneficial when the objective function or nonlinear constraint functions is undefined or is outside the region constrained by bounds.

- A step in the SQP algorithm might fail, and this means that an objective function or nonlinear constraint function has returned a non-defined value. The algorithm will attempts to take a smaller step, and this adds robustness to the method.

- SQP uses a set of linear algebra routines to solve the problem that are more efficient in both memory usage and speed than the active-set routines.

2.5   Numerical example

In what follows, we are going to compare the optimization results with the reference solution of Saggere and Kota [SK01]. Consider a rectangular flexible beam which is initially straight, and it is required to be guided and deformed to a new specified configuration. The coupler length is $L = 200$ mm. The material properties are: Young modulus $E = 2 \times 10^5$ N/mm^2 and shear modulus $G = 8.33 \times 10^4$ N/mm^2.

The mechanical task is the motion of both ends of the coupler link, which is $d = 10$ mm at an angle $\beta = 5.53^o$, depicted in Figure 2.19. Rotations at the ends are computed from the change in geometry: $\theta_B = -0.1$ rad and $\theta_C = -0.08$ rad, and no external loads are applied.
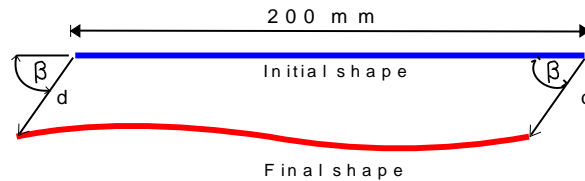
Figure 2.19: Specified task for the compliant coupler-link [SK01].

Next, the compliant input and follower links are synthesized using the optimization scheme described above. In the first example, the grounded ends of these segments are hinged to the ground (both ends are lower kinematic pairs). The chosen bounds for the design variables are summarized in Table 2.2.

Variable	H_1	H_2	c	b_1	b_2	h	h_1	h_2	α_1	α_2	θ_1
Minimum	10	10	5	5	5	5	5	5	0.1 π	0.1 π	-0.4 π
Maximum	120	120	50	50	50	50	50	50	0.9 π	0.9 π	0.4 π

Table 2.2: Bounds for the design variables.

2.5.1   Both free ends hinged to the grounds

The problem solved by Saggere and Kota [SK01] is a partially compliant 4-bar mechanisms with both free ends hinged to the ground, and the amount of material volume used to accomplish the mechanisms task is 8.0543×10^3 mm^3. In what follows the same problem is solved using beam finite elements, improving the results in [SK01] and using less volume to perform the same mechanisms task.

Discretization using Crisfield's beam finite element model

The first optimization was computed using Crisfield's beam finite element model, which is a small-displacement formulation with shear deformation, and the results are summarized in Table 2.3.

Design variable	SQP	Active-set
b_1	9.1680 mm	5.0000 mm
h_1	8.5166 mm	5.0000 mm
H_1	43.9033 mm	50.9249 mm
b_2	5.0116 mm	5.0000 mm
h_2	7.8631 mm	5.0000 mm
H_2	44.8067 mm	69.7444 mm
b_h	5.0000 mm	5.0000 mm
h_h	11.9848 mm	5.0375 mm
α_1	1.5390 rad	1.5630 rad
α_2	1.5506 rad	1.5925 rad
θ_A	-0.3837 rad	-0.3043 rad
M_A	-7.9482$\times 10^5$ Nmm	-5.1675$\times 10^4$ Nmm
Volume	1.7179$\times 10^4$ mm^3	8.0543$\times 10^3$ mm^3

Table 2.3: Hinged-hinged 4-bar partially compliant mechanism. Crisfield's beam finite element model.

As we can see in Figure 2.20, both optimization algorithms yield mechanisms in which the length of the follower link is slightly longer than the length of the input link, and where link deflection is very small under actuation, as should be expected in hinged segments. The volume of material computed using the active-set algorithm is 53% lower than the volume computed using SQP, 8.0543×10^3 mm^3 vs. 1.7179×10^4 mm^3 respectively, demonstrating that active-set proved much more efficient than SQP in this particular problem.
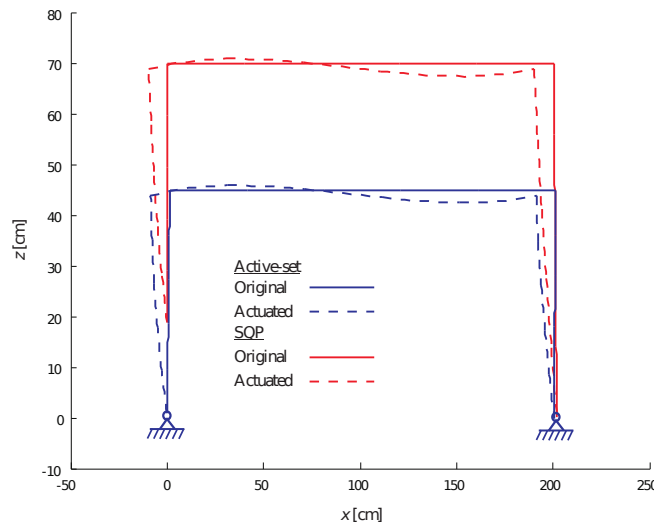
Figure 2.20: Hinged-hinged 4-bar mechanism. Crisfield's beam finite element model. Displacements are in the same scale than the dimensions of the mechanism.

The mechanism task is achieved by using 32% less volume than Saggere and Kota [SK01] in the worst result (SQP), and using 68% less volume in the best case (active-set algorithm).

Discretization using Cardona and Géradin's beam finite element model

The hinged-hinged four-bar mechanisms was later modeled using Cardona and Géradin's non-linear beam finite element, which is a large-displacement model with finite rotations, and the results are summarized in Table 2.4. As we can see in Figure 2.21, the resulting length of the follower link is slightly larger

than the length of the input link. Again, link deflection compared to the overall link length is very small. With this finite element model, both optimization algorithms yielded almost equal material volume. The best solution was obtained with SQP which yielded 8% less volume than active-set, 8.1374×10^3 mm^3 compared to 8.8507×10^3 mm^3 respectively. Reverting the behavior of the optimization coupled with small-displacement beam model, SQP was more efficient than active-set in this particular case.

Design variable	SQP	Active-set
b_1	5.0000 mm	5.0000 mm
h_1	5.0000 mm	5.2074 mm
H_1	50.8619 mm	55.1241 mm
b_2	5.0000 mm	5.2694 mm
h_2	5.0000 mm	5.6528 mm
H_2	69.4608 mm	81.0917 mm
b_h	5.0000 mm	5.0000 mm
h_h	5.1294 mm	5.0000 mm
α_1	1.5568 rad	1.6038 rad
α_2	1.5917 rad	1.5786 rad
θ_A	-0.3118 rad	-0.2762 rad
M_A	-5.3759×10^4 Nmm	-4.5362×10^4 Nmm
Volume	8.1374×10^3 mm^3	8.8507×10^3 mm^3

Table 2.4: Hinged-hinged 4-bar partially compliant mechanism. Cardona and Géradin's beam finite element model.

With this discretization the mechanism task is achieved by using less than halve the volume in Saggere and Kota [SK01]: 68% less volume in the best result (SQP), and 65% less volume in the worst result (active-set).

2.5.2 One free end hinged and the other clamped to the ground

The same optimization problem is performed now with an additional fixation constraint: the free end D of the follower link is now clamped.
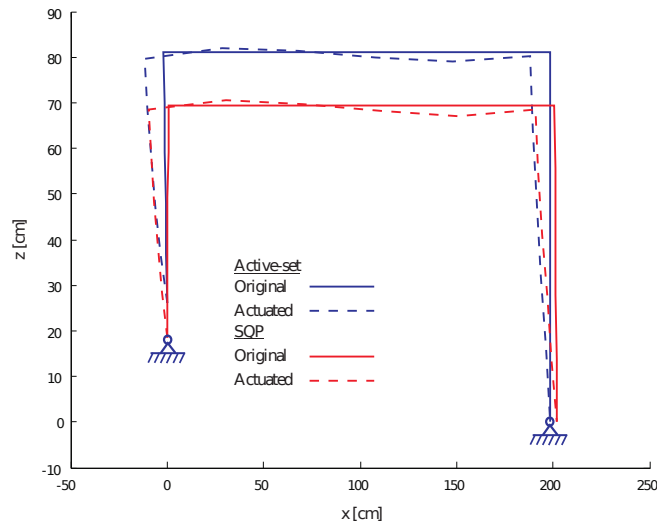
Figure 2.21: Hinged-hinged 4-bar mechanism. Cardona and Géradin's beam finite element model. Displacements are in the same scale than the dimensions of the mechanism.

Discretization using Crisfield's beam finite element model

The results of the optimization with the small-displacement shear deformation model and hinged-clamped fixation set are summarized in Table 2.5.

Design variable	SQP	Active-set
b_1	5.3884 mm	5.0391 mm
h_1	6.0511 mm	6.0128 mm
H_1	53.6244 mm	55.0245 mm
b_2	5.2775 mm	5.1227 mm
h_2	5.4138 mm	5.0000 mm
H_2	99.0420 mm	96.3174 mm
b_h	5.4222 mm	5.0000 mm
h_h	5.5046 mm	5.2979 mm
α_1	1.5666 rad	1.5713 rad
α_2	1.6112 rad	1.6089 rad
θ_A	-0.2951 rad	-0.2833 rad
M_A	-1.0008×10^5 Nmm	-8.4598×10^4 Nmm
Volume	1.0548×10^4 mm^3	9.4321×10^3 mm^3

Table 2.5: Hinged-clamped 4-bar partially compliant mechanism. Crisfield's beam finite element model.

The clamp fixation at D reduces the flexibility of the segment C-d, and in consequence, a segment of greater length than in the hinged-hinged case is needed to perform the same mechanisms task. That is exactly what both algorithms yielded in the hinged-clamp case: mechanisms with longer follower links compared to the hinged-hinged case, Figure 2.22.
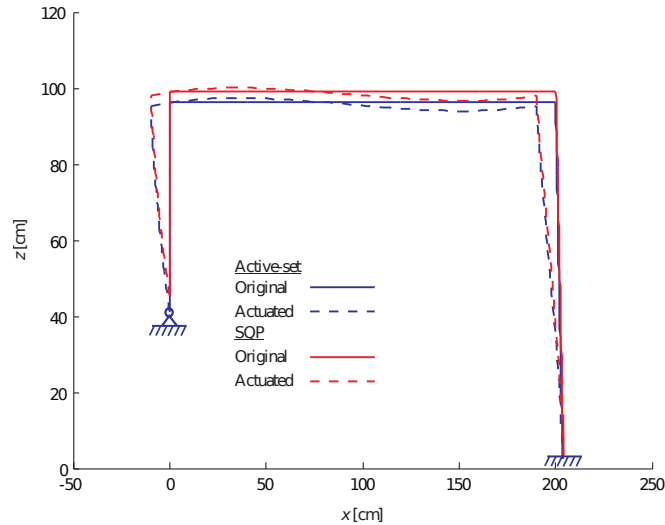
Figure 2.22: Hinged-clamped 4-bar mechanism. Crisfield's beam finite element model. Displacements are in the same scale than the dimensions of the mechanism.

Both algorithms yielded almost the same material volume, in which the best solution of active-set uses 10% less volume than solution computed by SQP, 9.4321×10^3 mm^3 vs. 1.0548×10^4 mm^3 respectively. Once again, the small-displacement shear deformation model gave better results with the active-set algorithm. Comparing this results to the ones of Saggere and Kota [SK01], the same mechanism task is fulfilled with 63% less volume in the best result (active-set), and with 58% less volume in the worst result (SQP).

Discretization using Cardona and Géradin's beam finite element model

The last optimization case was modeled using the large-displacement finite rotations model, and the hinged-clamped fixation set. Table 2.6 summarizes

this results.

Design variable	SQP	Active-set
b_1	5.2194 mm	6.4913 mm
h_1	5.1635 mm	6.5750 mm
H_1	52.0916 mm	53.2499 mm
b_2	5.0000 mm	5.3377 mm
h_2	5.0000 mm	5.2501 mm
H_2	101.8915 mm	81.9988 mm
b_h	5.0000 mm	5.1792 mm
h_h	5.0000 mm	6.5153 mm
α_1	1.5638 rad	1.6416 rad
α_2	1.6112 rad	1.6708 rad
θ_A	-0.3119 rad	-0.3061 rad
M_A	-4.4733$\times 10^5$ Nmm	-1.0998$\times 10^5$ Nmm
Volume	8.9512$\times 10^3$ mm^3	1.1319$\times 10^4$ mm^3

Table 2.6: Hinged-clamped 4-bar partially compliant mechanism. Cardona and Géradin's beam finite element model.
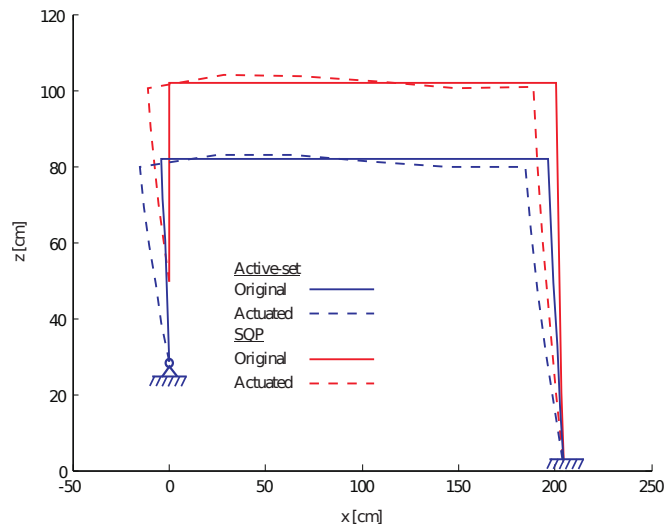
Figure 2.23: Hinged-clamped 4-bar mechanism. Cardona and Géradin's beam finite element model. Displacements are in the same scale than the dimensions of the mechanism.

The reduction of flexibility caused by the clamp yielded mechanisms with longer follower links compared to the hinged-hinged case, Figure 2.23. SQP

worked better with this large-displacement model, yielding a design that needs 21% less volume than the design of active-set for the same mechanism task, 8.9512×10^3 mm^3 vs. 1.1319×10^4 mm^3 respectively.

Both designs use much less material volume than Saggere and Kota [SK01] design, yiending a 65% volume save in the best result (SQP), and a 56% save in the worst result (active-set).

2.6 Conclusions

In this chapter, structural optimization methods (e.g. topology, size and shape) were described and tested in the context of mechanisms design. Results obtained with topology optimization methods are independent of prior design choices, being this perhaps the major advantage of this technique. However, algorithms used in topology optimization assume geometrically linear mechanical behavior, and inaccurate results may be obtained when applied to a compliant mechanisms that usually undergoes large displacement.

An application of shape and size optimization was performed on a turbine disc where the shape and size of its ventilation holes were optimized, and later on a four-bar compliant mechanism. Links were modeled with non-linear small and large-displacement FEM elements. Eight different alternatives were analyzed for the same mechanism task, with different optimization algorithms, boundary conditions and FEM models (large-displacement and small displacement). Results demonstrated the feasibility of the method, with less material needed to fulfill the same mechanisms task of a test problem from the literature.

Structural optimization techniques are general design methods, in which a multitude of possible designs are obtained without the need of any initial commitment or proposal. However, computational cost is still the main drawback of this technique.

Chapter 3

Inverse FEM of general 3D solids [FCJ08]

In this chapter a finite element model for the inverse design of solids with large displacements in the elastic range is introduced. The problem consists in determining the initial shape of the piece, such that it attains the designed shape under the effect of service loads. Although the formulation expresses equilibrium on the distorted configuration, it uses a standard constitutive equations library which is expressed as usual for measures attached to the undistorted configuration. In this way, the modifications to a standard finite elements code are limited to the routines for the computation of the finite element internal forces and tangent matrix.

3.1 Introduction

A central aspect when designing a piece to have an imposed shape after severe deformation, is to compute its undistorted shape. In this analysis, the final (desired) configuration is supposed to be that of the piece subjected to service loads once the steady state has been attained, neglecting any transient effect.

The classical (direct) problem in nonlinear elasticity consists in determining the distorted shape knowing the loads applied to the piece in a given reference configuration. The subject of this study is the inverse problem that consists

in determining the undistorted configuration knowing the final configuration and service loads. Strictly speaking, it is an inverse "design" problem [BW98], in contrast to classical inverse "measurement" problems (often called simply "inverse problems"), that consists in determining the material data knowing both the distorted and undistorted configurations as well as the service loads.

Some pieces (like turbine blades) that are designed to be cyclically used, must recover the original shape after each service cycle, constraining the material to lie within the elastic range all along the deformation process. Moreover, sometimes they are made of laminates with a markedly anisotropic behavior. We will use therefore an anisotropic hyperelastic material law limited to the small strains domain (however, large deformations can develop). In the isotropic case, some simplifications could be introduced that allow extending the formulation to finite hyperelasticity.

Previous numerical models for the inverse design analysis of hyperelastic bodies subjected to large deformations have been proposed by Govindjee and Mihalic [GM96, GM98] and Yamada [Yam97]. Both models use the finite element method in order to discretize the inverse deformation. They differ in the fact that Govindjee and Mihalic's model is Eulerian, and the equilibrium equation is formulated in terms of variables attached to the (known) distorted configuration, while Yamada's model is Arbitrary-Lagrangean-Eulerian (ALE), i.e., the problem is expressed on a reference configuration which is different from the undistorted and distorted ones.

In reference [GM98] not only the equilibrium equations but also the constitutive equations are written in terms of Eulerian variables, which complicates the description of orthotropic materials whose preferred directions are usually defined in the unknown undistorted configuration.

We made an effort in order to use the available material library from our nonlinear finite elements code [Sam07], in which constitutive equations are written in terms of Lagrangean variables (Piola-Kirchhoff stresses in terms of Green-Lagrange strains). In this form, the modifications made into the code to implement the model for inverse analysis are restricted to the routines for computing the residual vector and tangent matrix for the inverse finite element method, preserving the material library, what clearly simplified the develop-

ment. Another important contribution is the treatment of body forces, not included in previous works. In fact, in the problems addressed by the previous inverse design models [GM96, GM98, Yam97], the body forces were not relevant. However, this is not the case when modelling turbine blades, where centrifugal body forces are significant. External forces (including body and surface forces) usually depend on deformation, with the consequent contribution to the finite element tangent matrix.

An example application of the model is given. The simple case of bending of a laminated beam is considered, for which the determination of its distorted shape is an easy task for any available code for large deformation analysis. Once the distorted shape is known, we evaluate the ability of the present model to recover the initial shape.

3.2 Kinematic description

Let $\mathcal{B}_0$ be the undistorted reference configuration of a continuum body, and $\mathcal{B}$ the objective (final) configuration. The position $\boldsymbol{x} \in \mathcal{B}$ of any particle P with position $\boldsymbol{X} \in \mathcal{B}_0$ is determined by the deformation $\boldsymbol{x} = \boldsymbol{\phi}(\boldsymbol{X})$. The deformation gradient relative to the reference configuration is :

$$\boldsymbol{F} = \operatorname{Grad} \boldsymbol{\phi}, \tag{3.1}$$

where Grad denotes gradient with respect to $\boldsymbol{X} \in \mathcal{B}_0$.

In the problem we are interested in, we know the final configuration and we want to determine the inverse deformation $\boldsymbol{X} = \boldsymbol{\psi}(\boldsymbol{x})$ giving the position $\boldsymbol{X} \in \mathcal{B}_0$ of every particle whose final position is $\boldsymbol{x} \in \mathcal{B}$. The inverse deformation gradient is defined as

$$\boldsymbol{f} = \operatorname{grad} \boldsymbol{\psi} = \boldsymbol{F}^{-1}, \tag{3.2}$$

where grad denotes gradient with respect to $\boldsymbol{x} \in \mathcal{B}$.
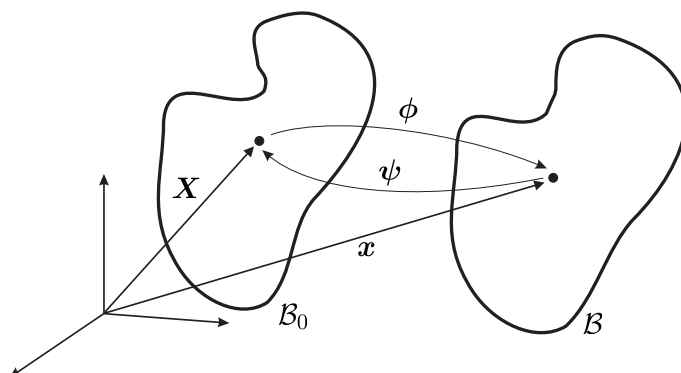
Figure 3.1: Distorted configuration $\mathcal{B}$, domain of inverse analysis, and undistorted configuration $\mathcal{B}_0$ sought as solution.

3.3   Material description

The constitutive law for a general hyperelastic material can be written as follows [Ogd84]

$$\boldsymbol{S} = \frac{\partial w}{\partial \boldsymbol{E}} = \boldsymbol{S}(\boldsymbol{E}), \tag{3.3}$$

where w is the strain-energy density function, $\boldsymbol{S}$ is the second Piola-Kirchhoff stress tensor, and $\boldsymbol{E}$ is the Green-Lagrange strain tensor defined as

$$\boldsymbol{E} = \frac{1}{2}\left(\boldsymbol{F}^T\boldsymbol{F} - \boldsymbol{1}\right), \tag{3.4}$$

$\boldsymbol{1}$ denoting the second-order identity tensor.

3.3.1   Anisotropy in inverse analysis

The constitutive equation (3.3) is formulated in terms of $\boldsymbol{S}$ and $\boldsymbol{E}$, that are Lagrangean tensors, i.e. tensors related to the reference configuration. Consequently, the material properties must be attached to this configuration which is unknown. This hinders the definition of preferred material directions, and hence the modelling of anisotropic materials.

In the case of laminated bodies for which strains remain small, it is possible to approximate the preferred directions of anisotropy in the distorted configuration by writing the constitutive equation (3.3) in Eulerian form by a simple

rotation of the material axes. We rotate the Green-Lagrange strain tensor and the second Piola-Kirchhoff stress tensor to the spatial axes as follows :

$$\boldsymbol{E}^* = \boldsymbol{R}\boldsymbol{E}\boldsymbol{R}^T = \frac{1}{2}\left(\boldsymbol{F}\boldsymbol{F}^T - \boldsymbol{1}\right) = \frac{1}{2}\left(\boldsymbol{V}^2 - \boldsymbol{1}\right), \tag{3.5}$$

$$\boldsymbol{S}^* = \boldsymbol{R}\boldsymbol{S}\boldsymbol{R}^T. \tag{3.6}$$

$\boldsymbol{V}$ is the symmetric positive-definite left-stretch tensor and $\boldsymbol{R}$ is the rotation tensor, both being computed from the polar decomposition of the deformation gradient :

$$\boldsymbol{F} = \boldsymbol{V}\boldsymbol{R}. \tag{3.7}$$

Now, the chain rule together with equation (3.5) yields

$$S_{ij} = \frac{\partial w}{\partial E_{ij}} = \frac{\partial w}{\partial E^*_{kl}}\frac{\partial E^*_{kl}}{\partial E_{ij}} = R_{ki}R_{lj}\frac{\partial w}{\partial E^*_{kl}}, \quad \text{or} \quad \boldsymbol{S} = \boldsymbol{R}^T\frac{\partial w}{\partial \boldsymbol{E}^*}\boldsymbol{R}, \tag{3.8}$$

from which we deduce the desired constitutive law in Eulerian form :

$$\boldsymbol{S}^* = \frac{\partial w}{\partial \boldsymbol{E}^*} = \boldsymbol{S}^*(\boldsymbol{E}^*). \tag{3.9}$$

In such a way, we are able to define the material properties with respect to a system of axes linked to the known distorted configuration.

3.4 Finite element formulation

The inverse design problem consists in finding the function $\boldsymbol{\psi}$ that satisfies the equilibrium equations, taken here in the weak form :

$$\int_{\mathcal{B}} \text{tr}\left[\boldsymbol{\sigma}^T \text{grad}\left(\boldsymbol{\eta}\right)\right] \mathrm{d}v - \int_{\mathcal{B}} \boldsymbol{b}\cdot\boldsymbol{\eta}\,\mathrm{d}v - \int_{\partial\mathcal{B}_t} \boldsymbol{t}\cdot\boldsymbol{\eta}\,\mathrm{d}s = \boldsymbol{0} \tag{3.10}$$

for every admissible variation $\boldsymbol{\eta}$, where $\boldsymbol{\sigma}$ is the Cauchy stress tensor, $\boldsymbol{b}$ is the given body force per unit distorted volume, $\boldsymbol{t}$ is the traction prescribed on the portion $\partial\mathcal{B}_t$ of the boundary $\partial\mathcal{B}$ of the distorted domain $\mathcal{B}$ (hence, $\boldsymbol{t}$ is a force per unit distorted area).

Using the finite element method, the position of particles in the undistorted

configuration is approximated inside a typical finite element Ω^e with nodes $1, 2, \ldots, N$ as follows

$$\boldsymbol{X} \approx \sum_{I=1}^{N} N_I(\boldsymbol{x})\boldsymbol{X}_I, \tag{3.11}$$

where $N_I(\boldsymbol{x})$ is the shape function associated to the node I, and $\boldsymbol{X}_I$ is the unknown position of this node in the undistorted configuration.

Introducing this approximation, and taking variations with respect to the positions in the undistorted configuration (standard Galerkin formulation), we get the discrete equation

$$\boldsymbol{R} = \boldsymbol{F}^{\text{int}} - \boldsymbol{F}^{\text{ext}} = \boldsymbol{0}, \tag{3.12}$$

where $\boldsymbol{F}^{\text{int}}$ and $\boldsymbol{F}^{\text{ext}}$ are respectively the internal and external force vectors, given by

$$\boldsymbol{F}^{\text{int}} = \int_{\mathcal{B}} \boldsymbol{b}^T \bar{\boldsymbol{\sigma}} \, \mathrm{d}v, \tag{3.13}$$

$$\boldsymbol{F}^{\text{ext}} = \int_{\mathcal{B}} \boldsymbol{N}^T \boldsymbol{b} \, \mathrm{d}v + \int_{\partial\mathcal{B}_t} \boldsymbol{N}^T \boldsymbol{t} \, \mathrm{d}s, \tag{3.14}$$

$\boldsymbol{b}$ being the gradients matrix, and $\bar{\boldsymbol{\sigma}}$ the vector containing the independent components of the symmetric Cauchy stress tensor $\boldsymbol{\sigma}$. [1]

In turbine blades modelling, the external forces mainly consist of the centrifugal and pressure forces. The former are represented by the first term of the r.h.s. of equation (3.14) with $\boldsymbol{b}$ defined as

$$\boldsymbol{b} = \rho\boldsymbol{a}^{\text{centr}}, \tag{3.15}$$

being ρ the density in the distorted configuration, and $\boldsymbol{a}^{\text{centr}}$ the centrifugal

---

[1] From now on, $\bar{\boldsymbol{t}}$ denotes the vector (matrix) containing the components of the second-order (respectively, fourth-order) tensor $\boldsymbol{t}$. A single rule for the mapping of tensors into vectors or matrices cannot be defined, since the mapping depends on the tensor symmetries involved in certain tensor products. For the sake of conciseness, the definition of the algorithmic versions of all tensors appearing in the text are given in the Appendix.

acceleration, defined as

$$\boldsymbol{a}^{\mathrm{centr}}(\boldsymbol{x}) = \boldsymbol{\omega} \times \left[\boldsymbol{\omega} \times (\boldsymbol{x} - \boldsymbol{o}) \right], \tag{3.16}$$

where $\boldsymbol{\omega}$ is the angular velocity vector and $\boldsymbol{o}$ the position of an arbitrary point on the rotation axis. On the other hand, the pressure force is represented by the second term of the r.h.s. of equation (3.14) by defining

$$\boldsymbol{t} = -p\boldsymbol{n} \tag{3.17}$$

where p is the pressure and $\boldsymbol{n}$ the outer normal to the portion $\partial \mathcal{B}_t$ of the surface of the body in the distorted configuration.

3.4.1 Computation of strains and stresses in finite elements

By using equation (5.1), the inverse deformation gradient is approximated in terms of derivatives of the interpolation functions as :

$$\boldsymbol{f} = \frac{\partial \boldsymbol{X}}{\partial \boldsymbol{x}} \approx \frac{\partial N_I}{\partial \boldsymbol{x}} \boldsymbol{X}_I. \tag{3.18}$$

Once $\boldsymbol{f}$ is known, we can compute the (direct) deformation gradient $\boldsymbol{F} = \boldsymbol{f}^{-1}$, and then the Green-Lagrange strain $\boldsymbol{E}$ using equation (3.4) as well as its rotated counterpart $\boldsymbol{E}^*$ given by equation (3.5).

Entering $\boldsymbol{E}^*$ in the constitutive law (3.9), we determine the rotated second Piola-Kirchhoff stress $\boldsymbol{S}^*$. Then, we are able to compute the Cauchy stress by means of the relationship

$$\boldsymbol{\sigma} = j\boldsymbol{F}\boldsymbol{S}\boldsymbol{F}^T = j\boldsymbol{V}\boldsymbol{S}^*\boldsymbol{V}^T,$$

or, given in Cartesian components :

$$\sigma_{kl} = jV_{km}S^*_{mn}V_{ln}, \tag{3.19}$$

where $j = \det \boldsymbol{f}$ is the Jacobian of the inverse deformation $\boldsymbol{X} = \boldsymbol{\psi}(\boldsymbol{x})$. In order to replace tensor products by matrix products as usual in the finite element practice, we introduce the tensor

$$I^V_{klmn} = \frac{1}{2} \left(V_{km} V_{ln} + V_{kn} V_{lm} \right) = I^V_{klnm} = I^V_{lkmn}, \tag{3.20}$$

which allows us to rewrite (3.19) as follows :

$$\sigma_{kl} = j I^V_{klmn} S^*_{mn}. \tag{3.21}$$

A tensor product like this can be taken to the following matrix expression :

$$\bar{\boldsymbol{\sigma}} = j \bar{\boldsymbol{I}}^V \bar{\boldsymbol{S}}^*. \tag{3.22}$$

3.4.2   Solution of the nonlinear equilibrium equation

The nonlinear equation (3.12) is solved iteratively using the Newton-Raphson method (see [ZT00] for details on the implementation of this method in the finite element context). At each iteration k we have to solve the following linear equation for the increment $\Delta \boldsymbol{q}$:

$$\boldsymbol{R}(\boldsymbol{q}^{k+1}) = \boldsymbol{R}(\boldsymbol{q}^k) + \boldsymbol{K}(\boldsymbol{q}^k)\Delta \boldsymbol{q}, \tag{3.23}$$

where $\boldsymbol{K}$ denotes the tangent matrix, given by :

$$\boldsymbol{K} = \frac{\partial \boldsymbol{R}}{\partial \boldsymbol{q}} = \frac{\partial \boldsymbol{F}^{\text{int}}}{\partial \boldsymbol{q}} + \frac{\partial \boldsymbol{F}^{\text{ext}}}{\partial \boldsymbol{q}} = \boldsymbol{K}^{\text{int}} + \boldsymbol{K}^{\text{ext}}. \tag{3.24}$$

and where $\boldsymbol{q}$ is the vector of unknown nodal parameters, which in this case are the positions $\boldsymbol{X}_I$ of nodes at the initial configuration.

Concerning external forces, we note that there is no contribution to the tangent matrix from the pressure forces in inverse analysis. In fact, contrary to what happens in direct analysis, the normal $\boldsymbol{n}$ to the external surface in the distorted configuration is known and fixed. On the other hand, there would be no contribution from the centrifugal force vector if ρ were known in the

distorted configuration. However, the value of the density we usually know is that related to the undistorted configuration, say ρ_0. Then, ρ is computed from the local mass balance equation

$$\rho = j\rho_0. \tag{3.25}$$

Nevertheless, since we remain within the domain of small strains, the density $\rho \approx \rho_0$ and the contribution of the centrifugal forces to the tangent matrix can be neglected.

Therefore, the tangent matrix reduces to the expression

$$\boldsymbol{K} \approx \boldsymbol{K}^{\text{int}} = \int_{\mathcal{B}} \boldsymbol{b}^T \frac{\partial \bar{\boldsymbol{\sigma}}}{\partial \boldsymbol{q}} \, \mathrm{d}v. \tag{3.26}$$

The computation of $\partial \bar{\boldsymbol{\sigma}} / \partial \boldsymbol{q}$ in an exact analytical way is described in the next section.

3.4.3 Computation of the stress derivatives

In a typical finite element, after computing the internal forces vector as described above, we know the inverse deformation gradient $\boldsymbol{f}$, the deformation gradient $\boldsymbol{F}$, the left-stretch tensor $\boldsymbol{V}$ and the fourth-order tensor $\boldsymbol{I}^V$ (which is a function of $\boldsymbol{V}$ squared), the rotated Green-Lagrange strain $\boldsymbol{E}^*$, the rotated Piola-Kirchhoff stress $\boldsymbol{S}^*$ and the Cauchy stress $\boldsymbol{\sigma}$. In order to compute the tangent stiffness matrix for inverse analysis, we need to compute the derivatives of the Cauchy stress with respect to the nodal parameters of the inverse motion. For this purpose, we will compute first the corresponding variations :

$$\Delta\bar{\boldsymbol{\sigma}} = \underbrace{j^{-1}\bar{\boldsymbol{\sigma}}\Delta j}_{\bar{\boldsymbol{\Delta}}^{(1)}} + \underbrace{j\bar{\boldsymbol{I}}^V \Delta\bar{\boldsymbol{S}}^*}_{\bar{\boldsymbol{\Delta}}^{(2)}} + \underbrace{j\Delta\bar{\boldsymbol{I}}^V \bar{\boldsymbol{S}}^*}_{\bar{\boldsymbol{\Delta}}^{(3)}}. \tag{3.27}$$

For clarity of presentation, the computation of each term $\bar{\boldsymbol{\Delta}}^{(i)}$ will be treated separately.

Computation of $\bar{\boldsymbol{\Delta}}^{(1)}$.

The differentiation rule for the determinant of a second order tensor yields

$$\Delta j = j \ \mathrm{tr}\,(\boldsymbol{F}^T \Delta \boldsymbol{f}) = j \ (\bar{\boldsymbol{F}^T})^T \Delta \bar{\boldsymbol{f}}. \tag{3.28}$$

Given $\boldsymbol{f}$ by equation (3.18), it is straightforward to compute its determinant j, its inverse $\boldsymbol{F}$ and its derivative

$$\Delta \boldsymbol{f} = \frac{\partial N_I}{\partial \boldsymbol{x}} \Delta \boldsymbol{X}_I, \quad \text{or} \quad \Delta \bar{\boldsymbol{f}} = \bar{\boldsymbol{N}}_{,x} \Delta \boldsymbol{q}. \tag{3.29}$$

Then, the first term in the r.h.s. of equation (3.27) can be expressed as

$$\bar{\boldsymbol{\Delta}}^{(1)} = \bar{\boldsymbol{\sigma}}(\bar{\boldsymbol{F}^T})^T \bar{\boldsymbol{N}}_{,x} \Delta \boldsymbol{q}. \tag{3.30}$$

Computation of $\bar{\boldsymbol{\Delta}}^{(2)}$.

First, we need to determine

$$\Delta \boldsymbol{S}^* = \frac{\partial \boldsymbol{S}^*}{\partial \boldsymbol{E}^*} \Delta \boldsymbol{E}^* = \boldsymbol{D}^* \Delta \boldsymbol{E}^*. \tag{3.31}$$

The components D^*_{mnkl} of the fourth-order tensor $\boldsymbol{D}^*$ of tangent moduli, together with the rotated second Piola-Kirchhoff stress tensor $\boldsymbol{S}^*$, are computed in the constitutive-equation software module as a function of the rotated Green-Lagrange strain $\boldsymbol{E}^*$. The tensor $\boldsymbol{D}^*$ verifies the following symmetries :

$$D^*_{mnkl} = D^*_{nmkl} = D^*_{mnlk}. \tag{3.32}$$

On the other hand, the variation of $\boldsymbol{E}^*$ results :

$$\Delta E^*_{ij} = \frac{1}{2} \Delta (F_{ik} F_{jk}) = \Theta_{ijkl} \Delta F_{kl}, \quad \text{or} \quad \Delta \bar{\boldsymbol{E}}^* = \bar{\boldsymbol{\Theta}} \Delta \bar{\boldsymbol{F}}, \tag{3.33}$$

with the components of the fourth-order tensor $\boldsymbol{\Theta}$ given by :

$$\Theta_{ijkl} = \frac{1}{2} \left(\delta_{ik} F_{jl} + \delta_{jk} F_{il} \right), \tag{3.34}$$

δ_{ij} denoting the Kronecker delta.

Using the rule of differentiation of the inverse of a second order tensor, we obtain :

$$\Delta F_{km} = -\Lambda_{kmpq}\Delta f_{pq}, \quad \text{or} \quad \Delta\bar{\boldsymbol{F}} = -\bar{\boldsymbol{\Lambda}}\Delta\bar{\boldsymbol{f}}, \tag{3.35}$$

with

$$\Lambda_{kmpq} = F_{kp}F_{qm}. \tag{3.36}$$

Then, the second term in the r.h.s. of equation (3.27) can be expressed as

$$\bar{\boldsymbol{\Delta}}^{(2)} = -j\bar{\boldsymbol{I}}^V\bar{\boldsymbol{D}}^*\bar{\boldsymbol{\Theta}}\bar{\boldsymbol{\Lambda}}\bar{\boldsymbol{N}}_{,x}\Delta\boldsymbol{q}. \tag{3.37}$$

Computation of $\bar{\boldsymbol{\Delta}}^{(3)}$.

First, let us rewrite the third term of the r.h.s. of equation (3.27) as follows :

$$\Delta_{kl}^{(3)} = j\Delta I_{klmn}^V S_{mn}^* = j\Upsilon_{klpq}\Delta V_{pq}, \quad \text{or} \quad \bar{\boldsymbol{\Delta}}^{(3)} = j\,\bar{\boldsymbol{\Upsilon}}\Delta\bar{\boldsymbol{V}}, \tag{3.38}$$

where

$$\Upsilon_{klpq} = \left(I_{kmpq}V_{ln} + I_{lmpq}V_{kn}\right)S_{mn}^* = \boldsymbol{\Upsilon}_{lkpq} = \Upsilon_{klqp}. \tag{3.39}$$

Here, $I_{ijkl} = (\delta_{ik}\delta_{jl} + \delta_{il}\delta_{jl})/2$ is the fourth-order identity tensor.

Now, the only missing term to be computed is $\Delta\boldsymbol{V}$. To this end, we begin by computing $\Delta\boldsymbol{V}^2$:

$$\Delta(V_{ik}V_{kj}) = \Delta V_{ik}V_{kj} + V_{ik}\Delta V_{kj} = \Phi_{ijkm}\Delta V_{km}, \quad \text{or} \quad \Delta\bar{\boldsymbol{V}}^2 = \bar{\boldsymbol{\phi}}\Delta\bar{\boldsymbol{V}}, \tag{3.40}$$

where

$$\Phi_{ijkm} = I_{ijkl}V_{lm} + I_{ijml}V_{lk} = \Phi_{ijmk} = \Phi_{jikm}. \tag{3.41}$$

On the other hand, since $\boldsymbol{V}^2 = 2\boldsymbol{E}^* - \boldsymbol{1}$, its variation can also be computed as

$$\Delta\bar{\boldsymbol{V}}^2 = 2\Delta\bar{\boldsymbol{E}}^* = -2\bar{\boldsymbol{\Theta}}\bar{\boldsymbol{\Lambda}}\bar{\boldsymbol{N}}_{,x}\Delta\boldsymbol{q}. \tag{3.42}$$

By making equation (3.40) the same as equation (3.42), we obtain

$$\Delta\bar{\boldsymbol{V}} = -2\bar{\boldsymbol{\phi}}^{-1}\bar{\boldsymbol{\Theta}}\bar{\boldsymbol{\Lambda}}\bar{\boldsymbol{N}}_{,x}\Delta\boldsymbol{q}. \tag{3.43}$$

Finally, after replacing the last equation into equation (3.38), the third term of the r.h.s. of equation (3.27) can be expressed :

$$\bar{\boldsymbol{\Delta}}^{(3)} = -2j\bar{\boldsymbol{\Upsilon}}\bar{\boldsymbol{\phi}}^{-1}\bar{\boldsymbol{\Theta}}\bar{\boldsymbol{\Lambda}}\bar{\boldsymbol{N}}_{,x}\Delta\boldsymbol{q}. \tag{3.44}$$

Final form of $\partial\bar{\boldsymbol{\sigma}}/\partial\boldsymbol{q}$

The form given to the terms $\bar{\boldsymbol{\Delta}}^{(i)}$ of the variation of $\bar{\boldsymbol{\sigma}}$ allows the immediate determination of the derivative of $\bar{\boldsymbol{\sigma}}$ with respect to the nodal unknowns $\boldsymbol{q}$:

$$\frac{\partial\bar{\boldsymbol{\sigma}}}{\partial\boldsymbol{q}} = \bar{\boldsymbol{\sigma}}(\bar{\boldsymbol{F}}^T)^T\bar{\boldsymbol{N}}_{,x} - j\bar{\boldsymbol{I}}^V\bar{\boldsymbol{D}}^*\bar{\boldsymbol{\Theta}}\bar{\boldsymbol{\Lambda}}\bar{\boldsymbol{N}}_{,x} - 2j\bar{\boldsymbol{\Upsilon}}\bar{\boldsymbol{\phi}}^{-1}\bar{\boldsymbol{\Theta}}\bar{\boldsymbol{\Lambda}}\bar{\boldsymbol{N}}_{,x}. \tag{3.45}$$

Therefore, the tangent stiffness matrix results

$$\boldsymbol{K} = \int_{\mathcal{B}}\boldsymbol{b}^T\left[\bar{\boldsymbol{\sigma}}(\bar{\boldsymbol{F}}^T)^T - j\bar{\boldsymbol{I}}^V\bar{\boldsymbol{D}}^*\bar{\boldsymbol{\Theta}}\bar{\boldsymbol{\Lambda}} - 2j\bar{\boldsymbol{\Upsilon}}\bar{\boldsymbol{\phi}}^{-1}\bar{\boldsymbol{\Theta}}\bar{\boldsymbol{\Lambda}}\right]\bar{\boldsymbol{N}}_{,x}\,\mathrm{d}v. \tag{3.46}$$

Note that $\boldsymbol{K}$ is non-symmetric, as it was already the case in references [GM96, GM98].

Although not detailed here, the formulation can be easily extended to account also for thermal loads.

Remark.   In this work, the use of a constitutive law of the type $\boldsymbol{S}^* = \boldsymbol{S}^*(\boldsymbol{E}^*)$ makes the linearization of stress with respect to material coordinates somehow different to what can be found in preceding works in inverse analysis, where different constitutive laws were used.

For instance, in the work of Govindjee and Mihalic [GM96] they used a neo-Hookean isotropic material model defined by

$$\sigma_{kl} = j\mu(c_{kl}^{-1} - \delta_{kl}) - \lambda j \ln j \delta_{kl}, \tag{3.47}$$

where $\boldsymbol{c} = \boldsymbol{f}^T \boldsymbol{f}$, and λ and μ are material parameters that reduce to the Lamé constants in the case of small strains. Then, they obtain

$$D_{klmn}^{\sigma} = \frac{\partial \sigma_{kl}}{\partial c_{mn}} = \frac{1}{2}j\left\{\mu\left(c_{kl}^{-1}c_{mn}^{-1} - c_{km}^{-1}c_{ln}^{-1} - c_{kn}^{-1}c_{lm}^{-1}\right) - \left[\mu + \lambda\left(1 - \ln j\right)\right]\delta_{kl}c_{mn}^{-1}\right\} \tag{3.48}$$

The variation of $\boldsymbol{\sigma}$ is completely determined after computing

$$\Delta c_{mn} = 2\theta_{mnkl}\Delta f_{kl}, \quad \text{or} \quad \Delta$$

Therefore, using a constitutive equation of the type $\boldsymbol{\sigma} = \boldsymbol{\sigma}(\boldsymbol{c})$ like equation (3.47), the derivative of $\boldsymbol{\sigma}$ with respect to the material coordinates takes the algorithmic form

$$\frac{\partial\bar{\boldsymbol{\sigma}}}{\partial\boldsymbol{q}} = 2\bar{\boldsymbol{D}}^{\sigma}\bar{\boldsymbol{\theta}}\bar{\boldsymbol{N}}_{,x}, \tag{3.50}$$

which is much simpler than that of equation (3.45) used in this work. Unfortunately, we cannot define a law $\boldsymbol{\sigma} = \boldsymbol{\sigma}(\boldsymbol{c})$ in the case of anisotropic behavior [TN65].

Note finally that linearization of stresses with respect to material coordinates have been used in other contexts by several authors, for instance in the work of Thoutireddy and Ortiz [Tho03, TO04] on shape optimization and mesh adaptivity. They use constitutive laws of the form

$$\boldsymbol{P} = \frac{\partial w}{\partial\boldsymbol{F}}, \tag{3.51}$$

where $\boldsymbol{P}$ is the first Piola-Kirchhoff stress tensor, from which they derive the moduli $D_{ijkl}^{P} = \partial P_{ij}/\partial F_{kl}$. Then, the variation of $\boldsymbol{\sigma} = j\boldsymbol{P}\boldsymbol{F}^T$ takes the form

$$\Delta\sigma_{kl} = \frac{1}{j}\sigma_{kl}\Delta j + jD_{kmpq}^{P}\Delta F_{pq}F_{lm} + jP_{km}\Delta F_{lm}. \tag{3.52}$$

This linearization is also somehow simpler than the linearization defined by equation (3.45). Let us remark that the law (3.51) may be used for anisotropic materials and is not restricted to isotropy, hence it could have been used in the present formulation for inverse design problems, after applying a similar technique of rotation of axes to be able to define material properties in a system of axes linked to the distorted (known) configuration. Nevertheless, in our case a law of the type $\boldsymbol{S}^* = \boldsymbol{S}^*(\boldsymbol{E}^*)$ was necessary with the objective of reutilization of the available material software module.

3.5 Application

3.5.1 Validation test

Let us consider the simple problem of bending a beam under plane strain conditions. First, we solve the direct problem, i.e., given the undistorted configuration $\mathcal{B}_0$ as well as the kinematic boundary conditions and the applied forces, we determine the distorted configuration $\mathcal{B}$. The problem is schematized in Figure 3.2. The domain is discretized using trilinear hexahedral finite elements. Even if it is essentially a 2D problem, 3D elements are used for generality. In order to represent a plane strain state, a one-element-wide mesh is used, and the faces normal to the $\boldsymbol{k}$-axis are constrained to move in their planes.

Table 3.1: Material data for the beam bending problem.

$E_1 = 500\,\mathrm{N/cm}^2$	$\nu_{12} = 0.3$	$G_{12} = 192.31\,\mathrm{N/cm}^2$
$E_2 = 1000\,\mathrm{N/cm}^2$	$\nu_{23} = 0.2$	$G_{23} = 312.50\,\mathrm{N/cm}^2$
$E_3 = 750\,\mathrm{N/cm}^2$	$\nu_{13} = 0.25$	$G_{13} = 288.46\,\mathrm{N/cm}^2$

The bar is made of horizontal laminates with fibers disposed in the $\boldsymbol{i}$-direction. The material has an orthotropic behavior, characterized by the Young moduli E_1, E_2, E_3, Poisson ratii ν_{12}, ν_{23}, ν_{13}, and shear ratii G_{12}, G_{23}, G_{13} with respect to the orthotropy orthogonal axes $\{\boldsymbol{u}^{(1)}, \boldsymbol{u}^{(2)}, \boldsymbol{u}^{(3)}\}$. Table
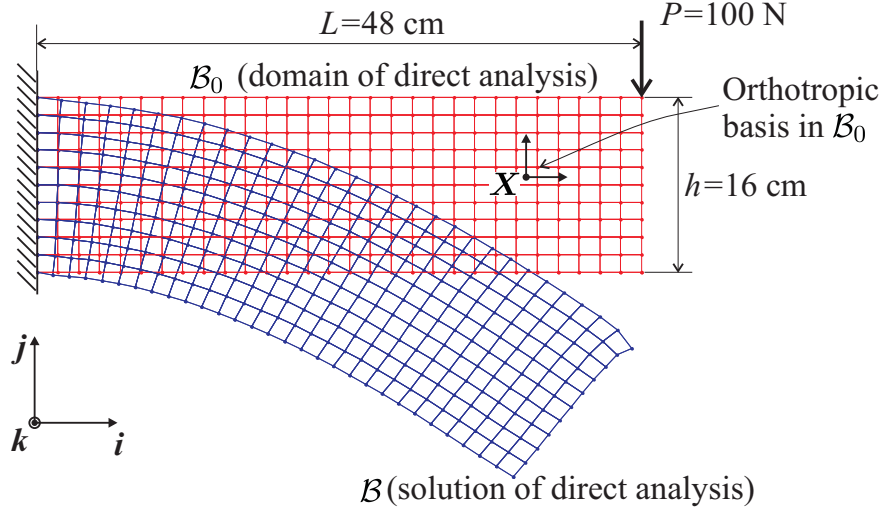
Figure 3.2: Direct problem.

3.1 lists the values we assumed for these properties. Further, we adopt the hyperelastic constitutive law :

$$\bar{\boldsymbol{S}} = \bar{\boldsymbol{D}}\bar{\boldsymbol{E}}, \tag{3.53}$$

where

$$\bar{\boldsymbol{D}} = \begin{bmatrix} \frac{1-\nu_{23}\nu_{32}}{\alpha E_2 E_3} & \frac{\nu_{12}+\nu_{32}\nu_{13}}{\alpha E_1 E_3} & \frac{\nu_{13}+\nu_{12}\nu_{23}}{\alpha E_1 E_2} & 0 & 0 & 0 \\ & \frac{1-\nu_{13}\nu_{31}}{\alpha E_3 E_3} & \frac{\nu_{23}+\nu_{21}\nu_{13}}{\alpha E_1 E_2} & 0 & 0 & 0 \\ & & \frac{1-\nu_{12}\nu_{21}}{\alpha E_1 E_2} & 0 & 0 & 0 \\ & & & G_{12} & 0 & 0 \\ & \text{symmetric} & & & G_{23} & 0 \\ & & & & & G_{13} \end{bmatrix}, \tag{3.54}$$

with

$$\nu_{21} = \frac{E_2}{E_1}\nu_{12}, \qquad \nu_{31} = \frac{E_3}{E_1}\nu_{13}, \qquad \nu_{32} = \frac{E_3}{E_2}\nu_{23},$$

$$\alpha = \frac{1 - \nu_{12}\nu_{21} - \nu_{23}\nu_{32} - \nu_{13}\nu_{31} - 2\nu_{12}\nu_{32}\nu_{13}}{E_1 E_2 E_3}. \tag{3.55}$$

Here, the orthotropy axes $\{\boldsymbol{u}^{(1)}, \boldsymbol{u}^{(2)}, \boldsymbol{u}^{(3)}\}$ coincide with the Lagrangean princi-
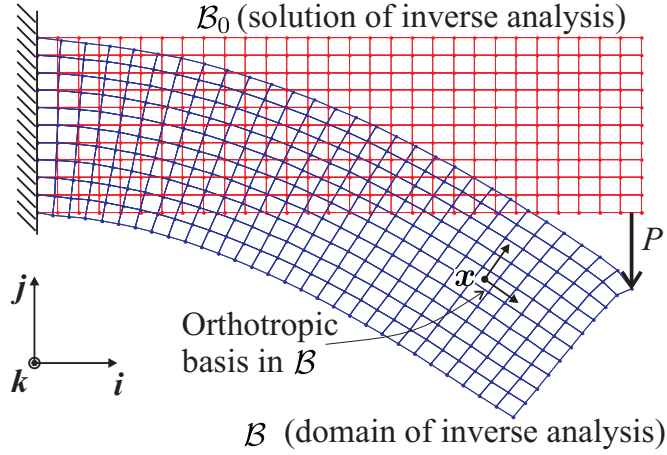
Figure 3.3: Inverse problem.

pal axes, which are also coincident with the Cartesian coordinate basis $\{i, j, k\}$.

The domain of the inverse design analysis is the distorted configuration $\mathcal{B}$ computed as solution of the direct analysis and shown in Figure 3.2. The inverse problem is schematized in Figure 3.3. The objective of the computation is to verify if we are able to recover the original undistorted configuration as solution.

The orthotropy axes coincide now with the Eulerian principal axes $v^{(i)} = Ru^{(i)}$, where R is the rotational part of the deformation gradient F and varies throughout the domain. Although in this case these axes can be exactly determined from the previous direct analysis, in practice they will be given for the distorted geometry taking into account the laminated nature of the body and the desired fiber orientations when under loading.

Figure 3.4 shows a plot of the inverse solution, displaying a map of the magnitude of the displacements $u = x - \psi(x)$.

We define an error measure of the inverse model computation, as a distance between the nodes of the mesh used for the direct analysis and the positions obtained as solution of the inverse analysis. After solving the equilibrium equation (3.12) with a very small residue norm $\|R\| < 1.6 \times 10^{-11}$ (the L_2-norm of the residue vector R), we obtained a maximum error of $26.6\,\mu$m at the nodes where the concentrated forces were applied. The relative error with respect to the displacements magnitude is less than 0.01%, which demonstrates
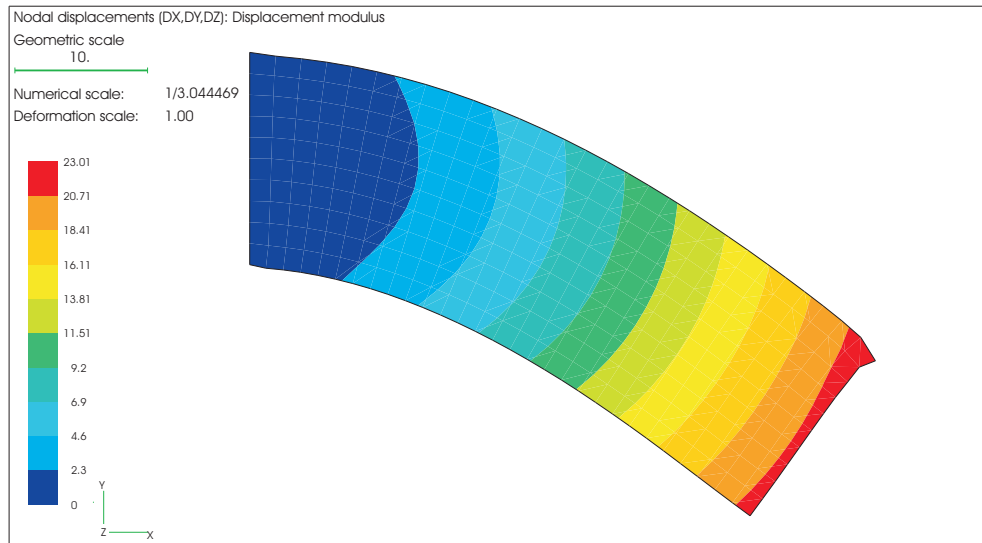
Figure 3.4: Displacement modulus from the inverse analysis.
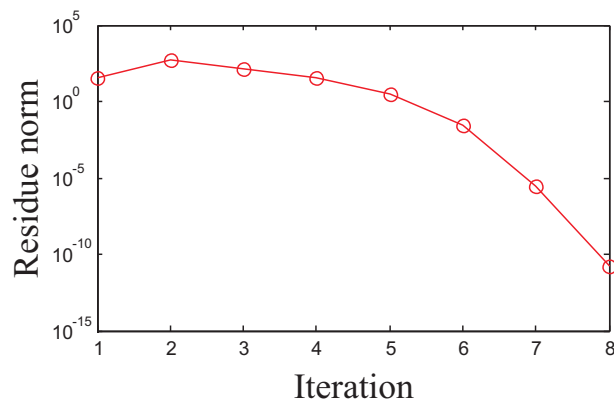
Figure 3.5: Evolution of the residue norm during the inverse analysis.

the excellent accuracy of the inverse model.

Figure 3.5 shows the evolution of $\|\boldsymbol{R}\|$ as a function of iterations. We note that after the 5th iteration, when the trial solution entered into the convergence radius of the solution, an optimal (quadratic) convergence rate is observed.

Appendix: Algorithmic form of tensors

A symmetric stress tensor, e.g. $\boldsymbol{\sigma}$, is mapped in a vector according to the rule:

$$\bar{\boldsymbol{\sigma}} = \bar{\boldsymbol{v}}^\sigma(\boldsymbol{\sigma}) = [\sigma_{11}\ \sigma_{22}\ \sigma_{33}\ \sigma_{12}\ \sigma_{23}\ \sigma_{31}]^T.$$

Accordingly, $\bar{\boldsymbol{S}} = \bar{\boldsymbol{v}}^\sigma(\boldsymbol{S})$, $\bar{\boldsymbol{S}}^* = \bar{\boldsymbol{v}}^\sigma(\boldsymbol{S}^*)$, $\bar{\Delta}^{(i)} = \bar{\boldsymbol{v}}^\sigma(\Delta^{(i)})$.

For a symmetric strain tensor, say $\boldsymbol{E}$, the following rule holds

$$\bar{\boldsymbol{E}} = \bar{\boldsymbol{v}}^\varepsilon(\boldsymbol{E}) = [E_{11}\ E_{22}\ E_{33}\ 2E_{12}\ 2E_{23}\ 2E_{31}]^T,$$

and so as $\bar{\boldsymbol{E}}^* = \bar{\boldsymbol{v}}^\varepsilon(\boldsymbol{E}^*)$, $\bar{\boldsymbol{c}} = \bar{\boldsymbol{v}}^\varepsilon(\boldsymbol{c})$ and $\bar{\boldsymbol{V}}^2 = \bar{\boldsymbol{v}}^\varepsilon(\boldsymbol{V}^2)$. This convention is adopted also for the left-stretch tensor $\boldsymbol{V}$, which transforms to $\bar{\boldsymbol{V}} = \bar{\boldsymbol{v}}^\varepsilon(\boldsymbol{V})$.

For non-symmetric second-order tensors like $\boldsymbol{f}$, having nine independent components, we apply the transformation

$$\bar{\boldsymbol{f}} = \bar{\boldsymbol{v}}^f(\boldsymbol{f}) = [f_{11}\ f_{21}\ f_{31}\ f_{12}\ f_{22}\ f_{32}\ f_{13}\ f_{23}\ f_{33}]^T,$$

so $\bar{\boldsymbol{F}}^T = \boldsymbol{v}^f(\boldsymbol{F}^T)$, $\boldsymbol{E}^*$ and $\boldsymbol{c}$ This is also the case for the symmetric strain-like tensor $\boldsymbol{c}$.

Fourth-order tensors $\boldsymbol{t}$ having the symmetries $T_{ijkl} = T_{jikl} = T_{ijlk}$ are mapped into matrices whose general expression is

$$\bar{\boldsymbol{t}} = \bar{\boldsymbol{M}}^s(\boldsymbol{t}, \alpha, \beta) = \begin{bmatrix} T_{1111} & T_{1122} & T_{1133} & \alpha T_{1112} & \alpha T_{1123} & \alpha T_{1131} \\ T_{2211} & T_{2222} & T_{2233} & \alpha T_{2212} & \alpha T_{2223} & \alpha T_{2231} \\ T_{3311} & T_{3322} & T_{3333} & \alpha T_{3312} & \alpha T_{3323} & \alpha T_{3331} \\ \beta T_{1211} & \beta T_{1222} & \beta T_{1233} & \alpha\beta T_{1212} & \alpha\beta T_{1223} & \alpha\beta T_{1231} \\ \beta T_{2311} & \beta T_{2322} & \beta T_{2333} & \alpha\beta T_{2312} & \alpha\beta T_{2323} & \alpha\beta T_{2331} \\ \beta T_{3111} & \beta T_{3122} & \beta T_{3133} & \alpha\beta T_{3112} & \alpha\beta T_{3123} & \alpha\beta T_{3131} \end{bmatrix} \tag{3.56}$$

where the coefficients α and β depend on the nature of the second-order tensors involved in the tensor product we aim to replace by a simpler matrix product. For tensors like $\boldsymbol{D}$, $\boldsymbol{D}^*$, $\boldsymbol{D}^\sigma$ and $\boldsymbol{\Upsilon}$ that are multiplied by a symmetric strain tensor to obtain a symmetric stress tensor, we have $\alpha = \beta = 1$. On the other hand, the tensor $\boldsymbol{I}^V$ relating two symmetric stress tensors in equation (3.38), is

mapped into the matrix $\bar{\boldsymbol{I}}^V = \bar{\boldsymbol{M}}^s(\boldsymbol{I}^V, 2, 1)$. It is the same case for $\boldsymbol{\phi}$ relating $\Delta \boldsymbol{V}^2$ and $\Delta \boldsymbol{V}$ in equation (3.40), which maps into $\bar{\boldsymbol{\phi}} = \bar{\boldsymbol{M}}^s(\boldsymbol{\phi}, 2, 1)$.

Special mappings are needed for fourth-order tensors without such symmetries. For tensor $\boldsymbol{\Theta}$ relating the symmetric strain tensor $\Delta \boldsymbol{E}^*$ and the non-symmetric tensor $\Delta \boldsymbol{F}$ in equation (3.33), we have :

$$
\bar{\boldsymbol{\Theta}} = \begin{bmatrix}
\Theta_{1111} & \Theta_{1121} & \Theta_{1131} & \Theta_{1112} & \Theta_{1122} & \Theta_{1132} & \Theta_{1113} & \Theta_{1123} & \Theta_{1133} \\
\Theta_{2211} & \Theta_{2221} & \Theta_{2231} & \Theta_{2212} & \Theta_{2222} & \Theta_{2232} & \Theta_{2213} & \Theta_{2223} & \Theta_{2233} \\
\Theta_{3311} & \Theta_{3321} & \Theta_{3331} & \Theta_{3312} & \Theta_{3322} & \Theta_{3332} & \Theta_{3313} & \Theta_{3323} & \Theta_{3333} \\
2\Theta_{1211} & 2\Theta_{1221} & 2\Theta_{1231} & 2\Theta_{1212} & 2\Theta_{1222} & 2\Theta_{1232} & 2\Theta_{1213} & 2\Theta_{1223} & 2\Theta_{1233} \\
2\Theta_{2311} & 2\Theta_{2321} & 2\Theta_{2331} & 2\Theta_{2312} & 2\Theta_{2322} & 2\Theta_{2332} & 2\Theta_{2313} & 2\Theta_{2323} & 2\Theta_{2333} \\
2\Theta_{3111} & 2\Theta_{3121} & 2\Theta_{3131} & 2\Theta_{3112} & 2\Theta_{3122} & 2\Theta_{3132} & 2\Theta_{3113} & 2\Theta_{3123} & 2\Theta_{3133}
\end{bmatrix}
\tag{3.57}
$$

The same transformation applies to $\boldsymbol{\theta}$ in equation (**??**).

The tensor $\boldsymbol{\Lambda}$ relating non-symmetric tensors $\Delta \boldsymbol{F}$ and $\Delta \boldsymbol{f}$ in equation (3.35) maps into the matrix

$$
\bar{\boldsymbol{\Lambda}} = \begin{bmatrix}
\Lambda_{1111} & \Lambda_{1121} & \Lambda_{1131} & \Lambda_{1112} & \Lambda_{1122} & \Lambda_{1132} & \Lambda_{1113} & \Lambda_{1123} & \Lambda_{1133} \\
\Lambda_{2111} & \Lambda_{2121} & \Lambda_{2131} & \Lambda_{2112} & \Lambda_{2122} & \Lambda_{2132} & \Lambda_{2113} & \Lambda_{2123} & \Lambda_{2133} \\
\Lambda_{3111} & \Lambda_{3121} & \Lambda_{3131} & \Lambda_{3112} & \Lambda_{3122} & \Lambda_{3132} & \Lambda_{3113} & \Lambda_{3123} & \Lambda_{3133} \\
\Lambda_{1211} & \Lambda_{1221} & \Lambda_{1231} & \Lambda_{1212} & \Lambda_{1222} & \Lambda_{1232} & \Lambda_{1213} & \Lambda_{1223} & \Lambda_{1233} \\
\Lambda_{2211} & \Lambda_{2221} & \Lambda_{2231} & \Lambda_{2212} & \Lambda_{2222} & \Lambda_{2232} & \Lambda_{2213} & \Lambda_{2223} & \Lambda_{2233} \\
\Lambda_{3211} & \Lambda_{3221} & \Lambda_{3231} & \Lambda_{3212} & \Lambda_{3222} & \Lambda_{3232} & \Lambda_{3213} & \Lambda_{3223} & \Lambda_{3233} \\
\Lambda_{1311} & \Lambda_{1321} & \Lambda_{1331} & \Lambda_{1312} & \Lambda_{1322} & \Lambda_{1332} & \Lambda_{1313} & \Lambda_{1323} & \Lambda_{1333} \\
\Lambda_{2311} & \Lambda_{2321} & \Lambda_{2331} & \Lambda_{2312} & \Lambda_{2322} & \Lambda_{2332} & \Lambda_{2313} & \Lambda_{2323} & \Lambda_{2333} \\
\Lambda_{3311} & \Lambda_{3321} & \Lambda_{3331} & \Lambda_{3312} & \Lambda_{3322} & \Lambda_{3332} & \Lambda_{3313} & \Lambda_{3323} & \Lambda_{3333}
\end{bmatrix}
\tag{3.58}
$$

Finally, $\bar{\boldsymbol{N}}_{,x}$ is the matrix reordering the derivatives of the shape functions

in the following way :

$$
\bar{\boldsymbol{N}}_{,x} =
\begin{bmatrix}
\frac{\partial N_1}{\partial x} & 0 & 0 & \frac{\partial N_2}{\partial x} & 0 & 0 & \cdots \\
0 & \frac{\partial N_1}{\partial x} & 0 & 0 & \frac{\partial N_2}{\partial x} & 0 & \cdots \\
0 & 0 & \frac{\partial N_1}{\partial x} & 0 & 0 & \frac{\partial N_2}{\partial x} & \cdots \\
\frac{\partial N_1}{\partial y} & 0 & 0 & \frac{\partial N_2}{\partial y} & 0 & 0 & \cdots \\
0 & \frac{\partial N_1}{\partial y} & 0 & 0 & \frac{\partial N_2}{\partial y} & 0 & \cdots \\
0 & 0 & \frac{\partial N_1}{\partial y} & 0 & 0 & \frac{\partial N_2}{\partial y} & \cdots \\
\frac{\partial N_1}{\partial z} & 0 & 0 & \frac{\partial N_2}{\partial z} & 0 & 0 & \cdots \\
0 & \frac{\partial N_1}{\partial z} & 0 & 0 & \frac{\partial N_2}{\partial z} & 0 & \cdots \\
0 & 0 & \frac{\partial N_1}{\partial z} & 0 & 0 & \frac{\partial N_2}{\partial z} & \cdots
\end{bmatrix}.
\tag{3.59}
$$

Plane stress and plane strain problems

Under plane strain conditions, with strains $E_{ij} = E_{ji}$ restricted to the plane containing the vectors $\boldsymbol{u}^{(1)}$ and $\boldsymbol{u}^{(2)}$ of the orthotropic basis $\{\boldsymbol{u}^{(1)}, \boldsymbol{u}^{(2)}, \boldsymbol{u}^{(3)}\}$, i.e. $E_{13} = E_{23} = E_{33} = 0$, the orthotropic hyperelastic constitutive law (??) is valid whenever the vector counterparts of $\boldsymbol{S}$ and $\boldsymbol{E}$ as well as the matrix counterpart of the elastic moduli $\boldsymbol{D}$ be expressed as

$$
\bar{\boldsymbol{S}} = [S_{11}\ S_{22}\ S_{12}]^T, \qquad \bar{\boldsymbol{E}} = [E_{11}\ E_{22}\ 2E_{12}]^T,
$$

$$
\bar{\boldsymbol{D}} =
\begin{bmatrix}
\frac{1-\nu_{23}\nu_{32}}{\alpha E_2 E_3} & \frac{\nu_{12}+\nu_{32}\nu_{13}}{\alpha E_1 E_3} & 0 \\
 & \frac{1-\nu_{13}\nu_{31}}{\alpha E_1 E_3} & 0 \\
\text{symmetric} & & G_{12}
\end{bmatrix}
$$

where E_1, E_2, and E_3 are the Young moduli, ν_{12}, ν_{23}, and ν_{13} the Poisson ratii with respect to the orthotropy orthogonal axes $\{\boldsymbol{u}^{(1)}, \boldsymbol{u}^{(2)}, \boldsymbol{u}^{(3)}\}$, G_{12} is shear modulus in the plane containing the axes $\boldsymbol{u}^{(1)}$ and $\boldsymbol{u}^{(2)}$, and ν_{31}, ν_{32} and α are given by equation (??) and (??). In this case, the out-of-plane stresses are:

$$
S_{13} = S_{23} = 0, \qquad S_{33} = \frac{\nu_{13} + \nu_{12}\nu_{23}}{\alpha E_1 E_2} E_{11} + \frac{\nu_{23} + \nu_{21}\nu_{13}}{\alpha E_1 E_2} E_{22}.
\tag{3.60}
$$

Under plane stress conditions, with stresses $S_{ij} = S_{ji}$ restricted to the plane containing the vectors $\boldsymbol{u}^{(1)}$ and $\boldsymbol{u}^{(2)}$ of the orthotropic basis $\{\boldsymbol{u}^{(1)}, \boldsymbol{u}^{(2)}, \boldsymbol{u}^{(3)}\}$, i.e. $S_{13} = S_{23} = S_{33} = 0$, the orthotropic hyperelastic constitutive law (**??**) is valid whenever the vector counterparts of $\boldsymbol{S}$ and $\boldsymbol{E}$ were expressed as above, and the matrix counterpart of the elastic moduli $\boldsymbol{D}$ be expressed as

$$\bar{\boldsymbol{D}} = \frac{E_1}{E_1 - E_2 \nu_{12}^2} \begin{bmatrix} E_1 & \nu_{12} E_2 & 0 \\ & E_2 & 0 \\ \text{symmetric} & & \frac{G_{12}}{E_1}(E_1 - E_2 \nu_{12}^2) \end{bmatrix} \tag{3.61}$$

where E_1, E_2, ν_{12} and G_{12} are those material properties already defined for plane strain conditions. In this case, the out-of-plane strains are:

$$E_{13} = E_{23} = 0, \quad E_{33} = -\frac{\nu_{13}}{E_1} S_{11} - \frac{\nu_{23}}{E_2} S_{22}. \tag{3.62}$$

Stratified or transversely isotropic material

Now, let us consider a stratified or transversely isotropic material that exhibits a rotational symmetry of mechanical properties within the plane of the strate, say the xy-plane. Under plane strain or plane stress conditions, the orthotropic hyperelastic constitutive law (**??**) is valid whenever the vector counterparts of $\boldsymbol{S}$ and $\boldsymbol{E}$ as well as the matrix counterpart of the elastic moduli $\boldsymbol{D}$ be expressed as [ZT00]

$$\bar{\boldsymbol{S}} = [S_{xx} \ S_{yy} \ S_{xy}]^T, \quad \bar{\boldsymbol{E}} = [E_{xx} \ E_{yy} \ 2E_{xy}]^T \tag{3.63}$$

$$\bar{\boldsymbol{D}} = \frac{E_3}{(1 + \nu_1)\left(1 - \nu_1 - 2\frac{E_1}{E_3}\nu_3^2\right)} \times$$
$$\begin{bmatrix} \frac{E_1}{E_3}(1 - \nu_3^2) & \frac{E_1}{E_3}\nu_3(1 - \nu_1) & 0 \\ \frac{E_1}{E_3}\nu_3(1 - \nu_1) & \frac{E_1}{E_3}(1 - \nu_3^2) & 0 \\ 0 & 0 & \frac{G_3}{E_3}\left(1 - \nu_1 - 2\frac{E_1}{E_3}\nu_3^2\right) \end{bmatrix}$$

$$(3.64)$$

for plain strain, and

$$\bar{\boldsymbol{D}} = \frac{E_3}{1 - \frac{E_1}{E_3}\nu_3^2} \begin{bmatrix} \frac{E_1}{E_3} & \frac{E_1}{E_3}\nu_3^2 & 0 \\ \frac{E_1}{E_3}\nu_3^2 & 1 & 0 \\ 0 & 0 & \frac{G_3}{E_3}\left(1 - \frac{E_1}{E_3}\nu_3^2\right) \end{bmatrix} \qquad (3.65)$$

for plain stress, where E_1 and ν_1 are respectively the Young modulus and the Poisson ratio associated to the behavior in the plane of the strata, and E_3, G_3 and ν_3 are respectively the Young modulus, the shear modulus and the Poisson ratio corresponding to the direction normal to the strata.

3.6   Conclusions

The present work introduced a finite element model for the inverse design analysis of three-dimensional geometrically nonlinear statics problems with hyperelastic materials.

Anisotropic materials were handled without modifying the constitutive-equation software module developed for classical (direct) large deformation elastic analysis. An exact computation of the tangent matrix made possible to obtain an optimum convergence rate. Plane stress and plain strain models are also derived.

An example showed the excellent accuracy of the model, measured by its ability to recover the original mesh of the corresponding direct analysis.

Chapter 4

Inverse FEM for Large-Displacement Beams

Many design methods for compliant mechanisms model flexible links as large-deflection beam-type elements with prismatic cross-section. Modeling a beam using the 3D or plane stress inverse finite element method of the previous chapter is evidently a considerable waste of computational resources. This motivated the formulation of an *inverse finite element method for large-displacement beams* in the elastic range [AFC10], as an extension of the previous work in inverse finite element methods. It grants the determination of the initial shape of a beam such that it attains a specified design shape under the effect of service loads. The inverse FEM formulation for large-displacement beams is introduced in this chapter.

4.1   Introduction

The general IFEM approach in Fachinotti *et al.* [FCJ08] motivated the development of inverse FEM for large-displacement beams, aimed at the design of compliant mechanisms and two- and three-dimensional highly flexible beam structures. Compliant mechanisms have low mass and very high flexibility, so large displacements behavior ought to be considered. This IFEM is based on the non-linear beam formulation proposed by Cardona and Géradin [CG88, GC00].

Equilibrium equations are written in terms of Eulerian variables, however, constitutive equations are expressed in terms of Lagrangian variables. While in the *geometrically exact beam theory* equations are derived directly from a three-dimensional non-linear theory and the appropriate kinematic assumptions are taken afterward, the work presented here proceeds as in [CG88, GC00] where kinematic beam assumptions are formulated before expressing non-linear strain measures.

Two simple tests were proposed for validation purposes. The first one was the two-dimensional bending of a cantilever beam, for which an analytical solution is available [How01]. The second problem is the 45-degree bend of a cantilever beam, which has been widely used as a benchmark for three-dimensional flexible beams models [CG88, GC00, BB79, SVQ86, DOO88].

4.2   Beam Kinematics

Let us consider a beam of cross-section $\mathcal{A}_0$ and length L, with initial configuration $\mathcal{B}_0 = \mathcal{A}_0 \times [0, L] \in R^3$ and current deformed configuration $\mathcal{B} = \mathcal{A} \times [0, l] \in R^3$ (Figure 4.1). We assume deformation of the beam takes place such that the cross-section does not change and remains plane; however, shear effects make the cross-section to not remain normal to the centroidal line [CG88, GC00].
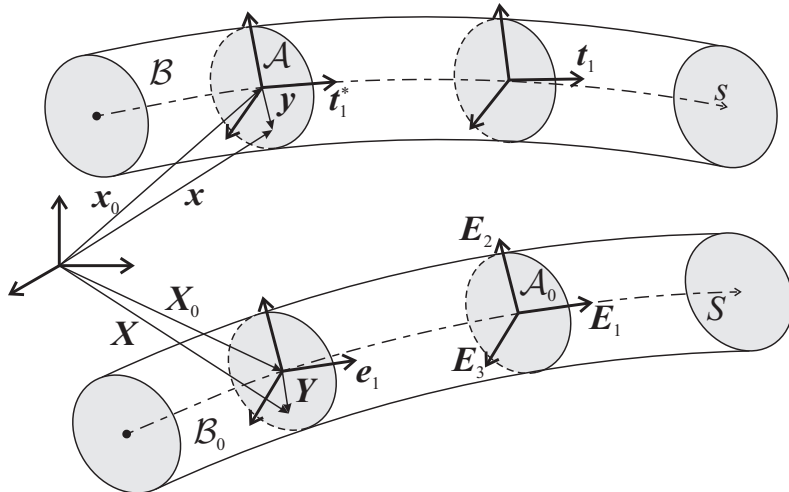
Figure 4.1: Description of beam kinematics.

The current position $\boldsymbol{x} \in \mathcal{B}$ of a generic point can be expressed as

$$\boldsymbol{x}(s) = \boldsymbol{x}_0(s) + \boldsymbol{y}(s)$$

where s is the length parameter along the neutral axis of the beam, $\boldsymbol{x}_0$ is the trace of the neutral axis on the cross section $\mathcal{A}$ containing the point $\boldsymbol{x}$ and normal to the neutral axis, and $\boldsymbol{y}$ is the position of $\boldsymbol{x}$ in the cross section relative to $\boldsymbol{x}_0$.

Before deformation, this same material point occupied the position $\boldsymbol{X} \in \mathcal{B}_0$:

$$\boldsymbol{X}(S) = \boldsymbol{X}_0(S) + \boldsymbol{Y}(S)$$

where S is the length parameter along the neutral axis of the undeformed beam, $\boldsymbol{X}_0 \in \mathcal{B}_0$ is the position occupied by the point at $\boldsymbol{x}_0 \in \mathcal{B}$ before deformation, and $\boldsymbol{Y}$ is the position of $\boldsymbol{X}$ relative to $\boldsymbol{X}_0$.

Vectors $\boldsymbol{y}$ and $\boldsymbol{Y}$ are related by

$$\boldsymbol{Y} = \boldsymbol{R}^T \boldsymbol{y} \tag{4.1}$$

where $\boldsymbol{R}$ is the so-called rotation operator, which belongs to the Lie group of proper orthogonal linear transformations. Since sections are assumed to remain plane during deformation, the transformation (4.1) is constant on the cross section $\mathcal{A}$.

Let $\{\boldsymbol{E}_1, \boldsymbol{E}_2, \boldsymbol{E}_3\}$ be an orthonormal basis in $\mathcal{B}_0$, such that $\boldsymbol{E}_1 = \mathrm{d}\boldsymbol{X}_0/\mathrm{d}S$ is normal to the cross section $\mathcal{A}_0$, and $\boldsymbol{E}_2$ and $\boldsymbol{E}_3$ define the principal axes of inertia of the cross section $\mathcal{A}_0$ of the undeformed beam. The corresponding orthonormal triad in $\mathcal{B}$ is $\{\boldsymbol{t}_1, \boldsymbol{t}_2, \boldsymbol{t}_3\}$, with

$$\boldsymbol{t}_i = \boldsymbol{R}\boldsymbol{E}_i \quad i = 1, 2, 3$$

Let us also consider an orthonormal basis $\{\boldsymbol{t}_1^*, \boldsymbol{t}_2^*, \boldsymbol{t}_3^*\}$ in $\mathcal{B}$, such that $\boldsymbol{t}_1^* = \mathrm{d}\boldsymbol{x}_0/\mathrm{d}s$ is normal to the cross section $\mathcal{A}$ and tangent to the neutral axis, and $\boldsymbol{t}_2^*, \boldsymbol{t}_3^*$ are aligned along the directions of the principal axes of inertia of the

cross-section. The corresponding orthonormal triad in $\mathcal{B}$ is $\{e_1, e_2, e_3\}$, with

$$e_i = R^T t_i^* \qquad i = 1, 2, 3$$

Note that although t_1^* and E_1 are aligned with the neutral axes in $\mathcal{B}$ and $\mathcal{B}_0$ respectively, e_1 and t_1 are not in general aligned with the neutral axes in $\mathcal{B}_0$ and $\mathcal{B}$ because of shear deformation. We remark that, for the same reason, $\mathcal{A}$ and $\mathcal{A}_0$ do not contain the same material points.

In the inverse analysis, the variables x_0 that determine $\mathcal{B}$ are assumed to be known. Then, we have to solve a problem for the unknowns X_0 and R in order to completely determine $\mathcal{B}_0$.

4.2.1   Parametrization of rotations

Let us introduce the Cartesian rotational vector ψ, which is defined as the vector whose direction is that of the rotation axis n and whose length is equal to the amplitude of the rotation ψ:

$$\psi = n\psi$$

Using ψ, the rotation operator in three dimensional space is completely determined by means of Rodrigues' formula:

$$R(\psi) = I + \frac{\sin\psi}{\psi}\widetilde{\psi} + \frac{1 - \cos\psi}{\psi^2}\widetilde{\psi}\widetilde{\psi} \qquad (4.2)$$

where I is the identity matrix and, from now on, $\widetilde{u}$ is the skew-symmetric matrix associated to the vector u given as

$$\widetilde{u} = \begin{bmatrix} 0 & -u_3 & u_2 \\ u_3 & 0 & -u_1 \\ -u_2 & u_1 & 0 \end{bmatrix}$$

Using this operator, the cross product of two vectors u and v can be obtained as

$$u \times v = \widetilde{u}v$$

Let us note that $\boldsymbol{R} \to \boldsymbol{I}$ when $\psi \to 0$.

Since $\boldsymbol{\psi}$ suffices to completely describe the rotation $\boldsymbol{R}$, we consider the minimal set of variables $\{\boldsymbol{X}_0, \boldsymbol{\psi}\}$ –instead of $\{\boldsymbol{X}_0, \boldsymbol{R}\}$– as unknown fields of the inverse problem.

4.2.2 Spatial deformation measures

Material deformation measures are given by the vectors of deformation of the neutral axis $\boldsymbol{\Gamma}$ and curvature $\boldsymbol{K}$ [GC00]:

$$\boldsymbol{\Gamma} = \boldsymbol{R}^T \frac{\mathrm{d}\boldsymbol{x}_0}{\mathrm{d}S} - \frac{\mathrm{d}\boldsymbol{X}_0}{\mathrm{d}S}$$
$$\boldsymbol{K} = \boldsymbol{T} \frac{\mathrm{d}\boldsymbol{\psi}}{\mathrm{d}S}$$

where $\boldsymbol{T}$ is the tangent operator

$$\boldsymbol{T}(\boldsymbol{\psi}) = \boldsymbol{I} + \frac{\cos\psi - 1}{\psi^2} \widetilde{\boldsymbol{\psi}} + \left(1 - \frac{\sin\psi}{\psi}\right) \widetilde{\boldsymbol{\psi}} \widetilde{\boldsymbol{\psi}} \tag{4.3}$$

(note that $\boldsymbol{T} \to \boldsymbol{I}$ as $\psi \to 0$).

The spatial counterparts of vectors $\boldsymbol{\Gamma}$ and $\boldsymbol{K}$, say $\boldsymbol{\gamma}$ and $\boldsymbol{\kappa}$ respectively, are obtained by applying a rotation to the current configuration:

$$\boldsymbol{\gamma} = \boldsymbol{R}\boldsymbol{\Gamma} = \frac{\mathrm{d}\boldsymbol{x}_0}{\mathrm{d}S} - \boldsymbol{R} \frac{\mathrm{d}\boldsymbol{X}_0}{\mathrm{d}S}$$
$$\boldsymbol{\kappa} = \boldsymbol{R}\boldsymbol{K} = \boldsymbol{R}\boldsymbol{T} \frac{\mathrm{d}\boldsymbol{\psi}}{\mathrm{d}S}$$

Since the length parameter S along the undeformed beam can be expressed as a function of the current length parameter s, the derivative of any function ϕ with respect to S can be computed using the chain rule:

$$\frac{\mathrm{d}\phi}{\mathrm{d}S} = \frac{\phi'}{S'}$$

with $(*)' \equiv \mathrm{d}(*)/\mathrm{d}s$. Then, the *spatial* measures of the deformation of the neutral axis and curvature, referred to the *known deformed frame*, can be

computed using the expressions:

$$\boldsymbol{\gamma} = \frac{1}{S'} \left(\boldsymbol{x}_0' - \boldsymbol{R} \boldsymbol{X}_0' \right) \tag{4.4}$$

$$\boldsymbol{\kappa} = \frac{1}{S'} \boldsymbol{R} \boldsymbol{T} \boldsymbol{\psi}' \tag{4.5}$$

4.3   Governing Equilibrium Equations

We formulate the equilibrium equations in the known deformed configuration $\mathcal{B}$ [FCJ08]. Let $\mathcal{A}$ be the cross-section containing point $\boldsymbol{x} \in \mathcal{B}$ and normal to the neutral axis in the deformed configuration. The area of $\mathcal{A}$ is assumed to be constant along the beam. Let us call $\boldsymbol{n}$ and $\boldsymbol{m}$ the resultant force and moment with respect to $\boldsymbol{x}_0$ of the tractions acting over the surface $\mathcal{A}$, and $\bar{\boldsymbol{n}}$ and $\bar{\boldsymbol{m}}$ the external force and moment per unit length at $\boldsymbol{x}$.

Then, assuming static conditions, the translational and rotational equilibrium equations at every point $\boldsymbol{x} \in \mathcal{B}$ can be expressed as follows:

$$\boldsymbol{n}' + \bar{\boldsymbol{n}} = \boldsymbol{0}$$

$$\boldsymbol{m}' + \boldsymbol{x}_0' \times \boldsymbol{n} + \bar{\boldsymbol{m}} = \boldsymbol{0}$$

The weak form of the equilibrium equations over $\mathcal{B}$ can be written as:

$$\int_{\mathcal{B}} \left(\boldsymbol{n}' + \bar{\boldsymbol{n}} \right)^T \delta \boldsymbol{X}_0 \, \mathrm{d}s + \int_{\mathcal{B}} \left(\boldsymbol{m}' + \boldsymbol{x}_0' \times \boldsymbol{n} + \bar{\boldsymbol{m}} \right)^T \delta \boldsymbol{\psi} \, \mathrm{d}s = 0$$

where $\delta \boldsymbol{X}_0$ and $\delta \boldsymbol{\psi}$ are admissible variations of $\boldsymbol{X}_0$ and $\boldsymbol{\psi}$.

Finally, after integration by parts, the equivalent variational problem takes the following form: *Find $\boldsymbol{X}_0(s)$ and $\boldsymbol{\psi}(s)$ such that*

$$\int_{\mathcal{B}} \left[\boldsymbol{n}^T \left(\delta \boldsymbol{X}_0' + \boldsymbol{x}_0' \times \delta \boldsymbol{\psi} \right) + \boldsymbol{m}^T \delta \boldsymbol{\psi}' \right] \, \mathrm{d}s = \int_{\mathcal{B}} \left(\bar{\boldsymbol{n}}^T \delta \boldsymbol{X}_0 + \bar{\boldsymbol{m}}^T \delta \boldsymbol{\psi} \right) \, \mathrm{d}s \tag{4.6}$$

for all admissible $\delta \boldsymbol{X}_0$ and $\delta \boldsymbol{\psi}$.

4.3.1 Constitutive equations

Let us make the following assumptions [GC00]:

- the material remains in the linear elastic range, and

- although the beam may undergo large rigid-body rotations, its material strains remain small.

Then, the following linear constitutive laws apply:

$$\boldsymbol{n} = \boldsymbol{C}^n \boldsymbol{\gamma} \tag{4.7}$$

$$\boldsymbol{m} = \boldsymbol{C}^m \boldsymbol{\kappa} \tag{4.8}$$

where $\boldsymbol{C}^n = C_{ij}^n \, \boldsymbol{t}_i^* \otimes \boldsymbol{t}_j^*$ and $\boldsymbol{C}^m = C_{ij}^m \, \boldsymbol{t}_i^* \otimes \boldsymbol{t}_j^*$ are the second order tensors of elastic integrated properties over the cross section. The matrices of elastic coefficients C_{ij}^n and C_{ij}^m referred to the principal axes of the deformed beam are written:

$$C^n = \begin{bmatrix} EA & 0 & 0 \\ 0 & GA_2 & 0 \\ 0 & 0 & GA_3 \end{bmatrix}, \quad C^m = \begin{bmatrix} GJ & 0 & 0 \\ 0 & EI_2 & 0 \\ 0 & 0 & EI_3 \end{bmatrix}$$

being EA the axial stiffness, GA_i the shear bending stiffness along the transverse axis $\boldsymbol{t}_i^*$, GJ the torsional stiffness, and EI_i the bending stiffness along the principal axis $\boldsymbol{t}_i^*$ $(i = 2, 3)$.

4.4 Finite Element Method

Based on the "direct" beam element proposed by Géradin and Cardona [GC00], the current "inverse" beam element representing the deformed configuration $\mathcal{B}$ is a straight, mixed linear-linear finite element. The element geometry is linearly interpolated:

$$\boldsymbol{x}_0(s) = \varphi_1(s)\boldsymbol{x}_0^1 + \varphi_2(s)\boldsymbol{x}_0^2, \quad 0 \leq s \leq l = \|\boldsymbol{x}_0^2 - \boldsymbol{x}_0^1\|$$

where $\boldsymbol{x}_0^i$ is the position of node i, $i = 1, 2$, and φ_i is the linear shape function associated to node i, defined as

$$\varphi_1 = 1 - \frac{s}{l}, \qquad \varphi_2 = \frac{s}{l}$$
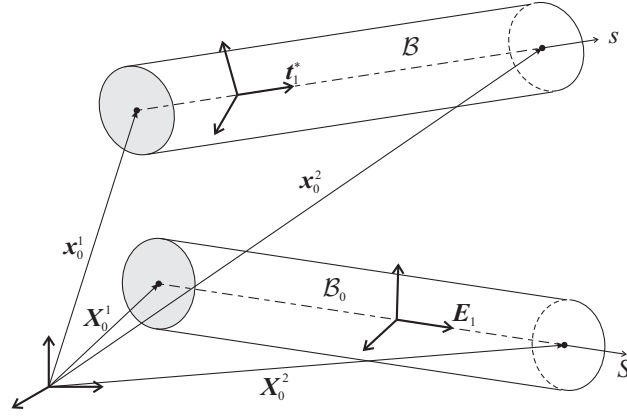
Figure 4.2: Finite element model of the inverse beam.

The unknowns of the inverse problem are approximated as follows:

$$\boldsymbol{X}_0(s) = \varphi_1(s)\boldsymbol{X}_0^1 + \varphi_2(s)\boldsymbol{X}_0^2 \tag{4.9}$$

$$\boldsymbol{\psi}(s) = \varphi_1(s)\boldsymbol{\psi}^1 + \varphi_2(s)\boldsymbol{\psi}^2 \tag{4.10}$$

where $\boldsymbol{X}_0^i$ and $\boldsymbol{\psi}^i$ are respectively the unknown values of $\boldsymbol{X}_0$ and $\boldsymbol{\psi}$ at node i.

Since $\boldsymbol{x}_0$ and $\boldsymbol{X}_0$ are both linearly interpolated, arc-length parameters s and S along the neutral axes in the deformed and undeformed configurations are related by the linear expression:

$$S = \frac{L}{l}s$$

with $L = \|\boldsymbol{X}_0^2 - \boldsymbol{X}_0^1\|$, and then

$$S' = \frac{L}{l}$$

4.4.1 Discretised equilibrium equations

Following the standard Galerkin finite element formulation [ZT00], we approximate the unknowns $\boldsymbol{X}_0$ and $\boldsymbol{\psi}$ as well as their their variations using equations (4.9) and (4.10). Then, the equilibrium equations (4.6) give rise to the following non-linear system of algebraic equations for the nodal unknowns $\boldsymbol{X}_0^i$ and $\boldsymbol{\psi}^i$:

$$\boldsymbol{F}_{int}(\boldsymbol{Q}) - \boldsymbol{F}_{ext} = \boldsymbol{0} \tag{4.11}$$

where $\boldsymbol{Q}$ is the vector of nodal unknowns defined as

$$\boldsymbol{Q} = \begin{bmatrix} \boldsymbol{X}_0^1 \\ \boldsymbol{\psi}^1 \\ \boldsymbol{X}_0^2 \\ \boldsymbol{\psi}^2 \end{bmatrix}$$

and where $\boldsymbol{F}_{int}$ and $\boldsymbol{F}_{ext}$ are the vectors of internal and external forces, respectively, given by

$$\boldsymbol{F}_{int} = \int_{\mathcal{B}} \boldsymbol{B}^T \boldsymbol{\sigma} \, \mathrm{d}s \quad , \qquad \boldsymbol{F}_{ext} = \int_{\mathcal{B}} \boldsymbol{\varphi}^T \bar{\boldsymbol{t}} \, \mathrm{d}s$$

with

$$\boldsymbol{B} = \begin{bmatrix} \varphi_1' \boldsymbol{I} & \varphi_1 \widetilde{\boldsymbol{x}_0'} & \varphi_2' \boldsymbol{I} & \varphi_2 \widetilde{\boldsymbol{x}_0'} \\ \boldsymbol{O} & \varphi_1' \boldsymbol{I} & \boldsymbol{O} & \varphi_2' \boldsymbol{I} \end{bmatrix}, \qquad \boldsymbol{\sigma} = \begin{bmatrix} \boldsymbol{n} \\ \boldsymbol{m} \end{bmatrix}$$

$$\boldsymbol{\varphi} = \begin{bmatrix} \varphi_1 \boldsymbol{I} & \boldsymbol{O} & \varphi_2 \boldsymbol{I} & \boldsymbol{O} \\ \boldsymbol{O} & \varphi_1 \boldsymbol{I} & \boldsymbol{O} & \varphi_2 \boldsymbol{I} \end{bmatrix}, \qquad \bar{\boldsymbol{t}} = \begin{bmatrix} \bar{\boldsymbol{n}} \\ \bar{\boldsymbol{m}} \end{bmatrix}.$$

Here, $\boldsymbol{O}$ is the 3×3 null matrix and $\boldsymbol{I}$ is the 3×3 identity matrix; note also that $\varphi_1' = -1/l$, $\varphi_2' = 1/l$ and $\boldsymbol{x}_0' = (\boldsymbol{x}_0^2 - \boldsymbol{x}_0^1)/l$ are constant within the element.

The external loads $\bar{\boldsymbol{n}}$ and $\bar{\boldsymbol{m}}$, are assumed to be given and independent of the unknowns; therefore the external force vector $\boldsymbol{F}_{ext}$ does not depend on the unknowns.

The internal force vector $\boldsymbol{F}_{int}$ depends on the unknowns via the internal efforts $\boldsymbol{\sigma}$, whose dependence on the unknowns will be analyzed in next section.

In order to avoid shear locking, $\boldsymbol{F}_{int}$ is evaluated using reduced integration with only one sampling point located at $s = l/2$, yielding:

$$\boldsymbol{F}_{int} = \boldsymbol{B}_{sp}^{T}\boldsymbol{\sigma}_{sp}\, l$$

where $(*)_{sp} \equiv *|_{s=l/2}$, and

$$\boldsymbol{B}_{sp} = \frac{1}{l}\begin{bmatrix} -\boldsymbol{I} & \frac{1}{2}\widetilde{\Delta\boldsymbol{x}_0} & \boldsymbol{I} & \frac{1}{2}\widetilde{\Delta\boldsymbol{x}_0} \\ \boldsymbol{O} & -\boldsymbol{I} & \boldsymbol{O} & \boldsymbol{I} \end{bmatrix}$$

with $\Delta\boldsymbol{x}_0 = \boldsymbol{x}_0^2 - \boldsymbol{x}_0^1$.

4.4.2 Computation of deformation and stress in the current finite element

By evaluating equations (4.4) and (4.5) at the sampling point, we obtain:

$$\boldsymbol{\gamma}_{sp} = \frac{1}{L}\left(\Delta\boldsymbol{x}_0 - \boldsymbol{R}_{sp}\Delta\boldsymbol{X}_0\right) \tag{4.12}$$

$$\boldsymbol{\kappa}_{sp} = \frac{1}{L}\boldsymbol{R}_{sp}\boldsymbol{T}_{sp}\Delta\boldsymbol{\psi} \tag{4.13}$$

with $\Delta\boldsymbol{X}_0 = \boldsymbol{X}_0^2 - \boldsymbol{X}_0^1$, $\Delta\boldsymbol{\psi} = \boldsymbol{\psi}^2 - \boldsymbol{\psi}^1$, and $\boldsymbol{R}_{sp} = \boldsymbol{R}(\boldsymbol{\psi}_{sp})$ and $\boldsymbol{T}_{sp} = \boldsymbol{T}(\boldsymbol{\psi}_{sp})$ are given by equations (4.2) and (4.3), respectively, evaluated at $\boldsymbol{\psi}_{sp} = (\boldsymbol{\psi}^1 + \boldsymbol{\psi}^2)/2$.

Now, the internal efforts at the sampling point are obtained using equations (4.7) and (4.8):

$$\boldsymbol{n}_{sp} = \boldsymbol{C}^n\boldsymbol{\gamma}_{sp}$$
$$\boldsymbol{m}_{sp} = \boldsymbol{C}^m\boldsymbol{\kappa}_{sp}$$

4.4.3 Linearization of the discrete equilibrium equations

The non-linear discrete equilibrium equations (4.11) are solved using the Newton-Raphson method [ZT00]. At each iteration k, the residual vector

$\boldsymbol{F} = \boldsymbol{F}_{int} - \boldsymbol{F}_{ext}$ is approximated using the linear Taylor expansion:

$$\boldsymbol{F}^{(k)} \approx \boldsymbol{F}^{(k-1)} + \boldsymbol{S}^{(k-1)}(\boldsymbol{Q}^{(k)} - \boldsymbol{Q}^{(k-1)}) = \boldsymbol{0}$$

where $\boldsymbol{S}^{(k-1)}$ is the tangent stiffness matrix:

$$\boldsymbol{S} = \frac{\mathrm{d}\boldsymbol{F}}{\mathrm{d}\boldsymbol{Q}}$$

evaluated at iteration $(k-1)$.

As already mentioned, only the internal forces are assumed to depend on the unknowns.

By differentiating $\boldsymbol{F}_{int}$ with respect to the unknowns $\boldsymbol{Q}$, we obtain

$$\boldsymbol{S} = l\boldsymbol{B}_{sp}^{T}\frac{\mathrm{d}\boldsymbol{\sigma}_{sp}}{\mathrm{d}\boldsymbol{Q}}$$

Then, it only remains to compute the derivatives of the stresses, evaluated at the sampling point $s = l/2$, with respect to $\boldsymbol{Q}$:

$$\frac{\mathrm{d}\boldsymbol{\sigma}_{sp}}{\mathrm{d}\boldsymbol{Q}} = \begin{bmatrix} \dfrac{\mathrm{d}\boldsymbol{n}_{sp}}{\mathrm{d}\boldsymbol{Q}} \\ \dfrac{\mathrm{d}\boldsymbol{m}_{sp}}{\mathrm{d}\boldsymbol{Q}} \end{bmatrix} = \begin{bmatrix} \boldsymbol{C}^{n} & \boldsymbol{O} \\ \boldsymbol{O} & \boldsymbol{C}^{m} \end{bmatrix} \begin{bmatrix} \dfrac{\mathrm{d}\boldsymbol{\gamma}_{sp}}{\mathrm{d}\boldsymbol{X}_{0}^{1}} & \dfrac{\mathrm{d}\boldsymbol{\gamma}_{sp}}{\mathrm{d}\boldsymbol{\psi}^{1}} & \dfrac{\mathrm{d}\boldsymbol{\gamma}_{sp}}{\mathrm{d}\boldsymbol{X}_{0}^{2}} & \dfrac{\mathrm{d}\boldsymbol{\gamma}_{sp}}{\mathrm{d}\boldsymbol{\psi}^{2}} \\ \dfrac{\mathrm{d}\boldsymbol{\kappa}_{sp}}{\mathrm{d}\boldsymbol{X}_{0}^{1}} & \dfrac{\mathrm{d}\boldsymbol{\kappa}_{sp}}{\mathrm{d}\boldsymbol{\psi}^{1}} & \dfrac{\mathrm{d}\boldsymbol{\kappa}_{sp}}{\mathrm{d}\boldsymbol{X}_{0}^{2}} & \dfrac{\mathrm{d}\boldsymbol{\kappa}_{sp}}{\mathrm{d}\boldsymbol{\psi}^{2}} \end{bmatrix}$$

4.4.4 Derivatives of deformation measures.

Derivatives of $\boldsymbol{\gamma}$.

From now on, let us obviate the subscript sp for notation convenience, keeping in mind however that all the variables are evaluated at the sampling point located at $s = L/2$.

By taking variations in equation (4.12), we obtain

$$\delta\boldsymbol{\gamma} = -\frac{1}{L}\boldsymbol{\gamma}\delta L - \frac{1}{L}\delta\boldsymbol{R}\Delta\boldsymbol{X}_{0} - \frac{1}{L}\boldsymbol{R}\delta(\Delta\boldsymbol{X}_{0}) \tag{4.14}$$

The variation of L takes the form

$$\delta L = \delta \|\Delta \boldsymbol{X}_0\| = \frac{1}{L} \Delta \boldsymbol{X}_0^T \delta(\Delta \boldsymbol{X}_0) \tag{4.15}$$

From [GC00], we know that

$$\delta \boldsymbol{R} \boldsymbol{u} = -\boldsymbol{R} \widetilde{\boldsymbol{u}} \boldsymbol{T} \delta \boldsymbol{\psi} \tag{4.16}$$

for an arbitrary vector $\boldsymbol{u}$. Then,

$$\delta \boldsymbol{R} \Delta \boldsymbol{X}_0 = -\boldsymbol{R} \widetilde{\Delta \boldsymbol{X}_0} \boldsymbol{T} \delta \boldsymbol{\psi}$$

Now, we can express the variation of $\boldsymbol{\gamma}$ given by equation (4.14) in terms of the variations $\delta \boldsymbol{\psi}$ and $\delta(\Delta \boldsymbol{X}_0)$ as follows:

$$\delta \boldsymbol{\gamma} = -\frac{1}{L} \left(\frac{1}{L} \boldsymbol{\gamma} \Delta \boldsymbol{X}_0^T + \boldsymbol{R} \right) \delta(\Delta \boldsymbol{X}_0) + \frac{1}{L} \boldsymbol{R} \widetilde{\Delta \boldsymbol{X}_0} \boldsymbol{T} \delta \boldsymbol{\psi}$$

Since $\delta \boldsymbol{\psi} = (\delta \boldsymbol{\psi}^1 + \delta \boldsymbol{\psi}^2)/2$ and $\delta(\Delta \boldsymbol{X}_0) = \delta \boldsymbol{X}_0^2 - \delta \boldsymbol{X}_0^1$, we derive from the above equation that:

$$\frac{\partial \boldsymbol{\gamma}}{\partial \boldsymbol{X}_0^1} = \frac{1}{L} \left(\frac{1}{L} \boldsymbol{\gamma} \Delta \boldsymbol{X}_0^T + \boldsymbol{R} \right) = -\frac{\partial \boldsymbol{\gamma}}{\partial \boldsymbol{X}_0^2}$$

$$\frac{\partial \boldsymbol{\gamma}}{\partial \boldsymbol{\psi}^1} = \frac{1}{2L} \boldsymbol{R} \widetilde{\Delta \boldsymbol{X}_0} \boldsymbol{T} = \frac{\partial \boldsymbol{\gamma}}{\partial \boldsymbol{\psi}^2}$$

Derivatives of κ.

By taking variations in equation (4.13), we obtain

$$\delta \boldsymbol{\kappa} = -\frac{1}{L} \boldsymbol{\kappa} \delta L + \frac{1}{L} \delta \boldsymbol{R} \boldsymbol{T} \Delta \boldsymbol{\psi} + \frac{1}{L} \boldsymbol{R} \delta \boldsymbol{T} \Delta \boldsymbol{\psi} + \frac{1}{L} \boldsymbol{R} \boldsymbol{T} \delta(\Delta \boldsymbol{\psi}) \tag{4.17}$$

Using equation (4.15), we have

$$\boldsymbol{\kappa} \delta L = \frac{1}{L} \boldsymbol{\kappa} \Delta \boldsymbol{X}_0^T \delta(\Delta \boldsymbol{X}_0)$$

Using equation (4.16), we have

$$\delta \boldsymbol{R} \boldsymbol{T} \Delta \boldsymbol{\psi} = -\boldsymbol{R} \widetilde{\boldsymbol{T} \Delta \boldsymbol{\psi}} \boldsymbol{T} (\delta \boldsymbol{\psi})$$

In order to compute the last term in the r.h.s. of equation (4.17), note that

$$\delta \boldsymbol{T} \Delta \boldsymbol{\psi} = \boldsymbol{A} \delta \boldsymbol{\psi}$$

with

$$\boldsymbol{A} = \left[\begin{array}{ccc} \dfrac{\partial \boldsymbol{T}}{\partial \psi_1} \Delta \boldsymbol{\psi} & \dfrac{\partial \boldsymbol{T}}{\partial \psi_2} \Delta \boldsymbol{\psi} & \dfrac{\partial \boldsymbol{T}}{\partial \psi_3} \Delta \boldsymbol{\psi} \end{array} \right]$$

Now, we can express the variation of $\boldsymbol{\kappa}$ given by equation (4.17) in terms of the variations $\delta \boldsymbol{\psi}$, $\delta(\Delta \boldsymbol{\psi})$ and $\delta(\Delta \boldsymbol{X}_0)$ as follows

$$\delta \boldsymbol{\kappa} = -\frac{1}{L^2} \boldsymbol{\kappa} \Delta \boldsymbol{X}_0^T \delta(\Delta \boldsymbol{X}_0) + \frac{1}{L} \boldsymbol{R} \left(\boldsymbol{A} - \widetilde{\boldsymbol{T} \Delta \boldsymbol{\psi}} \boldsymbol{T} \right) \delta \boldsymbol{\psi} + \frac{1}{L} \boldsymbol{R} \boldsymbol{T} \delta(\Delta \boldsymbol{\psi})$$

Since $\delta \boldsymbol{\psi} = (\delta \boldsymbol{\psi}^1 + \delta \boldsymbol{\psi}^2)/2$, $\delta(\Delta \boldsymbol{\psi}) = \delta \boldsymbol{\psi}^2 - \delta \boldsymbol{\psi}^1$ and $\delta(\Delta \boldsymbol{X}_0) = \delta \boldsymbol{X}_0^2 - \delta \boldsymbol{X}_0^1$, we get from the above equation that:

$$\frac{\partial \boldsymbol{\kappa}}{\partial \boldsymbol{X}_0^1} = \frac{1}{L^2} \boldsymbol{\kappa} \Delta \boldsymbol{X}_0^T = -\frac{\partial \boldsymbol{\kappa}}{\partial \boldsymbol{X}_0^2}$$

$$\frac{\partial \boldsymbol{\kappa}}{\partial \boldsymbol{\psi}^1} = \frac{1}{2L} \boldsymbol{R} \left(\boldsymbol{A} - \widetilde{\boldsymbol{T} \Delta \boldsymbol{\psi}} \boldsymbol{T} - 2 \boldsymbol{T} \right)$$

$$\frac{\partial \boldsymbol{\kappa}}{\partial \boldsymbol{\psi}^2} = \frac{1}{2L} \boldsymbol{R} \left(\boldsymbol{A} - \widetilde{\boldsymbol{T} \Delta \boldsymbol{\psi}} \boldsymbol{T} + 2 \boldsymbol{T} \right)$$

4.5 Validation Examples

4.5.1 Bending of a flexible cantilever beam

Let us consider the plane bending of a flexible cantilever beam with constant rectangular cross section, whose geometrical and material properties are listed in Table 4.1. We assume the beam is clamped at the origin of a reference frame O-xyz, and it is aligned along the x-axis in the undeformed configuration. It bends in the xz plane under a force $P = 10^5 \, \text{N}$ exerted at the free end in the z-direction. The magnitude of force is such that resulting deflections are large,

out of the range of linearized beam deflections equations.

Beam width	$b = 3\,\mathrm{cm}$
Beam height	$d = 6\,\mathrm{cm}$
Beam length	$L = 2\,\mathrm{m}$
Young modulus	$E = 2.10 \times 10^{11}\,\mathrm{N/m^2}$
Shear modulus	$G = 1.05 \times 10^{11}\,\mathrm{N/m^2}$

Table 4.1: Geometrical and material data for the problem of plane bending of a flexible cantilever beam.

In order to define the domain of inverse analysis, we need to know the whole elastica. An analytical expression of the elastica can be computed by assuming that shear effects on deformation are negligible. This hypothesis is well justified since the beam has a high slenderness ratio. The large deflection $w(x)$ of a cantilever beam with bending stiffness EI_y under a vertical load P applied at the free end is given by the solution of the differential equation:

$$\frac{\mathrm{d}^2 w}{\mathrm{d}x^2} + \frac{P}{EI}(x_{tip} - x)\left(1 + \frac{\mathrm{d}w}{\mathrm{d}x}\right)^{3/2} = 0$$

subject to the boundary conditions:

$$w(0) = 0, \qquad \left.\frac{\mathrm{d}w}{dx}\right|_{x=0} = 0$$

The solution of the above boundary value problem is

$$w(x) = \int_0^x \frac{1}{\sqrt{\beta^2(\chi) - 1}}\,\mathrm{d}\chi, \qquad 0 \le x \le x_{tip} \tag{4.18}$$

with

$$\beta(\chi) = \left[\frac{P}{EI}\left(x_{tip}\chi - \frac{\chi^2}{2}\right)\right]^{-1}$$

This integral does not have a closed solution, and is numerically evaluated using Gauss-Kronrod quadrature [Sha08] by setting the absolute tolerance to 10^{-10}. The position $\boldsymbol{x}_{tip} = [x_{tip}\ 0\ z_{tip}]^T$ and the rotation angle $\psi_{tip} = \|\boldsymbol{\psi}_{tip}\|$

of the loaded end after deformation are obtained by using Howell's elliptic-integral solutions [How01]:

$$x_{tip} = 1.408070 \, \text{m}$$

$$z_{tip} = 1.2843651 \, \text{m}$$

$$\psi_{tip} = 1.063764 \, \text{rad}$$
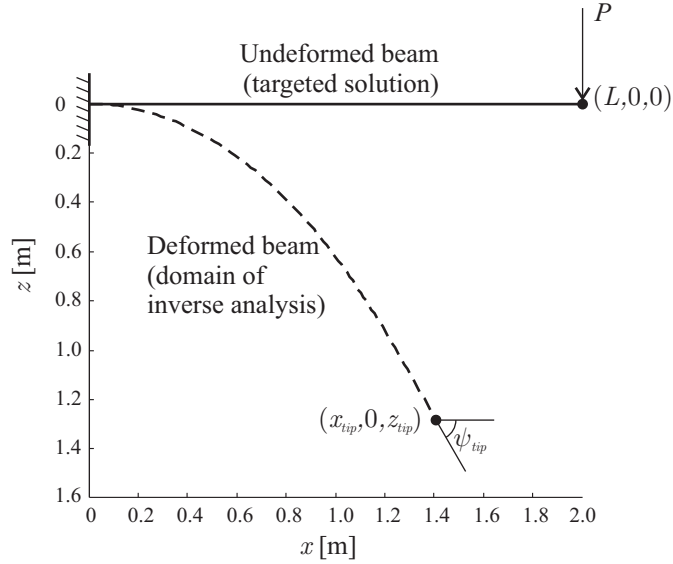
Figure 4.3: Plane bending of a flexible cantilever beam: undeformed and deformed neutral axes. Note that the scales for x and z are equal.

The deformed beam, as determined using equation (4.18), is depicted in Figure 4.3. This is actually the domain $\mathcal{B}$ of inverse analysis. Then, several meshes are defined by dividing $\mathcal{B}$ into $N = 2, 4, 8, 12, 16, 20$ segments of equal length $h = L/N$, each one approximated using a straight finite element. The target solution is the undeformed beam aligned with the x-axis.

Figure 4.4 depicts the L_2-norm of the error in initial position $\boldsymbol{X}_0$ and rotation $\boldsymbol{\psi}$ for the different meshes. It can be seen that for 20 finite elements the error in displacement is approximately of 10^{-3} m, which is very small compared to the dimensions of the beam (2 m long), demonstrating the accuracy of the

model. Note that a quadratic convergence rate is obtained for both error measures.

Concerning the performance of the Newton-Raphson solver, let us mention that for all the meshes considered here, it always took 6 iterations to attain $\|\boldsymbol{F}_{int} - \boldsymbol{F}_{ext}\| < 10^{-8}\|\boldsymbol{F}_{ext}\|$ starting from the initial guess $\boldsymbol{X}_0^i = \boldsymbol{x}_0^i$ and $\boldsymbol{\psi}^i = \boldsymbol{0}$ at every node i.

4.5.2   Cantilever 45-degrees bend

Let us now consider the cantilever 45-degrees bend depicted in Figure 4.5. The structure is clamped at the origin O of the reference frame $O\text{-}xyz$, and lies in the plane xy when undeformed. The beam has a unit square cross section, the Young modulus is $E = 10^7$ and the shear modulus is $G = 5 \times 10^6$. It is bent and twisted by the action of the force $P = 600$ applied at the free end, in the z-direction. This problem was used as a benchmark for three-dimensional
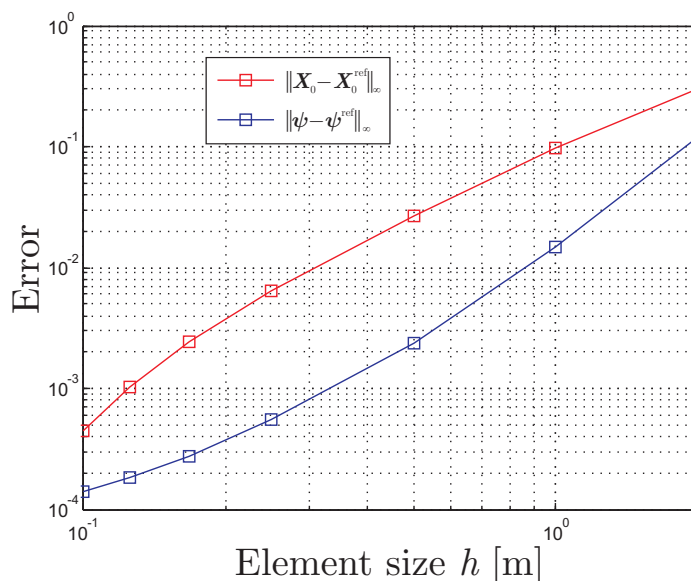

Figure 4.4: Bending of a flexible cantilever beam: errors in the approximation of positions and rotations (measured in L_2-norm) using the proposed inverse finite element model, as a function of the element size. For 20 finite elements the error in displacement is approximately of 10^{-3} m, which is very small compared to the dimensions of the beam (2 m long).

flexible beam models by several authors [CG88, GC00, BB79, SVQ86, DOO88].
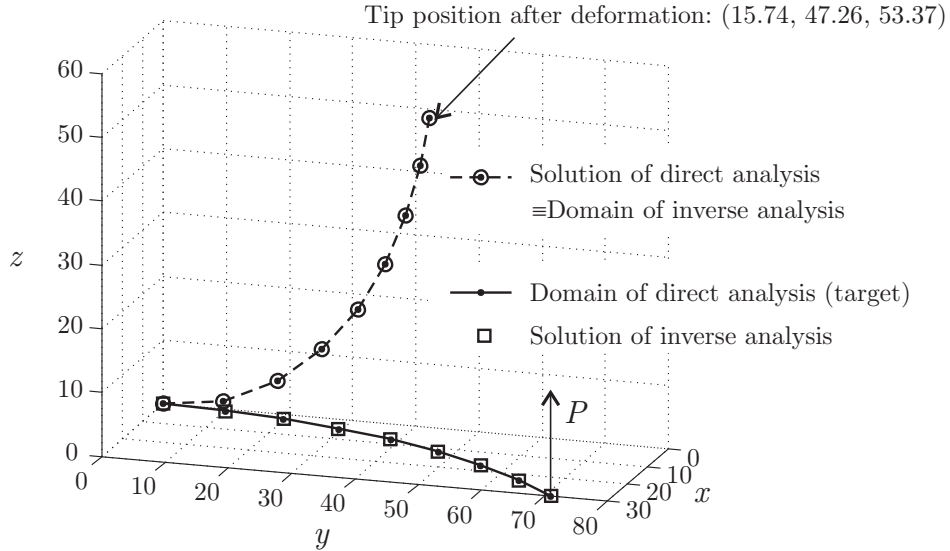
Figure 4.5: Cantilever 45-degree bend: solutions of direct and inverse analyses.

First, a direct analysis is performed. The beam is discretized using eight equal finite elements [CG88, GC00]. The computed position of the loaded end is shown in Figure 4.5. Then, an inverse analysis using the beam inverse model is performed, starting from a grid drawn on the computed deformed configuration. The solution of the inverse analysis should fit the original grid of the direct analysis. As it can be seen in Figure 4.5, the model is highly accurate, and almost complete agreement with the initial mesh is obtained. For instance, the distance between the given and the computed position at the free-end (loaded) node in the undeformed configuration is 0.1179 (less than 0.2% of the displacement at the same node).

A quadratic convergence rate was obtained for the Newton-Raphson iterations, taking 7 iterations to attain an equilibrium error norm $\|\boldsymbol{F}_{int} - \boldsymbol{F}_{ext}\| < 10^{-8}\|\boldsymbol{F}_{ext}\|$, starting from an initial guess $\boldsymbol{X}_0^i = \boldsymbol{x}_0^i$ and $\boldsymbol{\psi}^i = \boldsymbol{0}$ at every node i.

4.6   Conclusions

A finite element model for the inverse analysis of large-displacement beams has been presented. The objective in this kind of analysis is to solve inverse design problems, where the undeformed configuration is determined knowing the deformed configuration and the applied loads. A linear elastic constitutive relation is assumed.

Two and three-dimensional test-examples have been shown, illustrating the accuracy of the model. The performance was measured either by comparison to an analytical solution (2D case) or by its ability to recover the original mesh of the corresponding direct analysis (3D case).

Chapter 5

Design of compliant mechanisms that exactly fit a desired shape

Several applications of the inverse FEM for large-displacement beams introduced in the previous chapter are presented here. These consist in mechanisms and compliant structures with distributed and concentrated compliance. This inverse FEM allows to design compliant mechanisms that exactly fulfill the loaded mechanism shape, with lower computational costs compared with other design methods. It is specially suited for problems where an object has to be manipulated by the mechanism, allowing to maximize contact points between the mechanism and the object geometry. In particular, grippers, pliers and brakes are studied here, where results show a perfect matching of the contact shapes.

5.1   Compliant joint

A compliant joint used as a non-linear transmission between the motors and the moving link of a robot was proposed by Palli *et al.* [PMBV10], where the desired flexibility of the joint is achieved by exploiting the characteristics of four-bar mechanisms. This mechanism connects two concentric shafts (Figure 5.1 on the left). Compliant transmission elements (CTE) offer advantages over rigid counterparts, such as protection of actuators from shock due to

impact of moving links with stiff objects, the compactness of the resulting designs and customization of the flexibility. This is an example of a compliant mechanism with concentrated compliance, in which Palli et al. [PMBV10] used an optimization scheme in order to achieve the design constraints (desired shape under loading).
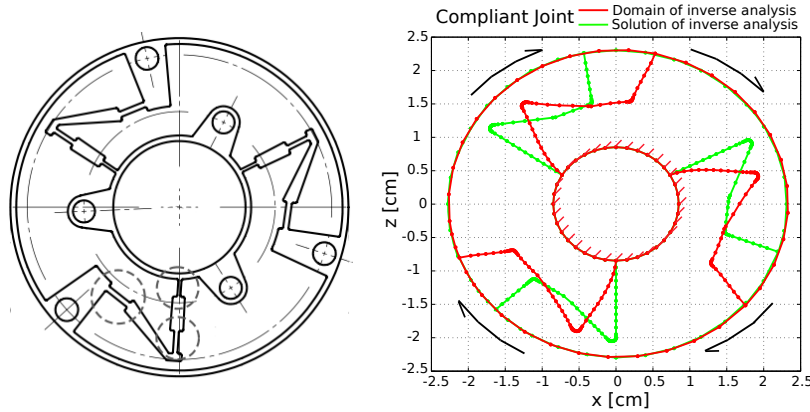
Figure 5.1: A compliant joint with distributed compliance proposed in [PMBV10] (left), and the solution computed with the inverse FEM for large-displacement beams (right). The inner circle of the joint is fixed to the ground, and torque is applied to the outer circle in order to deform the model.

The joint under study is made of an aluminum alloy with Young modulus $E = 69 \times 10^3 \, \text{N/mm}^2$ and shear modulus $G = 25 \times 10^3 \, \text{N/mm}^2$. Its outer diameter is 46 mm, and has a constant width of 4.7 mm. Links have a constant height of 5 mm (resulting in a 5 mm height and 4.7 mm width cross-section). For the finite element inverse analysis, the desired shape of the entire mechanism was discretized using 254 beam elements of equal length (each element is a two node-straight element, so more elements means better approximation to curved links). The inner circle of the joint is fixed to the ground, and torque is applied to the outer circle in order to deform the joint. Identical torque/deflection relations to the ones computed by [PMBV10] are obtained using inverse fem. The solid line in Figure 5.1 on the right represents the computed undeformed shape for manufacturing the joint, in order to verify the design requirements. The analysis took 12 Newton-Raphson iterations to attain an equilibrium error norm $\|\boldsymbol{F}_{int} - \boldsymbol{F}_{ext}\| < 10^{-8}\|\boldsymbol{F}_{ext}\|$ starting from

the initial guess $\boldsymbol{X}_0^i = \boldsymbol{x}_0^i$ and $\boldsymbol{\psi}^i = \boldsymbol{0}$ at every node i.

5.2 Compliant S-clutch

This mechanism connects two concentric shafts (Figure 5.2). When deformed under the effect of given centrifugal loads, the clutch shoe must engage the friction surface of the outer drum. The objective is to design a clutch that engages at a certain angular speed. The deformed geometry of the clutch should match very closely the geometry of the drum, to ensure a smooth distribution of the contact force between both surfaces. This reduces stress concentration and makes wear evenly distributed in the contact surfaces. Crane [Cra99] studied this kind of mechanisms using a pseudo-rigid body model. We refer to [Wei04] for several examples of industrial S-clutches.
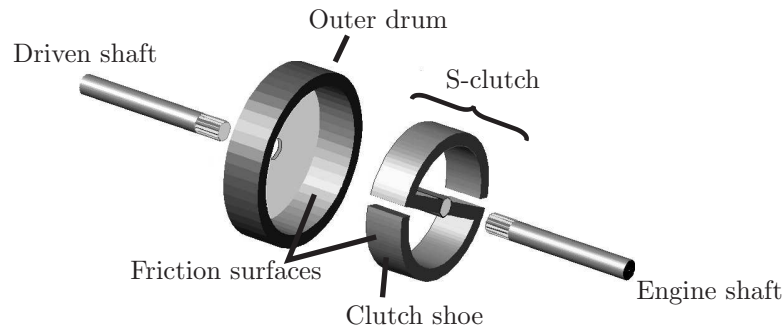
Figure 5.2: A compliant S-clutch.

The S-clutch studied here is made of an aluminum alloy with Young modulus $E = 69 \times 10^3 \,\mathrm{N/mm}^2$ and shear modulus $G = 25 \times 10^3 \,\mathrm{N/mm}^2$. In order to simplify the manufacture of the piece, the clutch shoes are assumed to have a constant rectangular cross section (30 mm wide, 10 mm high). A second design requirement is that the clutch matches the inner diameter of the drum (110 mm) when the angular speed is 1000 RPM. The model is fixed at the radius center.

For the inverse FEM analysis, the desired shape was discretized using 64 beam elements of the same length. The solid line in Figure 5.3 represents the computed undeformed shape for manufacturing the clutch in order to verify
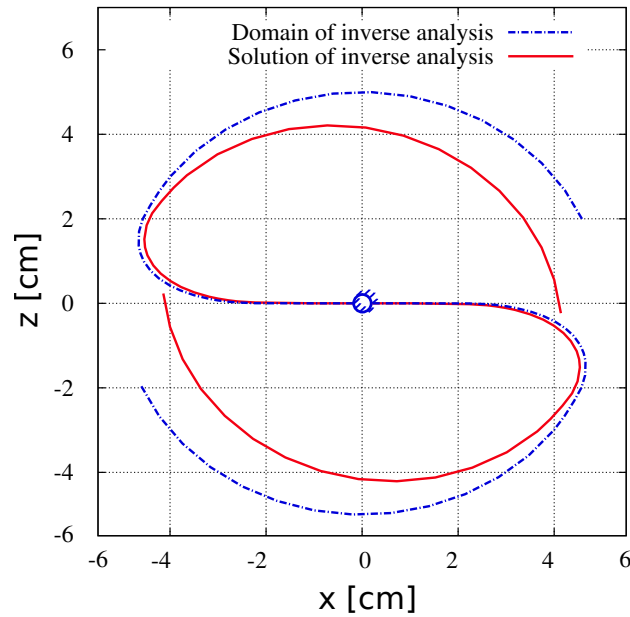
Figure 5.3: Compliant S-clutch: deformed (given design requirement), and undeformed (computed) configuration. The model is fixed to the ground at the center.

the design requirements. The analysis took 5 Newton-Raphson iterations to attain an equilibrium error norm $\|\boldsymbol{F}_{int} - \boldsymbol{F}_{ext}\| < 10^{-8}\|\boldsymbol{F}_{ext}\|$ starting from the initial guess $\boldsymbol{X}_0^i = \boldsymbol{x}_0^i$ and $\boldsymbol{\psi}^i = \boldsymbol{0}$ at every node i.

5.3   Compliant gripper

A simple compliant gripper was proposed by Lan and Cheng [LC07], which allows to grab an object of a certain size and shape when acted upon. They carried out a direct analysis using intrinsic functions to parameterize the topology and the generalized multiple shooting method (GMSM) to analyze the deflection of the mechanisms. These techniques were then integrated into an optimization scheme in order to achieve the design constraints (desired shape under loading).

Figure 5.4 depicts the target loaded shape in dashed line and the actuation force $P = 24\,\text{N}$, as computed by Lan and Cheng using a quadratic polynomial to parameterize the angle of rotation of the beam axis. The gripper has con-

stant rectangular cross section (10 mm wide and 5 mm high). It is made of polypropylene, with Young modulus $E = 1.4 \times 10^3 \, \text{N/mm}^2$ and Poisson ratio $\nu = 0.25$.
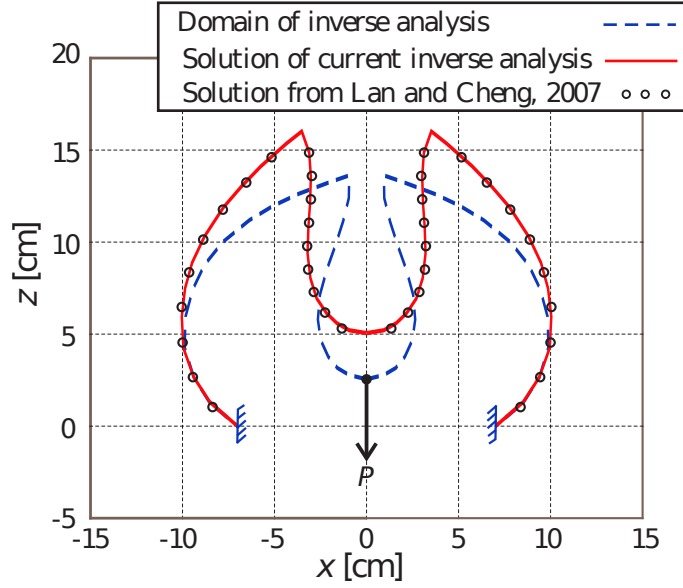
Figure 5.4: Compliant gripper: deformed (given design requirement) and undeformed (computed) configurations. Comparison with a reference solution [LC07]. The actuation force is $P = 24 \, \text{N}$.

If we take as domain of analysis the desired shape of the gripper when actuated, we can apply the method of inverse analysis to compute the unknown initial shape. The deformed gripper is modeled using 46 flexible beam finite elements. The undeformed configuration obtained as solution of the current inverse analysis is depicted in solid line in Figure 5.4. This solution agrees with that of Lan and Cheng, depicted in hollow circles in the same figure. The solution of the discrete non-linear equation using the Newton-Raphson method took 6 iterations to get an equilibrium error norm $\|\boldsymbol{F}_{int} - \boldsymbol{F}_{ext}\| < 10^{-8} \|\boldsymbol{F}_{ext}\|$, starting from the initial guess $\boldsymbol{X}_0^i = \boldsymbol{x}_0^i$ and $\boldsymbol{\psi}^i = \boldsymbol{0}$ at every node i.

5.4 Compliant Biomedical Instruments

One of the fastest growing areas in Biomedical Engineering is *minimally invasive surgery* (MIS). Aided by the recent advances in millimeter and sub-millimeter scale engineering that allows the construction of miniature medical tools, MIS techniques have revolutionized surgery by allowing operations to be conducted trough incisions ranging from a few millimeters to centimeters [FG09]. These procedures have dramatically reduced the risk of infection, reduce the duration of surgery as well as recovery time, and reduced hospital stays with less cost and less scaring. Surgical instruments based on compliant mechanisms offer a number of potential advantages over traditional MIS instruments and current robotic systems, like precisely completion of complex movements and haptic feedback [KLK$^+$05]. Their monolithic nature eliminates wear debris, pinch points and lubrication, all of which are critical in the sensitive internal environment of the body. In what follows we present promising applications of inverse FEM in the design of compliant mechanisms for minimally invasive surgery instruments.

5.4.1 Compliant lens folding device

Intraocular lens (IOL) are used in cataract surgery as a replacement of the eyes natural lens, and have approximately 6 mm of diameter. Once folded, a soft IOLs is inserted through a small tube into the eye through incisions of 3.2 mm or less. This is not only clinically advantageous compared to other procedures due to faster recovery from surgery, but also reduce astigmatism. These new lenses can be folded to be inserted through a small tube into the eye. After the folded IOL has been pushed completely through a delivery tube introduced into the eye, the IOL memory causes it to spring back, regaining its original shape. Erdman and Loftness [EL05] propose a rigid four-bar mechanism to fold the lens, Figure 5.5. The fold is not symmetric, and the lens assumes a σ shape which is advantageous for delivery through a small diameter delivery tube.

A compliant folder assures a reliable and repeatable action, and it will not impart damage to the lens during the process as it's made of a single soft-
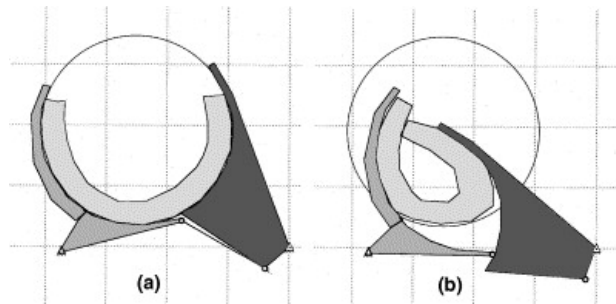
Figure 5.5: Rigid IOL folding device: inactive open position (left), and closed "sigma shaped" position, (right), by Erdman and Loftness [EL05].

curved flexible segment. Other advantage over its rigid counterparts is the reduced number of parts, i.e. it is monolithic and consists in only one piece. Not only this reduces manufacturing and assembly costs, but it is also simpler to sterilize.
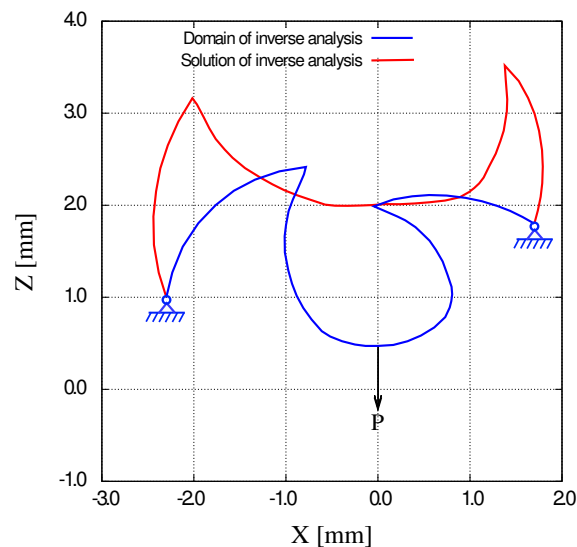
Figure 5.6: Inverse analysis results of the compliant IOL proposal. The model is hinged to the ground.

Figure 5.6 depicts the targeted deformed shape under an actuation force of 10 N. The compliant folder is made of polypropylene, with Young modulus $E = 1.4 \times 10^3 \, \text{N/mm}^2$ and Poisson ratio $\nu = 0.25$, and it's assumed to have a square cross section (2 mm high and wide). For the inverse FEM analysis,

the desired shape was discretized using 55 beam elements of equal length. The model is hinged to the ground, and the solid line represents the computed manufacture shape that will perfectly match the σ shape upon actuation in a safe and repeatable folding procedure. The analysis took 4 Newton-Raphson iterations to attain an equilibrium error norm $\|\boldsymbol{F}_{int} - \boldsymbol{F}_{ext}\| < 10^{-8}\|\boldsymbol{F}_{ext}\|$ starting from the initial guess $\boldsymbol{X}_0^i = \boldsymbol{x}_0^i$ and $\boldsymbol{\psi}^i = \boldsymbol{0}$ at every node i.

5.4.2   Compliant microvalves

Microfluidic systems are powerful tools for handling bio-molecules such as cells, DNA, RNA, proteins or neurons, and they range from disposable lab-on-chips to high output instruments. Micropumps ([LS04], [Woi05]), micromixers ([NW05])and microvalves ([KC06]) are typical microfluidic systems. Seidemann *et al.* [SBB01] proposed a *passive microvalve* (also known as a check valve) to seal a 200 μm microfluidic channel (Figure 5.7), which only opens to forward pressure, showing diode-like characteristics. It is operated by the pressure difference across the valve.
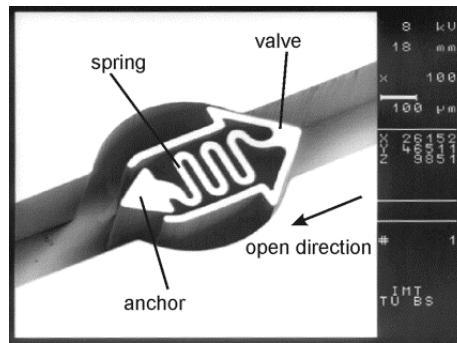
Figure 5.7: Flow channel with released check valve, [SBB01].

The check valve is fabricated of SU8, a monomer with a wide elastic range without plastic deformation, which has Young modulus E = 4×10^3 N/mm^2 and Poisson ratio $\nu = 0.22$. SU8 can be applied by masking, electroplating molds or injection molds, and this enables the design of complex planar structures.

Taking as domain of the analysis the desired shape of the valve under a specified pressure, inverse FEM can be applied to compute the unknown initial

(manufacture) shape. Applications range from the opening or closure of the valve at a specified pressure (such as a relief valve), mantention of a specified (constant) pressure drop in the microchannel, or bypassing a certain fluid flow.
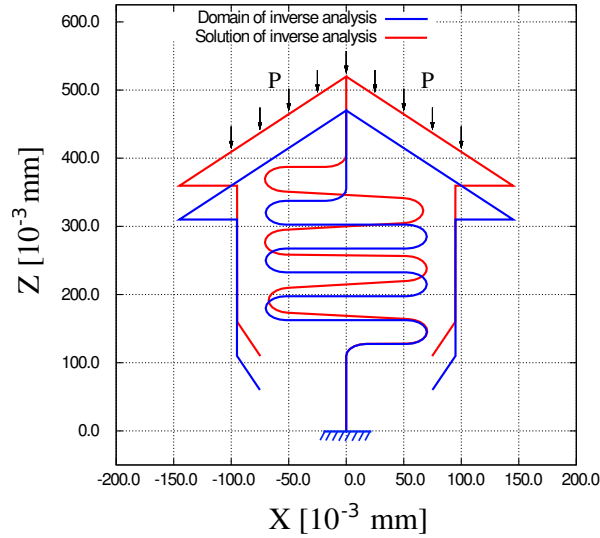
Figure 5.8: Inverse analysis of the check valve proposed by [SBB01].

Figure 5.8 depicts the targeted deformed valve under an actuation pressure P = 1.2 KPa. It is modelled using 85 flexible beam finite elements with constant rectangular cross section (h = 15 μm high and b = 20 μm wide), and it is fixed at the bottom. The solution of the discrete non-linear equation using the Newton-Raphson method took 7 iterations to get an equilibrium error norm $\|\boldsymbol{F}_{int} - \boldsymbol{F}_{ext}\| < 10^{-8}\|\boldsymbol{F}_{ext}\|$, starting from the initial guess $\boldsymbol{X}_0^i = \boldsymbol{x}_0^i$ and $\boldsymbol{\psi}^i = \boldsymbol{0}$ at every node i.

5.4.3 Compliant microgrippers

With the development of minimally invasive surgery (MIS), surgeons no longer needed to physically place their hands within the body to perform an operation. Instruments and viewing equipment are inserted into the body through small incisions, and the surgeon may now remotely teleoperate a robot in a comfortable, dexterous, and intuitive manner from outside the body [CKS04]. These devices may be manually driven prototypes, or servo-controlled by the

surgeon [CF99, FJ05]. Microgrippers fall in the operative instruments cat-
egory, and their size ranges from a few micrometers [WHH+06] to several
millimeters, being 5 mm the most common size [FG09]. In this category we
can also find other instruments such as forceps, scissors, retractors, clip pliers,
suturer and stapling devices to name a few [LE03]. As minimally invasive
surgery instruments become smaller, compliant mechanisms are an attractive
alternative to pin joined linkages and rigid parts. They can provide multiple
degrees of freedom in a single monolithic part, and can be scaled to smaller
sizes without encountering issues relating precision assembly [FSH+05].
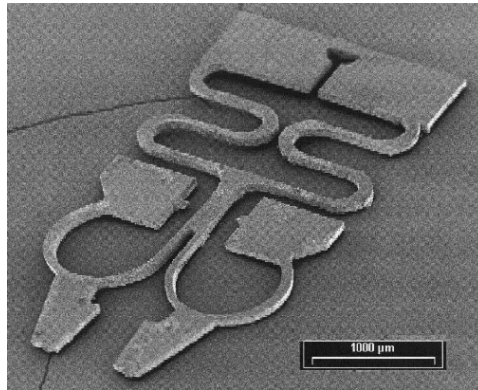
Figure 5.9: The SMA microgripper, [KJPM00].

The compliant microgripper proposed by Kohl *et al.* [KJPM00] (Figure 5.9)
is a $2 \times 3.9 \times 0.1$ mm^3 microgripper with a stress-optimized geometry, built
in a shape memory alloy (SMA) conceiving a high flexibility design. As the
geometry is made up of two circular beams on top and a folded beam structure
at the bottom it has distributed compliance behavior. When the microgripper
is acted by a force in the beam structure at the bottom, the circular beams
are deformed and the gripping jaws are closed.

Figure 5.10 depicts the target loaded shape in dashed line. The actuation
force is $P = 160$ μN. The microgripper has constant rectangular cross section
(0.5 mm wide and 0.5 mm high), and it is made of Nitinol, a super-elastic Ni-Ti
alloy with Young modulus E=28×10^3 N/mm^2 and Poisson ratio $\nu = 0.30$.

Inverse analysis was used to compute the unknown initial shape. The
deformed microgripper is modelled using 96 flexible beam finite elements. The
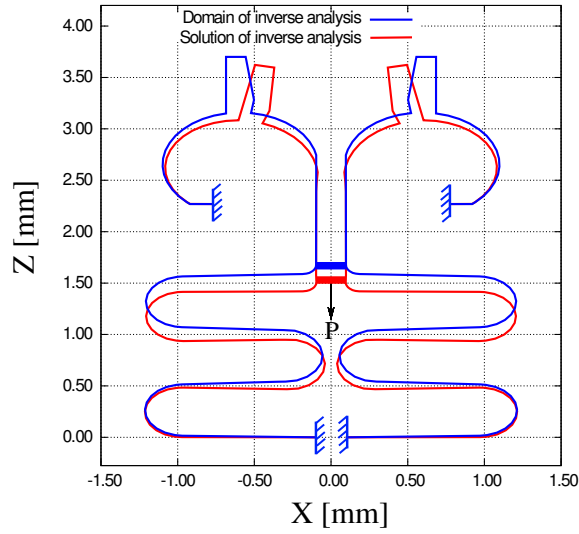
Figure 5.10: Inverse analysis results of the SMA microgipper proposed by [KJPM00].

undeformed configuration obtained as solution of the current inverse analysis is depicted in solid line in Figure 5.10. This solution agrees with that of [KJPM00]. The solution of the discrete non-linear equation using the Newton-Raphson method took 5 iterations to get an equilibrium error norm $\|\boldsymbol{F}_{int} - \boldsymbol{F}_{ext}\| < 10^{-8}\|\boldsymbol{F}_{ext}\|$, starting from the initial guess $\boldsymbol{X}_0^i = \boldsymbol{x}_0^i$ and $\boldsymbol{\psi}^i = \boldsymbol{0}$ at every node i.

5.5 Inverse FEM as a tool to design compliant mechanisms: advantages and disadvantages

In the previous section we have presented numerical applications of the inverse beam model applied to compliant mechanisms design. Inverse FEM allows to perfectly match the desired shapes of the objects. It is convenient to make some final comments of the advantages and inconveniences found in the design process while using inverse FEM.

5.5.1 Computational cost

The rate of convergence of the inverse beam model is quadratic (order 2), as it should be in any method using the Newton-Raphson algorithm [ZT00]. In general, the solutions obtained trough the use of the inverse finite element model demanded much less computational cost than the original solution procedure used by the respective author. Optimization was the preferred solution method by Lan and Cheng [LC07] in the compliant gripper, and by Kohl et al. [KJPM00] in the compliant microgripper. Only a few Newton-Raphson iterations are required to obtain a solution with IFEM, compared to the large amount of iterations needed in optimization problems.

In the other hand, Palli et al. [PMBV10] in compliant joints design, and Crane [Cra99] in compliant clutches design use the PRBM to create a mechanism and direct finite element models to compute the mechanisms performance. The inverse finite element model also proved to converge faster than the direct finite element model, what is another advantage of this method. The number of iterations and the residue norm are summarized in Table 5.1.

5.5.2 Stability check and feasibility of a design: detecting critical points

Once a design is obtained, the stability of the mechanism all along the deformation path[1] be verified, given that if stability is not satisfied, one cannot assure that the computed geometry in the inverse analysis will attain the design shape under the effect of service loads. If the path represents a configuration of static equilibrium it is called equilibrium path and each point on the load-deflection curve is called an equilibrium point. Certain points in the equilibrium path of a structure have special significance. A structure that is initially stable may lose stability as it moves to another equilibrium position. The non-linear equilibrium equation of the inverse finite element model

$$\boldsymbol{R} = \boldsymbol{F}(\boldsymbol{Q})_{int} - \boldsymbol{F}_{ext} \tag{5.1}$$

---

[1]The curve in the load-deflection diagram of a structure is called a path.

where $\boldsymbol{F(Q)}_{int}$ and $\boldsymbol{F}_{ext}$ are respectively the internal and external force vectors, is solved iteratively using the Newton-Raphson method. At each iteration k, the following linear equation is solved

$$\boldsymbol{R(Q^k)} = \boldsymbol{R(Q^{k-1})} + \boldsymbol{K(Q^{k-1})}\Delta\boldsymbol{Q} \tag{5.2}$$

where $\boldsymbol{K}$ denotes the tangent matrix, given by :

$$\boldsymbol{K} = \frac{\partial\boldsymbol{R}}{\partial\boldsymbol{q}} \tag{5.3}$$

and where $\boldsymbol{Q}$ is the vector of unknown nodal parameters, which in this case are the positions $\boldsymbol{X}_I$ and rotations $\boldsymbol{\psi}_I$ of the nodes in the initial configuration. In general, that transition from a stable to an unstable state is associated with the occurrence of *critical points* at which $\boldsymbol{K}$ becomes singular. Critical points have been classified into *limit points* (points at which the tangent to the equilibrium path is horizontal) and *bifurcation points* (points at which two or more equilibrium paths cross and there is an abrupt transition from one deformation mode to another). Other points of interest are *turning points* (points at which the tangent to the equilibrium path is vertical) and *failure points*(points at which the equilibrium path stops or breaks). All equilibrium points that are not critical are called *regular*. Stability is assessed by comparing the potential energy of the actual configuration with that of the equilibrium position. If all previous states have a higher potential energy, the actual equilibrium is stable. If at least one state has a lower (equal) potential energy the equilibrium is unstable.

There is no interest in tracing the equilibrium path in inverse FEM but rather to detect the occurrence of critical points, in which case two simple evaluation procedures may be used for this task[2]: the *determinant* test and the *spectrum* test of $\boldsymbol{K}$ [AG87, Cri00, Fel10]. Since the tangent stiffness matrix is singular at critical points, the most intuitive procedure consists in computing the determinant of $\boldsymbol{K}$. This approach is generally impractical given its computational cost. The spectrum test consists in the computation of the eigenvalues λ of the tangent matrix $\boldsymbol{K}$. The set of λ_i's are the solution of the

eigenproblem

$$\boldsymbol{K}\boldsymbol{z}_i = \lambda_i \boldsymbol{z}_i \tag{5.4}$$

where $\boldsymbol{z}_i$ are the eigenvectors corresponding to the eigenvalues λ_i. If $\boldsymbol{K}$ is real and symmetric (with real eigenvalues) a simple procedure can be used to detect critical points [Fel10]:

- If all $\lambda_i > 0$ the equilibrium position is strongly stable

- If all $\lambda_i \geq 0$ the equilibrium position is neutrally stable

- If some $\lambda_i < 0$ the equilibrium position is unstable

Given the small size of the problems under study we have adopted the *lowest eigenvalue test* criterion to evaluate stability at each loadstep, without altering the computational efficiency of the inverse method. If at a given loadstep the lowest eigenvalue is null or negative, the design is classified as non-feasible, and a new one must be proposed[3]. The results of lowest eigenvalue test criterion are summarized in Table 5.1.

Mechanism	Iterations	$\|\boldsymbol{F}_{int} - \boldsymbol{F}_{ext}\|$	Eigenvalues
Compliant joint	12	$< 10^{-8}\|\boldsymbol{F}_{ext}\|$	All positive
Compliant clutch	5	$< 10^{-8}\|\boldsymbol{F}_{ext}\|$	All positive
Compliant gripper	6	$< 10^{-8}\|\boldsymbol{F}_{ext}\|$	All positive
Compliant IOL folder	4	$< 10^{-8}\|\boldsymbol{F}_{ext}\|$	All positive
Compliant microvalve	7	$< 10^{-8}\|\boldsymbol{F}_{ext}\|$	All positive
Compliant microgripper	5	$< 10^{-8}\|\boldsymbol{F}_{ext}\|$	All positive

Table 5.1: Stability and computational costs of the example mechanisms

---

[2]They consist in searching for critical points without being concerned with tracing equilibrium paths up to those points.

[3]The discretization of the mechanism has a significant effect in the lowest eigenvalue test criterion, and this method may accuse an instability even if the mechanism is in strongly stable equilibrium. For example, if the discretization presents sharp edges or closed angles it is prone to have negative eigenvalues in the tangent matrix $\boldsymbol{K}$. However, the same mechanism but with a different discretization results in positive eigenvalues of matrix $\boldsymbol{K}$.

5.5.3   Intersections and interpenetrations

In some cases, intersections of beam elements exist in the undeformed configuration, resulting in a non-feasible mechanism where beam elements cross each other at areas that would invalidate the desired motion (that means that the code itself is not able to check that some elements are crossing each other in non-feasible ways). This happens even though inverse FEM started from a valid deformed geometry. The undeformed geometry of the compliant bicycle brake depicted in Figure 5.11 has intersections at the mid-length of the brakes's arms (we remark that the lines in these figures represent the beam axis and not the beam itself). The compliant gripper depicted in Figure 5.12 has multiple intersections beetween beam elements.
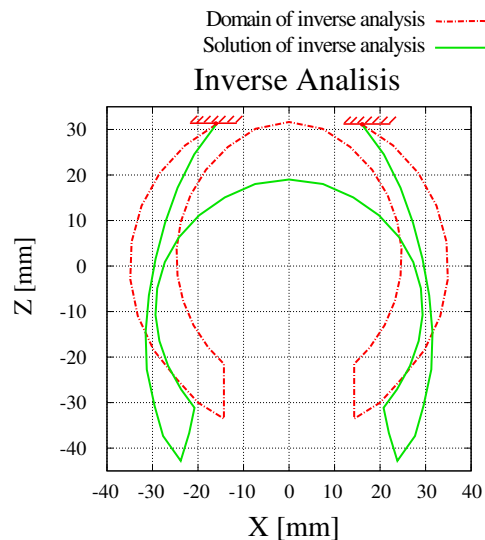
Figure 5.11: Non-feasible results for a compliant brake: the continuum line represents the beam axis in the undeformed geometry. Note that this line almost self-intersects at the mid-length of the brakes's arms, leading to undesired intersections and self-contact.

The compliant planar clutch depicted in Figure 5.13 has intersections between its arms, crossing itself in a spiral-like shape. Intersections led to trial and error design process (in which the variation of the beam cross-section or the material is needed to solve the issue). In most cases the use of intuition is sufficient to propose a new feasible design.
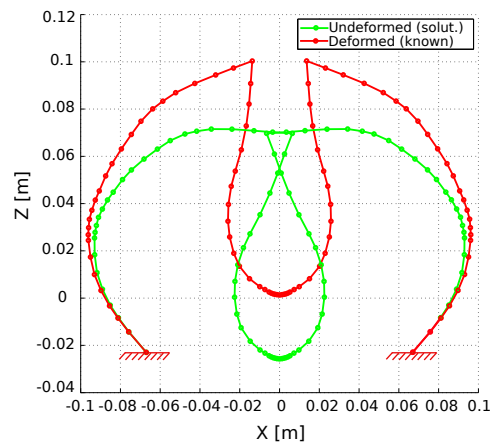
Figure 5.12: Non-feasible results for a compliant gripper: multiple self-crossing of beam elements.
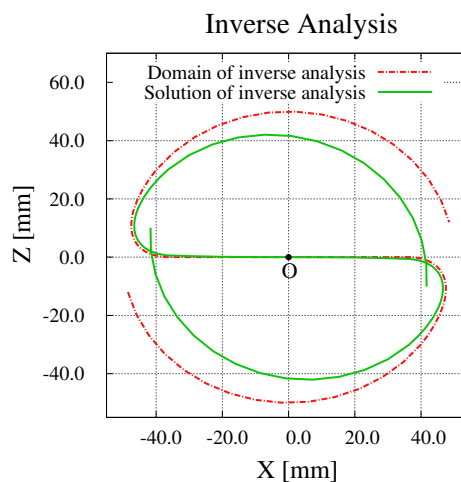
Figure 5.13: Self-crossing of beam elements in a planar clutch design. The model is fixed at the center point O.

The self-crossing of beam elements in a planar problem can be overcome by using 3D mechanisms. The nodal x and z coordinates of the 3D clutch design in Figure 5.14 are the same than those of the planar clutch, but the y coordinates of the arms in located in two different xz planes. This 3D design fulfills the design requirement and eliminates intersections. Nevertheless, it is important to remark that intersections and interpenetrations can ocurr in 3D mechanisms as well.
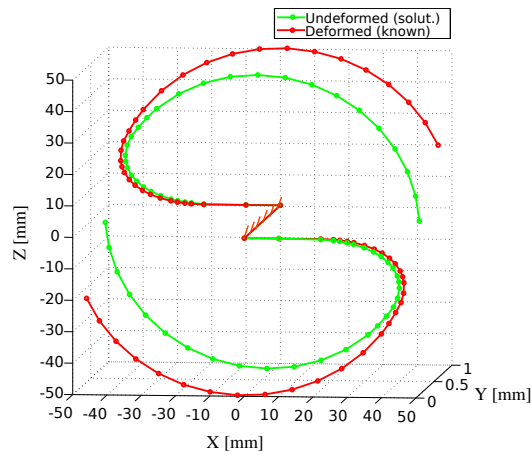
Figure 5.14: A feasible 3D clutch design that eliminates the self-crossing of beam elements present in its planar counterpart.

5.5.4 Violation of the design domain

Another inconvenient found while using the inverse finite element model was the violation of the design domain in some cases. As it evolves from the deformed to the undeformed configuration certain elements may be located outside of the allowed design domain in an intermediate configuration.
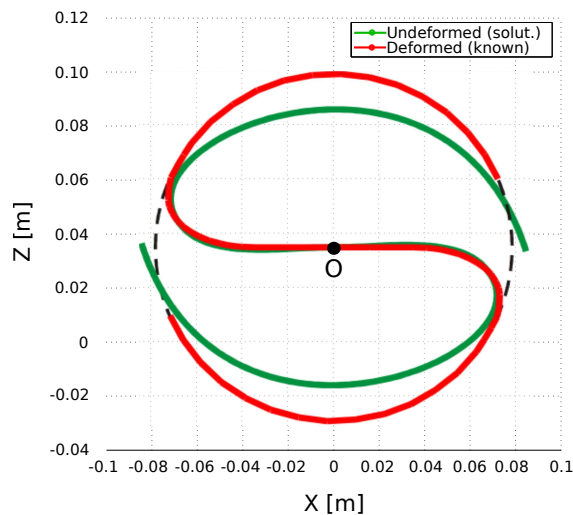
Figure 5.15: Violation of the design domain in the compliant clutch design. The model is fixed at the center point O.

Figure 5.15 depicts one of such cases, where in an intermediate configu-

ration (different from the deformed and undeformed configuration), the arms of the compliant clutch invade the boundary of the design domain. In other words, the arms of the clutch engage contact with the drum before the specified centrifugal load has been applied (at lower RPM than the specified), and this led to an unfeasible design. Again, the intuition of the designer is sufficient to propose a new alternative that grants a feasible design.

A possible way to interrupt the computation or to impose restrictions if this occurs would be to implement a simple contact problem of the type node-to-segment with penalty [PL04] or soft contact algorithms with friction for 3D beams [Lit07]. This in currently under study.

Chapter 6

Closure

6.1 Conclusions

The many advantages of compliant mechanisms compared to their rigid-body counterparts have produced a growing interest in compliant mechanism design and synthesis methods. This thesis has explored the use of different computational methods to design compliant mechanisms.

A novel methodology based in inverse FEM was developed and implemented, constituting a very useful tool that allows engineers to conceive designs in less time and at much lower costs than the ones involved in traditional experimental and optimization-based design, and avoids the trial and error approach used in the design process. It is specially suited for applications where an object has to be manipulated by the mechanism, allowing maximizing contact points between the mechanism and the object geometry.

The main contribution of this thesis is the development and use of inverse FEM to design compliant mechanisms, departing from classical design methods used up-to-date. This novel methodology permits to exactly compute the initial shape of a body such that it fulfills the specified design shape under service loads and undergoing large defections. The method is numerically efficient due to an analytically exact Newton-Raphson scheme. It is original since there is no background of inverse finite element methods among the procedures used to design compliant systems, and does not rely on the use of optimiza-

tion techniques. Compliant mechanisms and structures, with distributed and concentrated compliance, can be designed using inverse FEM with lower computational costs compared with other classical design methods.

The first approach to determine the mechanism design for a given task was based on optimization methods. Structural optimization methods (e.g. topology, size and shape) were tested in several applications. Results obtained with topology optimization methods are independent of prior design choices, allowing the user to create designs starting from scratch, being this perhaps the major advantage of this technique. Nevertheless, almost all algorithms used in topology optimization assume geometrically linear mechanical behavior, and inaccurate results may be obtained when applied to a compliant mechanisms that usually undergoes large displacement. Shape and size optimization were performed with different gradient-based algorithms. The computational cost is still the main drawback of these methods.

It became evident that IFEM could make important contributions in the field of compliant mechanism design, in particular as a re-design tool. Early work focused in a general inverse FEM for 3D solids, however, as most flexible links in compliant mechanisms can be modeled as large-deflection beams, it became evident that modeling a beam using the 3D or plane stress IFEM is a considerable waste of computational resources. This motivated the formulation of an inverse finite element method for large-displacement beams in the elastic range, as an extension of the previous work specifically addressed to the design of compliant mechanisms. The difference with respect to general 3D solid is that in beam elements it is not possible to precisely define principal transverse Lagrangian coordinates (used to derive the constitutive law) in the cross-section when torsional efforts are present. The workaround was the formulation of the problem in Eulerian form, in which principal axis can be defined since this is the current known (deformed) configuration, and the derivation of the constitutive law is straightforward.

The inverse FEM for large-displacement beams has a good computational efficiency, requiring only a few iterations to converge to a feasible solution. The stability and feasibility of the design is assessed by the lowest eigenvalue test criterion. Several 2D and 3D mechanisms, in the macro and micro-scale,

were successfully tested, and validated with great precision against the results of the literature, as for example compliant transmission mechanisms (clutch and joint), robotic surgery tools for minimally invasive surgery (grippers and microgrippers), and passive elements for microfluidic systems (microvalves).

The main flaws of this method at the present state are the intersection and interpenetration of beam elements, and the violation of the design domain. In the first case, intersections of beam elements result in a non-feasible design in which self-crossing of beam elements invalidate the desired motion. In the latter case, during the deformation of the body, some elements may be located outside of the specified design domain.

6.2   Further Research

Several shortcomings must be circumvented in order to extend the capabilities of IFEM and make it an automatic design tool.

Extension of the inverse FEM to large-displacement shells in the elastic range [ZL08] is currently in progress. This will allow to extending the model to sheet metal forming, deep drawing processes, and medical imaging technology of vascular organs, and detection of veins and arteries that tend to develop aneurysms [LZR07b]. The combination of different type of elements (beam, shell, solid, etc.) connected by kinematic joints to model flexible multibody would permit to construct a library of mechanical elements for IFEM analysis.

In the case of sheet metal forming or deep drawing modeling though IFEM, where large displacements in the plastic range are encountered, two approaches are found in the literature: a *one step* and the *multiple step* inverse approach. The work of Batoz [BGM98, GBN$^+$00, NBEB04, NDBG04b, NDBG04a] has focused in the one step inverse approach, where Hencky plasticity is used [Lub02], which is strictly valid for proportional loading and grants a preliminary solution to sheet metal forming problem when flexural efforts are predominant. Improvement in precision is achieved with the multiple step inverse approach [LC01, KKH01, KH02, YHCD06] where the load is applied gradually. However, even in this case, the assumption of proportional load is an excessive simplification of the problem. Under the assumption of proportional loading,

multiple step inverse FEM may be used as a tool to compute fast preliminary results, that may be used as a starting point in the search of more precise solutions using for instance, optimization algorithms [ABR11].

Contact algorithms are currently under study to consider friction forces (e.g in the compliant clutch), and to interrupt the computation or to impose restrictions if intersection and interpenetration occurs. For this purpose, contact models of the type node-to-segment with penalty [PL04] or soft contact algorithms with friction for 3D beams [Lit07] may be adequate choices.

Bibliography

[ABFJ97]   G. Allaire, E. Bonnetier, G. Francfort, and F. Jouve, *Shape opti-mization by the homogenization method*, Nümerische Mathematik **76** (1997), 27–68. 14

[ABR11]   M. Azaouzi, S. Belouettar, and G. Rauchs, *A numerical method for the optimal blank shape design*, Materials and Design **32** (2011), 756–765. 122

[ACS⁺01]   E. Andreassen, A. Clausen, M. Schevenels, B. S. Lazarov, and O. Sigmund, *Efficient topology optimization in matlab using 88 lines of code*, Structural and Multidisciplinary Optimization (2001). 26, 27

[AFC10]   A. Albanesi, V. Fachinotti, and A. Cardona, *Inverse finite ele-ment method for large-displacement beams*, International Journal for Numerical Methods in Engineering **84** (2010), 1166–1182. 20, 83

[AFPC07]   A. Albanesi, V. Fachinotti, M. Pucheta, and A. Cardona, *Syn-thesis of compliant mechanisms for segment-motion generation tasks*, Proceedings of Enief 2007. Córdoba, Argentina. Mecánica Computacional **26** (2007), 2919–2930. 37, 39

[AG87]   E L. Allgower and K. Georg, *Introduction to numerical continu-ation methods*, Society for Industrial Mathematics, 1987. 113

[All02]   G. Allaire, *Shape optimization by the homogenization method*, Springer, 2002. 14, 23

[Ana94]   G. K. Ananthasuresh, *A new design paradigm for Micro-Electro-Mechanical Systems and investigations on the compliant mechanism synthesis*, Ph.D. thesis, University of Michigan, Ann Harbor, USA, 1994. 2, 15

[ARFC06]   A. Albanesi, J. Risso, V. Fachinotti, and A. Cardona, *Optimization of ventilation holes in an aeronautic turbine disc*, Proceedings of Enief 2006. Santa Fe, Argentina. Mecánica Computacional **25** (2006), 1513–1530. 30, 37

[AVMC10]   R. Ansola, E. Veguer, A. Maturana, and J. Canales, *3d compliant mechanisms synthesis by a finite element addition procedure*, Finite Elements in Analysis and Design **46** (2010), 760–769. vi, 15, 17, 18

[BB79]   K. J. Bathe and S. Bolourchi, *Large displacement analysis of three-dimensional beam structures*, International Journal for Numerical Methods in Engineering **14** (1979), 961–986. 84, 99

[BDF02]   M. Bruyneel, P. Duysinx, and C. Fleury, *A family of MMA approximations for structural optimization*, Structural and Multidisciplinary Optimization, Springer-Verlag **24** (2002), 263276. 31

[Be89]   M. P. Bendsø e, *Optimal shape design as a material distribution problem*, Structural and Multidisciplinary Optimization, Springer-Verlag **1** (1989), 193–202. 14, 27

[Be95]   M. P. Bendsø e, *Optimization of structural topology, shape and material*, Springer-Verlag, New York, 1995. 15, 28

[BGM98]   J. L. Batoz, Y. Q. Guo, and F. Mercier, *The inverse approach with simple triangular shell elements for large strain predictions of sheet metal forming parts*, Engineering Computations **15** (1998), 864–892. 121

[BS04]   M. P. Bendsoe and O. Sigmund, *Topology optimization: Theory, methods and applications*, Springer-Verlag, Berlin, 2004. 9, 15

[BT01] T. E. Bruns and D. A. Tortorelli, *Topology optimization of non-linear elastic structures and compliant mechanisms*, Computer Methods in Applied Mechanics and Engineering **190** (2001), 3343–3459. v, 9

[BW98] J. V. Beck and K. A. Woodbury, *Inverse problems and parameter estimation: integration of measurements and analysis*, Measurement Science Technology **9** (1998), 839–847. 18, 62

[CF99] D. J. Cappelleri and M. I. Frecker, *Optimal design of smart tools for minimally invasive surgery*, Proceedings of Optimization in Industry II, Banff, Canada (1999). 110

[CG88] A Cardona and M. Géradin, *A beam finite element non-linear theory with finite rotations*, International Journal for Numerical Methods in Engineering **26** (1988), 2403–2438. vii, 42, 45, 46, 48, 83, 84, 99

[CKS04] D. B. Camarillo, T. M. Krummel, and K. Jr. Salisbury, *Robotic technology in surgery: past, present, and future*, The American Journal of Surgery **188** (2004), 2–15. 109

[Cra99] N. Crane, *Compliant centrifugal clutches: Design, analysis and testing*, Ph.D. thesis, Brigham Young University, Provo, Utah, USA, 1999. 103, 112

[Cri00] M. A. Crisfield, *Non-linear finite element analysis of solids and structures*, vol. I, John Wiley & Sons, 2000. vii, 42, 43, 113

[DOO88] E. N. Dvorkin, E. Oñate, and J. Oliver, *On a non-linear formulation for curved Timoshenko elements considering large displacements/rotations increments*, International Journal for Numerical Methods in Engineering **26** (1988), 1597–1613. 84, 99

[EL05] A. G. Erdman and P. E. Loftness, *Synthesis of linkages for cataract surgery: storage, folding and delivery of replacement*

                  intraocular lenses (iols), Mechanism and Machine Theory **40** (2005), 337–351. ix, 106, 107

[ES97]   A. G. Erdman and G. N. Sandor, *Mechanism design: Analysis and synthesis*, Prentice-Hall, 1997. 8

[FAN⁺97]   M. I. Frecker, G. K. Ananthasuresh, S. Nishiwaki, N. Kikuchi, and S. Kota, *Topological synthesis of compliant mechanisms using multi-criteria optimisation*, ASME Journal of Mechanical Design **119** (1997), 238–245. 15

[FCJ08]   V. Fachinotti, A. Cardona, and P. Jetteur, *Finite element modeling of inverse design problems in large deformations anisotropic hyperelasticity*, International Journal for Numerical Methods in Engineering **74** (2008), 894–910. ii, vi, 19, 20, 61, 83, 88

[FD65]   F. Freudenstein and L. Dobrjanskyj, *On a theory for the type synthesis of mechanisms*, Proceedings of 11th International Congress of Applied Mechanics, Springer-Verlag, Berlin (1965), 420–428. 12

[Fel10]   C. Felippa, *Class notes. nonlinear finite element methods*, University of Colorado at Boulder, USA, 2010. 113, 114

[FG09]   R. Fernandes and D. H. Gracias, *Toward a miniaturized mechanical surgeon*, Materials Today **12** (2009), 14–20. 106, 110

[FJ05]   M. Frecker and Snyder A. J., *Surgical robotics: Multifunctional end effectors for robotic surgery*, Operative Techniques in General Surgery **9** (2005), 165–69. 110

[Fle79]   C. Fleury, *Structural weight optimization by dual methods of convex programming*, International Journal for Numerical Methods in Engineering **14** (1979), 1761–1783. 26

[Fle89a]   C. Fleury, *Conlin: An efficient dual optimizer based on convex approximation concepts*, Structural Optimization **1** (1989), 81–89. 26

[Fle89b] C. Fleury, *First and second order convex approximation strategies in structural optimization*, Structural Optimization **1** (1989), 3–10. 32

[FSH⁺05] M. I. Frecker, J. Schadler, R. S. Haluck, K. Culkar, and R. Dziedzic, *Laparoscopic multifunctional instruments: Design and testing of initial prototypes*, Journal of the Society of Laparoscopic Surgeons **9** (2005), 105–112. 110

[GBN⁺00] Y. Q. Guo, J. L. Batoz, H. Naceur, S. Bouabdallah, F. Mercier, and O. Barlet, *Recent developments on the analysis and optimum design of sheet metal forming parts using a simplified inverse approach*, Computers and Structures **78** (2000), 133–148. 121

[GC00] M. Géradin and A. Cardona, *Flexible Multibody Dynamics. A Finite Element Approach*, John Wiley & Sons, Chichester, 2000. vii, 42, 45, 46, 83, 84, 87, 89, 94, 99

[GM96] S. Govindjee and P. A. Mihalic, *Computational methods for inverse finite elastostatics*, Computer Methods in Applied Mechanics and Engineering **136** (1996), 47–57. 19, 62, 63, 72, 73

[GM98] S. Govindjee and P. A. Mihalic, *Computational methods for inverse deformations in quasi-incompressible finite elasticity*, International Journal for Numerical Methods in Engineering **43** (1998), 821–838. vi, 19, 62, 63, 72

[HM87] I. Her and A. Midha, *A compliance number concept for compliant mechanisms and type synthesis*, ASME Transactions. Journal of mechanisms, transmissions and automation in design **109** (1987), 348355. 10

[HM94] L. L. Howell and A. Midha, *A method for the design of compliant mechanisms with small-length flexural pivots*, ASME Journal of Mechanical Design **115** (1994), 280–290. 11

[HM96]   L. L. Howell and A. Midha, *A loop-closure theory for the analysis and synthesis of compliant mechanisms*, ASME Journal of Mechanical Design **118** (1996), 121–125. 11

[HM03]   J. Haslinger and R. A. M'akinen, *Introduction to shape optimization: theory, approximation, and computation*, SIAM Technology Engineering, 2003. 14, 23

[How93]   L. L. Howell, *A generalized loop-closure theory for the analysis and synthesis of compliant mechanisms*, Ph.D. thesis, Purdue University, West Lafayette, Indiana, USA, 1993. 10

[How01]   L. L. Howell, *Compliant mechanisms*, John Wiley & Sons, 2001. v, 2, 3, 4, 5, 7, 8, 10, 14, 84, 97

[HV99]   J. A. Hetrick and S. Viota, *An energy formulation for parametric size and shape optimization of compliant mechanisms*, ASME Journal of Mechanical Design **121** (1999), 229–234. 15

[KBe88]   N. Kikuchi and M. P. Bendsø e, *Generating optimal topologies in structural design using a homogenization method*, Computer Methods in Applied Mechanics and Engineering **71** (1988), 197–224. 14, 15

[KC06]   W. O. Kwang and H. A. Chong, *A review of microvalves*, Journal of Micromechanics and Microengineering **16** (2006), 13–39. 108

[KH02]   S. H. Kim and H. Huh, *Construction of sliding constraint surfaces and initial guess shapes for intermediate steps in multi-step finite element inverse analysis*, Journal of Materials Processing Technology **131** (2002), 482–489. 121

[KHLS99]   S. Kota, J. Hetrick, Z. Li, and L. Saggere, *Tailoring unconventional actuators using compliant transmissions: Design methods and applications*, ASME Transactions on Mechatronics **4** (1999), 396–408. 2, 3

[Kir93]   U. Kirsch, *Structural optimization: Fundamentals and applications*, Springer, 1993. 24

[KJPM00]   M. Kohl, E. Just, W. Pfleging, and S. Miyazaki, *SMA microgripper with integrated antagonism*, Sensors and Actuators **83** (2000), 208–213. ix, 110, 111, 112

[KKH01]   S. H. Kim, S. H. Kim, and H. Huh, *Finite element inverse analysis for the design of intermediate dies in multi-stage deep-drawing processes with large aspect ratio*, Journal of Materials Processing Technology **113** (2001), 779–785. 121

[KLK⁺05]   S. Kota, K.-J. Lu, Z. Kreiner, B. Trease, J Arenas, and J. Geiger, *Design and application of compliant mechanisms for surgical tools*, ASME Journal of Biomedical Engineering **127** (2005), 981–989. 106

[LC01]   Ch. Lee and J. Cao, *Shell element formulation of multi-step inverse analysis for axisymmetric deep drawing process*, International Journal for Numerical Methods in Engineering **50** (2001), 681–706. 121

[LC07]   C-C. Lan and Y-J. Cheng, *Distributed shape optimization of compliant mechanisms using intrinsic functions*, Proceedings of ASME IDETC 2007 (2007). viii, 104, 105, 112

[LE03]   J. J. B. Lim and A. G. Erdman, *A review of mechanisms used in laparoscopic surgical instruments*, Mechanism and Machine Theory **38** (2003), 1133–1147. 110

[Lit07]   P. Litewka, *Smooth frictional contact between beams in 3d*, Computational Contact Mechanics (2007), 157–176. 118, 122

[LK03]   K. J. Lu and S. Kota, *Design of compliant mechanisms for morphing structural shapes*, Journal of Intelligent Systems and Structures **14** (2003), 379–391. 17, 39

[LK05]   K. J. Lu and S. Kota, *An effective method of synthesizing com-
           pliant adaptive structures using load path representation*, Journal
           of Intelligent Systems and Structures **16** (2005), 307–317. 17

[LK06]   K. J. Lu and S. Kota, *Topology and dimensional synthesis of com-
           pliant mechanisms using discrete optimization*, ASME Journal of
           Mechanical Design **128** (2006), 1080–1091. vi, 16

[Lob03]   N. Lobontiu, *Compliant mechanisms. design of flexure hinges*,
           CRC Press, Boca Raton, 2003. 3, 7

[LS04]   D. Laser and J. Santiago, *A review of micropumps*, Journal of
           Micromechanics and Microengineering **14** (2004), 35–64. 108

[Lub02]   V. A. Lubarda, *Elastoplasticity theory*, CRC Press LLC, 2002.
           121

[LZR07a]   J. Lu, X. Zhou, and M. L. Raghavan, *Computational method of
           inverse elastostatics for anisotropic hyperelastic solids*, Interna-
           tional Journal for Numerical Methods in Engineering **69** (2007),
           1239–1261. 19

[LZR07b]   J. Lu, X. Zhou, and M. L. Raghavan, *Computational method of
           inverse elastostatics for anisotropic hyperelastic solids*, Interna-
           tional Journal for Numerical Methods in Engineering **69** (2007),
           1239–1261. 121

[MMH96]   M. D. Murphy, A. Midha, and L. L. Howell, *The topological syn-
           thesis of compliant mechanisms*, Mechanism and Machine Theory
           31 (1996), 185–199. 12

[MNH94]   A. Midha, T. W. Norton, and L. L. Howell, *On the nomenclature,
           classification and abstractions of compliant mechanisms*, ASME
           Journal of Mechanical Design **116** (1994), 270–279. 4, 10

[NBEB04]   H. Naceur, S. Ben-Elechi, and J. L. Batoz, *The inverse approach
           for the design of sheet metal forming parameters to control spring-
           back effects*, Proceedings of ECCOMAS 2004, European Congress

on Comput. Meth. in Appl. Sci. and Engng., Jyvskyl (Finland), P. Neittaanmki, T. Rossi, S. Korotov, E. Oñate, J. Périaux D. Knrzer (eds.) **78** (2004), 133–148. 121

[NDBG04a] H. Naceur, A. Delaméziere, J. L. Batoz, and Y. Q. Guo, *Blank optimization in sheet metal forming using an evolutionary algorithm*, Journal of Materials Processing Technology **151** (2004), 183–192. 121

[NDBG04b] H. Naceur, A. Delaméziere, J. L. Batoz, and Y. Q. Guo, *Some improvements on the optimum process design in deep drawing using the inverse approach*, Journal of Materials Processing Technology **146** (2004), 250–262. 121

[Nor91] T. W. Norton, *On the nomenclature and classification, and mobility of compliant mechanisms*, Master's thesis, Purdue University, Indiana, USA, 1991. 4, 5

[NW05] N-T. Nguyen and Z. Wu, *Micromixers a review*, Journal of Micromechanics and Microengineering **15** (2005), 1–6. 108

[Ogd84] R. W. Ogden, *Non-linear elastic deformations*, Dover Publications, Inc., 1984. 64

[On92] E. Oñate, *Cálculo de estructuras por el método de elementos finitos*, CIMNE, 1992. 43

[OS00] M. A. Omar and A. A. Shabana, *A two-dimensional shear deformable beam for large rotations and deformation problems*, Journal of Sound and Vibration **243** (2000), 565–576. 42

[PC07] M. A. Pucheta and A. Cardona, *An automated method for type synthesis of planar linkages based on a constrained subgraph isomorphims detection*, Proceedings of MULTIBODY DYNAMICS 2009, ECCOMAS Thematic Conference. Warsaw, Poland. **18** (2007), 233–258. 13

[PC10]   M. A. Pucheta and A. Cardona, *Design of bistable compliant mechanisms using precisionposition and rigid-body replacement methods*, Mechanism and Machine Theory **45** (2010), 304–326. v, 12, 13

[PCGH96]   S. Patnaik, R. Coroneos, S. Guptill, and D. Hopkins, *Performance trend of different algorithms for structural design optimization*, NASA Technical Memorandum **4698** (1996). 31

[PL04]   M. A. Puso and T. A. Laursen, *A mortar segment-to-segment contact method for large deformation solid mechanics*, Computer Methods in Applied Mechanics and Engineering **193** (2004), 601–629. 118, 122

[PMBV10]   G. Palli, C. Melchiorri, G. Berselli, and G. Vassura, *Design and modelling of variable stiffness joints based on compliant flexures*, Proceedings of ASME IDETC 2007 (2010). v, viii, 11, 101, 102, 112

[Puc08]   M. A. Pucheta, *Computational methods for design and synthesis of planar mechanisms*, Ph.D. thesis, Universidad Nacional del Litoral, Santa Fe, Argentina, 2008. 12

[Roz97]   G. I. N. Rozvani, *Aims, scope, basic concepts and methods of topology optimization*, Topology Optimization in Structural Mechanics. CISM Courses and Lectures and Lectures N 374. International Centre for Mechanical Sciences, 1997. 14

[RR01]   B. Reyes Rodriguez, *Study of the degrees of freedom equations in the compliant mechanism design*, Proceedings EcoDesign 2001: Second International Symposium on Environmentally Conscious Design and Inverse Manufacturing (2001), 202–207. 5

[RR02]   A. Remouchamps and Y. Radovcic, *Boss quattro: an open system for parametric design*, Structural and Multidisciplinary Optimization **23** (2002), 140–152. 26

[RR05]   A. Remouchamps and Y. Radovic, *Boss/Quattro User Manual*, Samtech, S.A., Liége (Angleur), Belgium, 2005. vi, 24, 25, 31, 34

[RZS94]   G. I. N. Rozvani, M. Zhou, and O. Sigmund, *Topology optimization in structural design*, Advances in Design Optimization, Chapman and Hall, London., 1994. 14

[Sam07]   Samtech, S.A., Liége (Angleur), Belgium, *Samcef/Mecano V12.1 User Manual*, 2007. 62

[Sam10]   Samtech, S.A., Liége (Angleur), Belgium, *Samcef V13.1 User Manual*, 2010. 26

[SBB01]   V. Seidemann, S. Butefisch, and S. Buttgenbach, *Fabrication and investigation of in-plane compliant SU8 structures for MEMS and their application to micro-valves and micro-grippers*, Sensors and Actuators **98** (2001), 457–461. ix, 108, 109

[Sch05]   K. Schittkowski, *Optimization in industrial engineering: SQP - methods and applications*, Radioss User Meeting, Mecalog, Nice (2005). 31

[Sha08]   L. F. Shampine, *Vectorized adaptive quadrature in Matlab*, Journal of Computational and Applied Mathematics **211** (2008), 131–140. 96

[Sig01]   O. Sigmund, *A 99 line topology optimization code written in Matlab*, Structural and Multidisciplinary Optimization **21** (2001), 120–127. 26, 27

[SK01]   L. Saggere and S. Kota, *Synthesis of planar, compliant four-bar mechanisms for compliant-segment motion generation*, ASME Journal of Mechanical Design **123** (2001), 535–541. vii, 38, 52, 53, 54, 55, 57, 59

[Sva87]   K. Svanberg, *Method of moving asymptotes — a new method for estructural optimization*, International Journal for Numerical Methods in Engineering **24** (1987), 359–373. 30, 31

[Sva07]   K. Svanberg, *MMA and GCMMA, versions september 2007*, Available via http://www.math.kth.se/∼krille/gcmma07.pdf (2007), 1–9. 30

[SVQ86]   J. C. Simo and L. Vu-Quoc, *A three-dimensional finite strain-rod model. part II: Computational aspects*, Computer Methods in Applied Mechanics and Engineering **58** (1986), 79–116. 84, 99

[SZ05]   K. Schittkowski and C. Zillober, *SQP versus SCP methods for nonlinear programming*, Springer, 2005. 31

[Tar05]   A. Tarantola, *Inverse problem theory and model parameter estimation*, Siam, 2005. 18

[The10]   The MathWorks, Inc., *Matlab Optimization Toolbox 5. User Manual*, MathWorks ®, Natick, MA, USA, 2010. 51

[Tho03]   P. Thoutireddy, *Variational arbitrary lagrangian-eulerian method.*, Ph.D. thesis, California Institute of Technology, California, USA, 2003. 73

[TN65]   C. Truesdel and W. Noll, *The non-linear field theories of mechanics. in Enclyclopedia of Physics*, vol. 3, Flügge S, Springer, Berlin, 1965. 73

[TO04]   P. Thoutireddy and M. Ortiz, *A variational r-adaptation and shape-optimization method for finite-deformation elasticity*, International Journal for Numerical Methods in Engineering **1** (2004). 73

[Tro02]   A. Troxler, *Inverse design of gas turbine components*, Inverse Problems in Engineering, Rio de Janeiro, Brazil (2002). 19

[Van84]   G. Vanderplaats, *Numerical optimization techniques for engineering design*, McGraw-Hill, New York, 1984. 14, 24, 30, 31, 32

[Wan09]   Y. M. Wang, *Mechanical and geometric advantages in compliant mechanism optimization*, Frontiers of Mechanical Engineering in China **4** (2009), 229–241. 16

[WBWF07]   D. Wagg, I. Bond, P. Weaver, and M. Friswell, *Adaptive structures. engineering applications*, Faculty of Engineering, University of Bristol, UK, 2007. 1, 2, 3, 4

[WCWM05]   Y. M. Wang, S. Chen, X. Wang, and Y. Mei, *Design of multi-material compliant mechanisms using level set methods*, ASME Journal of Mechanical Design **5** (2005), 941–956. vi, 16, 17

[Wei04]   R. G. Weight, *High-torque capacity compliant centrifugal clutches*, Master's thesis, Brigham Young University, Provo, Utah, USA, 2004. 103

[WHH+06]   R. Wierzbicki, K. Houston, H. Heerling, W. Barth, T. Debski, A. Eisinberg, A. Menciassi, M.C. Caroozza, and P. Dario, *Design and fabrication of an electrostatically driven microgripper for blood vessel manipulation*, Journal of Micromechanics and Microengineering **83** (2006), 1651–1654. 110

[WL07]   Y. M. Wang and Z. Luo, *Shape and topology optimization of compliant mechanisms using level set-based parameterization method*, Proceedings of 12th World Congress in Mechanism and Machine Science, Besancon, France (2007). 16

[Woi05]   P. Woias, *Micropumps-past, progress and future prospects*, Sensors and Actuators **105** (2005), 28–38. 108

[WW06]   P. Wei and Y. M. Wang, *Parametric structural shape and topology optimization method with radial basis functions and level-set method*, Proceedings of ASME IDETC 2007 (2006). 16

[XS97]   Y. M. Xie and G. P. Steven, *Evolutionary Structural Optimization*, Berlin, Heidelberg, New York: Springer, 1997. 27

[Yam97]   T. Yamada, *Finite element procedure of initial shape determination for hyperelasticity*, Structural Engineering and Mechanics **436** (1997), 173–183. 19, 62, 63

[YHCD06]   Y. Y. Huang, Y. P. Chen, and R. X. Du, *A new approach to solve key issues in multi-step inverse finite-element method in sheet metal stamping*, International Journal of Mechanical Sciences **48** (2006), 591–600. 121

[ZFD96]   W. H. Zhang, C. Fleury, and P. Duysinx, *A generalized method of moving asymptotes (GMMA) including equality constraints*, Structural Optimization **12** (1996), 143–146. 30

[ZHS98]   C. Zhao, P. Hornby, and G. P. Steven, *A generalized evolutionary method for numerical topology optimization of structures under static loading conditions*, Structural Optimization **15** (1998), 251–260. 27

[ZL08]   X. Zhou and J. Lu, *Inverse formulation for geometrically exact stress resultant shells*, International Journal for Numerical Methods in Engineering **74** (2008), 1278–1302. 19, 121

[ZT00]   O. C. Zienkiewicz and R. L. Taylor, *The finite element method*, vol. 2, Butterworth-Heinemann, London, 2000. 68, 81, 91, 92, 112